Institute of Veterinary Pathology
Department of Veterinary Medicine
Freie Universität Berlin
and
Experimental Transplantation Surgery
Department of General, Visceral and Vascular Surgery
University Hospital Jena, Medical Faculty
Friedrich-Schiller University Jena

Impact of Steatosis on Drug Metabolism of the Liver: Functional and Translational Implications

Thesis submitted for the fulfillment of a
Doctor of Philosophy (PhD) degree in Biomedical Sciences
at the
Freie Universität Berlin

submitted by
Mohamed Awad Mohamed Albadry
Veterinarian from Dakahliya / Egypt

Berlin 2024

Journal-No.: 4474

Printed with permission of the Department of Veterinary Medicine
of Freie Universität Berlin

Dean	Univ.-Prof. Dr. Uwe Rösler
First Reviewer	Univ.-Porf. Dr. Robert Klopfleisch
Second Reviewer	Prof. Dr. Uta Dahmen
Third Reviewer	PD.Dr. Lars Mundhenk

Descriptors (according to CAB-Thesaurus):
Mice, liver, fibrosis, drug metabolism, steatosis, animal models, cytochromes

Promotion Date: 07.08.2024

Dedicated to

My family

Table of Contents

List of tables

List of figures

List of abbreviations

$t_{1/2}$	Half-life
t_{peak}	Time of peak concentration
x_{peak}	Peak concentration
2D	Two-dimensional
3D	Three-dimensional
AI	Artificial intelligence
AUC	Area under the curve
Bf3R	The German Centre for the Protection of Laboratory Animals
CCL4	Carbon tetrachloride
C-max	maximum concentration
CV	Central vein
CYP	Cytochrome P450
DAB	3,3′-Diaminobenzidine
ECOD	Ethoxycoumarin-O-Deethylation
EMND	Ethylmorphine-N-Demethylation
EROD	Ethoxyresorufin-O-Deethylation
ESS	Effective Sample Size
FFA	Free fatty acid
FLD	Fatty liver disease
GS	Glutamate synthetase
HDAB	Hematoxylin 3,3′-Diaminobenzidine

HE	Hematoxylin and Eosin
HF-diet	high-fat diet
i.p	Intraperitoneal
ICL	Inferior caudate lobe
IHC	Immunohistochemitry
LLL	Left lateral lobe
MCD	Methionine choline-deficient
MCMC	Markov Chain Monte Carlo
ME	Margin of error
N	Number of replicates
NAFLD	Non-alcoholic fatty liver disease
NASH	Non-alcoholic steatohepatitis
ODE	Ordinary differential equation
PK	Pharmacokinetics data
PNPH	P-Nitrophenol-Hydroxylation
PROD	Pentoxyresorufin-O-Depentylation
PV	Portal vein
r	Correlation coefficient
RML	Right median lobe
ROI	Region of interest
RSL	Right superior lobe
SBML	Systems Biology Markup Language

s.c.	subcutaneous
Sd	Standard deviation
TG	Triglyceride
TPS	Tissue positioning system
UPLC-MS/MS	Ultra-performance liquid chromatography-tandem mass spectrometry
WSI	Whole slide Image
ZDF	Zucker diabetic fatty
μ	Mean of the parameter

1. Introduction (research questions and hypotheses)

The influence of steatosis on drug metabolism has been discussed controversially. Information about the impact of the zonal distribution of steatosis on centrally located hepatic functions, such as drug metabolism, is not available. Additionally, the translational relevance of the complex underlying biological processes should be considered when addressing fundamental science questions. Therefore, we designed two subsequent studies addressing these two aspects in the context of steatosis and drug metabolism.

On the biological side, we were interested in the impact of zonated steatosis on drug metabolism features using a mouse model. On the translational side, we investigated the differences in lobular geometry and spatial distribution of CYP expression to get a notion regarding the potential translation of the results to the human situation.

The following section outlines the scientific questions and underlying hypotheses in detail.

1.1. Research questions

1.1.1. How does zonated periportal steatosis impact centrally located drug-metabolizing enzymes?

Diseases such as fatty liver disease may impact the zonated expression of CYP enzymes and possibly the zonation of function. So far, little attention has been paid to previous studies to describe the severity, type, and zonation pattern of fat accumulation. These factors may affect CYP expression pattern and/or activity and, consequently, the drug-metabolizing function of the corresponding CYP enzyme.

Therefore, we studied the impact of periportal steatosis on pericentrally located drug metabolism functions, focusing on the major CYP isoforms CYP1A2, CYP2D6, CYP2E1, and CYP3A4 (Albadry et al. 2022).

1.1.2. How similar are lobular geometry and zonal expression of key CYP as two key features governing drug metabolism in frequently used animal models?

Animal models are frequently used in preclinical research, but their translational relevance is discussed controversially. The current literature provides little insight regarding the cross-species similarities or differences in microscopical lobular structure, expression pattern, or function of CYP enzymes. However, these differences are potentially affecting the translatability of drug metabolism studies.

Therefore, we want to investigate the lobular geometry and the expression pattern of key CYP enzymes in different species. In addition, we want to identify the minimum number of liver lobules

in the four species (mice, rats, pigs, and humans) needed for reliable quantification of zonated expression of a given CYP enzyme (Albadry et al. 2024).

1.2. Scientific hypothesis

We raised two hypotheses:

1.2.1. Periportal steatosis may affect zonated drug metabolism parameters.

1.2.2. Lobular geometry as an anatomical feature is species-independent (low interspecies variability), whereas CYP expression as a functional parameter is species-dependent (high interspecies variability).

2. Literature

2.1. Liver

2.1.1. Morphology

The liver is crucial in coordinating major physiological processes in the human body. It is known for its complex anatomical structure and functional heterogeneity (Trefts et al. 2017). Anatomically, the human liver comprises four major lobes: the right, left, caudate, and quadrate lobes. Each of these lobes consists of thousands of lobules (Vernon et al. 2023). Liver lobules are arranged as irregular polygons, made up of hepatic cords that extend outwards from the central vein in the center of the lobule to the portal triad in the periphery. The hepatic acinus is the key functional structure in the liver. Hepatocytes are arranged in alignment with the afferent vascular systems (portal veins and hepatic arteries) as they merge into the hepatic capillaries, the so-called sinusoids (Figure 1) (Washabau 2013).

The liver structure comprises two main seamlessly integrated components: the parenchymal cells called hepatocytes as well as the biliary and vascular tree supplying and draining the organ (Guido et al. 2019). In addition, the liver has various non-parenchymal cells: Cholangiocytes, stellate cells, Kupffer cells, oval cells, and hepatic sinusoidal endothelial cells. Each cell type has a distinct role in contributing to overall metabolic homeostasis in the body. Hepatocytes are the primary functional unit of the liver and are responsible for metabolic functions such as protein and carbohydrate metabolism, as well as detoxification (Trefts et al. 2017).

2.1.2. Metabolic Zonation

Liver function is spatially organized along the hepatic sinusoids extending from the portal area to the central vein (porto-central axis), a phenomenon called “metabolic zonation” (Gebhardt 1992). He reported for the first time that there are intralobular gradients of oxygen, nutrients and metabolites.

According to these gradients along the porto-central axis of the liver, liver lobules are separated into three functional zones that are specialized in carrying out specific metabolic functions in metabolism, detoxification, and bile generation (Kietzmann 2017;Manco and Itzkovitz 2021) (Figure 1). Zone 1, also known as the periportal zone, is in the closest vicinity to the arterioles and bile duct and has high oxygen levels and nutrients. Zone 1 is the central location for oxygen-requiring processes such as gluconeogenesis, cholesterol biosynthesis, ureagenesis, and fatty acid β-oxidation. Zone 2, or the midzone, performs a mixture of functions, including special ones like maintaining iron homeostasis and regulation of insulin-like growth factors. Zone 3, also called the pericentral zone (around the central vein), has a lower oxygen level and is primarily

responsible for glycolysis, bile-acid biosynthesis, glutamine synthesis, lipogenesis, and xenobiotic metabolism. The term xenobiotic metabolism refers mainly to metabolizing (potentially toxic) drugs by rendering less polar compounds into more polar compounds that can be excreted (Kietzmann 2017;Ben-Moshe et al. 2019;Manco and Itzkovitz 2021;Yap and Mitchell 2022).

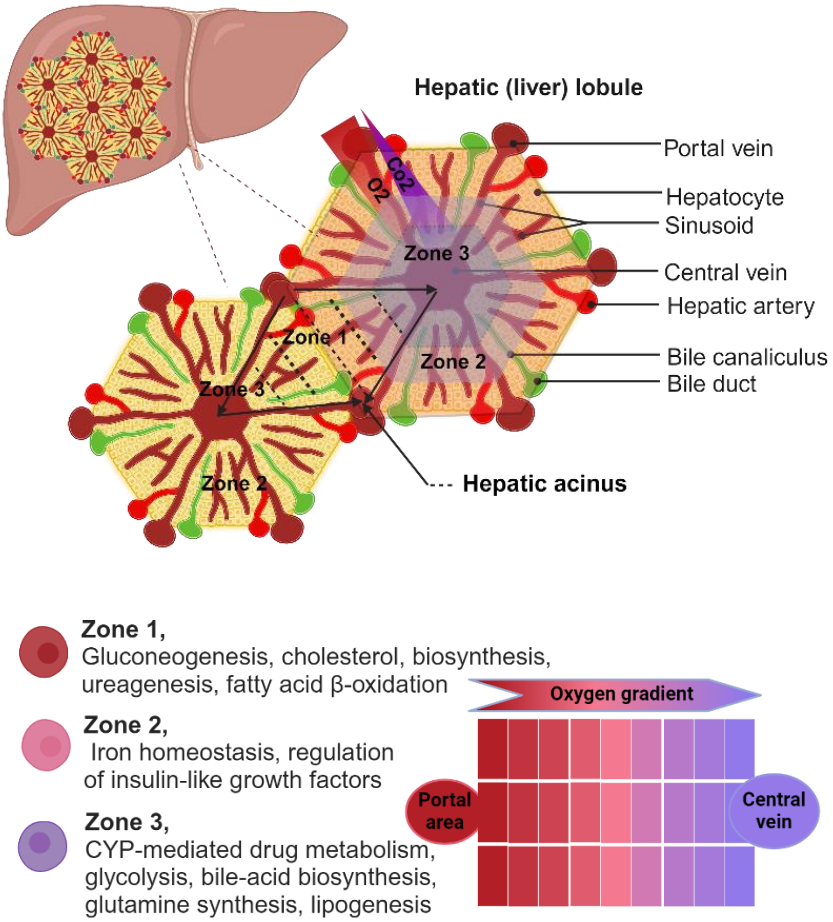

Figure 1. Overview of hepatic lobule structure and zonal distribution of functions. Hepatocytes are arranged in alignment with the afferent vascular systems (portal veins and hepatic arteries) as they merge into sinusoids. The liver acinus is divided into three adjacent zones (zone 1, 2, and 3). Hepatocytes located in zone 1, which is in the closest vicinity to the arterioles, receive the highest oxygen content. Zone 1 is the main location for oxidative processes such as gluconeogenesis, cholesterol biosynthesis, ureagenesis, and fatty acid β-oxidation. Hepatocytes are located in zone 2, which is the midzone between zone 1 and zone 3. Zone 2 is the main location for a mixture of functions, including iron homeostasis and regulation of insulin-like growth factors. Hepatocytes in zone 3 are located at the outside border of the acinus, close to the central vein, and have a lower oxygen level. Zone 3 is the main location for glycolysis, bile-acid biosynthesis, glutamine synthesis, lipogenesis, and CYP-mediated drug metabolism, clearance, and detoxification. “Created with BioRender.com.”

2.1.3. Drug metabolism

Drug metabolism refers to the enzymatic modification of drug molecules within the body (Almazroo et al. 2017). Drug metabolism occurs in three phases: modification, conjugation, and elimination. Phase I involves the oxidation, reduction, and hydrolysis of drugs with the help of the hepatic microsomal enzyme Cytochrome P450 (CYP) enzyme system. Following Phase I, Phase II requires conjugation of the metabolized drug to a low-molecular-weight polar compound, which renders the drug water-soluble. Phase III involves the elimination of low molecular weight molecules with the help of drug transporters (Almazroo et al. 2017;Garza et al. 2022).

CYP enzymes are the most widely recognized key drug-metabolizing enzymes involved in phase I (Almazroo et al. 2017;Garza et al. 2022). CYPs involve a group of isoenzymes in the mitochondria and smooth endoplasmic reticulum of hepatocytes, proximal renal tubules, and small intestinal epithelium (Almazroo et al. 2017). Among CYPs, the CYP3A subfamily (3A4, 3A5) constitutes approximately 40% of total hepatic CYP content, followed by CYPs 2C (25%), 1A2 (18%), 2E1 (9%), 2A6 (6%), 2D6 (2%), and 2B6 (<1%) (Figure 2) (Shimada et al. 1994;Paine et al. 2006). CYP1A2, 2C8, 2C9, 2E1, and 3A4 are the most abundant hepatic CYPs, whereas CYP2A6, 2B6, 2C19, 2D6, and 3A5 are less expressed (Paine et al. 2006;Zanger and Schwab 2013;Almazroo et al. 2017).

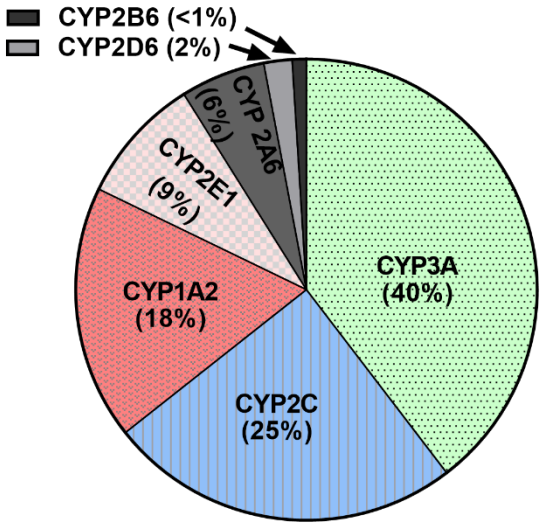

Figure 2. Average relative hepatic CYP protein content. Liver pie values were obtained from (Shimada et al. 1994;Paine et al. 2006). "Created with GraphPad Prism version 9.3.1(471) for Windows, a software developed by GraphPad Software, San Diego, California, USA, www.graphpad.com".

2.1.4. Portalization

Hepatic CYP enzymes have a distinct zonation pattern, characterized by their strong expression and selective induction in the pericentral zone (Lindros 1997;Kietzmann 2017;Ben-Moshe et al. 2019). Little is described about the extent of pericentral expression of the different CYP enzymes. Our current understanding of how morphological alterations in the different lobular zones affect CYP-dependent drug expression and function is limited. Damage to the pericentral zone is known to directly impact the pericentral expression of certain CYP enzymes (Schenk et al. 2017;Ghallab et al. 2019). In contrast, the impact of periportal damage or alterations on pericentral processes remains unclear.

Recent research by Ghallab and their colleagues (2019) suggests that alterations in the periportal zone may also affect metabolic processes in the pericentral zone. Their findings indicate that pericentral and periportal fibrosis can have a comparable impact on the zonated expression of hepatic CYP proteins. Both conditions resulted in a partial or complete loss of pericentral CYP expression. They also observed a phenomenon called "portalization of pericentral hepatocytes," where pericentral hepatocytes acquire features similar to periportal hepatocytes (Ghallab et al. 2019). However, they did not investigate the impact of portalization on the functional activity of different CYP proteins.

This gap of knowledge emphasizes the importance of conducting further studies to gain a complete understanding of the phenomenon of portalization.

2.2. Steatosis

Hepatic Steatosis is the accumulation of fat in more than 5% of the hepatocytes, either in a micro- or macrovesicular pattern (European Association for the Study of the Liver et al. 2016).

2.2.1. Epidemiology

Hepatic steatosis is a global health burden characterized by excessive fat accumulation in the liver, potentially causing hepatic dysfunction (Pereira et al. 2017). Steatosis affects individuals of all ages and ethnicities, and its prevalence is increasing. Steatosis, often also called fatty liver disease, does not have one common cause but has different etiologies. Dietary nonalcoholic and alcoholic fatty liver disease are the most common types, followed by chemotherapy- or drug-induced fatty liver disease. Other causes of steatosis include inflammatory diseases such as viral hepatitis and autoimmune hepatitis (Burt et al. 2015).

The overall global prevalence of steatosis is approximately 30%, with the highest rates observed in Latin America (44.37%), followed by the Middle East and North Africa (36.53%), South Asia

(33.89%), North America (31.20%), East Asia (29.71%), Asia Pacific (28.02%), and Western Europe (29.71%) (Figure 3) (Younossi et al. 2023).

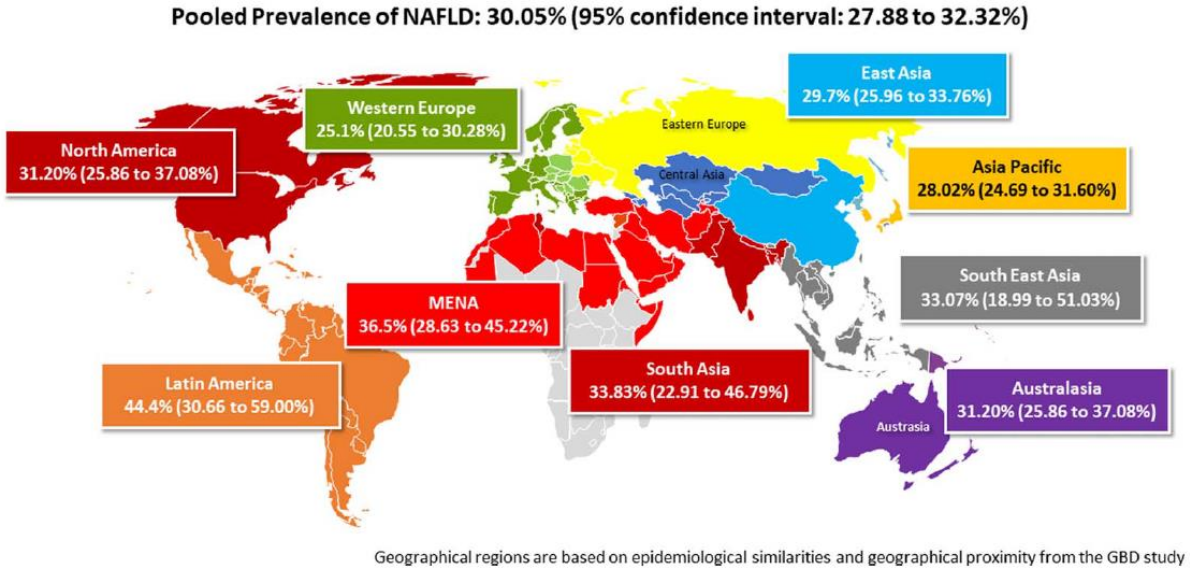

Figure 3. Global and regional data collected from 1990 to 2019 reveals the prevalence of NAFLD. “Obtained from (Younossi et al. 2023), “used with friendly permission of journal of Hepatology, Wolters Kluwer Health, Inc (license number: 5710940825018)”.

The anticipated prevalence of nonalcoholic fatty liver disease (NAFLD) in the United States is expected to rise by more than 20%, from 83 million cases in 2015 to 100 million cases in 2030. Similarly, the prevalence of nonalcoholic steatohepatitis (NASH) is expected to rise from 16 million cases to 27 million cases. It is estimated that by 2030, around one-third of adults aged 15 years and older will suffer from NAFLD. Furthermore, the median age of people with NAFLD is expected to increase from 50 to 55 years between 2015 and 2030 (Estes et al. 2018). These findings suggest that NAFLD is a growing global health concern, with the prevalence of steatosis increasing steadily over the years.

2.2.2. Pathogenesis

The liver is the central organ for lipid metabolism. The pathogenesis of fatty changes in the liver centers around the biochemical process of free fatty acid (FFA) metabolism. FFA, originating from triglycerides, constitutes a substantial portion of the fundamental energy requirements of parenchymal cells. FFA are mostly derived from dietary intake and digestion, chylomicrons in the bloodstream, or adipose cells in body fat reserves (adipose tissue). Chylomicrons carry dietary lipids, primarily triglycerides, from the digestive system to the liver, muscles, and adipose tissue. The lipase enzyme within chylomicrons interacts to release fatty acids from triglycerides, which

are used as a basis for energy production. In the liver, free fatty acids either undergo esterification to form triglycerides, or are transformed into cholesterol or phospholipids, or are oxidized to ketones. Triglycerides can be released by hepatocytes only when apolipoproteins transform them into lipoproteins for transportation. Alterations in these metabolic pathways can lead to the accumulation of triglycerides and other lipid metabolites within the hepatocyte, causing hepatic steatosis (Vetelainen et al. 2007;Zachary and Mcgavin 2012) (Figure 4).

.

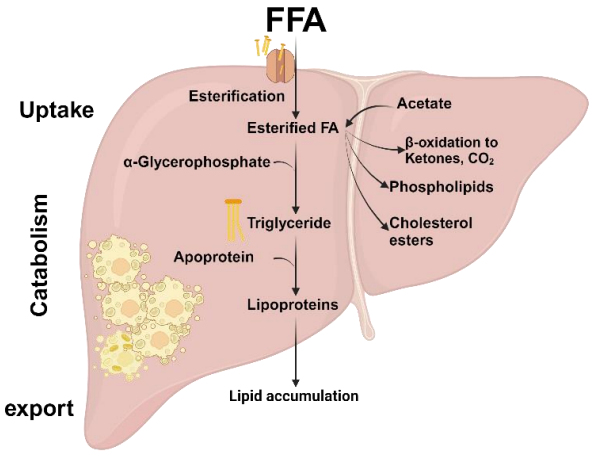

Figure 4. Overview of free fatty acid (FFA) catabolism by the liver. Alteration in one of these metabolic pathways leads to the accumulation of fat in the hepatocytes and results in hepatic steatosis. Information extracted from (Vetelainen et al. 2007;Zachary and Mcgavin 2012). “Created with BioRender.com.”

Steatosis most commonly develops due to caloric overload or dietary imbalance, such as a lack of essential nutrients like choline and methionine deficiency (Santhekadur et al. 2018). Steatosis can also result from exposure to toxic substances like alcohol or certain drugs such as methotrexate (Kolaric et al. 2021). Alcohol is the most frequent toxin that can lead to hepatic steatosis in patients. Experimentally used toxic substances such as Carbon tetrachloride (CCL4) can cause hepatic steatosis by decreasing the oxidation of free fatty acids. Hepatic steatosis can also be caused by conditions that result in increased mobilization of the fat stores due to a higher demand for energy over a short period. Additionally, steatosis may occur in cases of malnutrition, where apolipoprotein synthesis is impaired, and in case of starvation, where triglycerides are mobilized (Vetelainen et al. 2007;Zachary and Mcgavin 2012).

In general, the etiology of steatosis in humans is not entirely clear and can result from various processes, as mentioned above, which may even occur simultaneously. Patients can suffer from caloric overload due to an unbalanced diet together with excessive alcohol consumption and/or

therapy with hepatotoxic drugs (Osna et al. 2017). Therefore, in clinical studies, etiology is often multifactorial and cannot be attributed to one clear cause (Stefan et al. 2008;Lonardo et al. 2015). As a result, the histological pattern (macro- versus microvesicular steatosis) and the lobular zonal distribution (periportal versus pericentral) (Figure 5) can be less clear and often appear mixed.
In contrast, the etiology is known in animal studies, but studies are also hardly comparable due to abundant variations of steatosis induction protocols (Stärkel et al. 2003;Kulkarni et al. 2016;Soret et al. 2020). Several well-established animal models mimic different etiologies of steatosis. For instance, the Zucker diabetic fatty (ZDF) rat is a genetic model of obesity-related steatosis (Kanuri and Bergheim 2013). Griffen showed in 2001 that the ZDF rat carries a genetic defect in beta-cell transcription inherited independently from the leptin receptor mutation and insulin resistance (Griffen et al. 2001). In contrast, the ob/ob mouse is also a genetic model but lacks the leptin hormone (Kanuri and Bergheim 2013).

2.2.3. Zonation and drug metabolism

Hepatic steatosis may affect liver function. Regardless of the cause, hepatic steatosis can influence liver function by interfering with regular metabolic processes. Advanced NAFLD is associated with systemic metabolic disorders, including disturbances in glucose metabolism, such as insulin resistance (Farrell et al. 2008;Lu et al. 2021). At the cellular level, surplus fat accumulation also affects the functional activity of hepatocytes. Fat accumulation can impair various metabolic processes such as glycolysis, gluconeogenesis, lactate generation, tricarboxylic acid cycle, and mitochondrial oxidation, ultimately leading to disease progression (Lu et al. 2021).
There are controversial reports regarding the impact of steatosis on drug metabolism (Weltman et al. 1996;Stärkel et al. 2003;Bell et al. 2010;Hata et al. 2010;Merrell and Cherrington 2011;Kostrzewski et al. 2017), for details see Appendix, Tables S 2 - S 4. One reason for the controversial results could be that the etiology, zonation pattern, type, and severity of steatosis were not reported and considered.
Therefore, the impact of the zonal (periportal or pericentral) distribution of fat (Figure 5**)** on the function and expression of centrally located drug-metabolizing enzymes needs to be investigated.

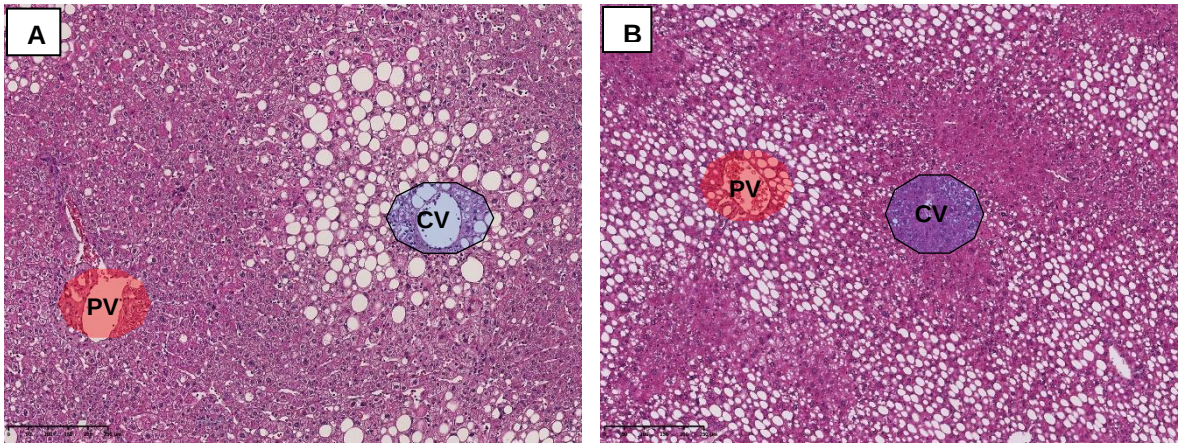

Figure 5. Overview of HE-stained liver section with two different zonated steatosis patterns. (A) HE staining of human liver tissue with pericentral steatosis. Fat is mainly located in hepatocytes in zone 3 around the central vein (CV). (B) HE staining of mouse liver tissue with periportal steatosis. Fat is mainly located in hepatocytes in zone 1 around the portal vein (PV). Unpublished images; scale bar: 250 µm.

Doing so allows us to address whether and which type and distribution of steatosis could also lead to portalization, as described by Ghallab for fibrosis. Spatially resolved expression data are of utmost importance in addressing this question.

2.3. Translational medicine

The relevance of animal studies to human situations is discussed controversially. It is not always possible to immediately apply the results of basic science studies of biological phenomena in the clinical setting. There is a clear need for basic science investigations to be more focused on their clinical relevance rather than simply exploring biological phenomena for their own sake.

Translational medicine aims to apply the knowledge obtained from animal studies to human applications (Wehling 2011). Adopting a systems medicine approach can accelerate the process by integrating observations acquired from laboratory experiments and clinical trials using simplified computational models (Murad 2022).

Scientific research involving animal studies aims to enhance our comprehension of health and illness. At the same time, animal experiments may yield crucial insights for the development of future strategies for prevention and treatment (Nih 2022). Therefore, many animal models are used in pre-clinical scientific studies. According to Bf3R (The German Centre for the Protection of Laboratory Animals), the number of animals used in research and the number of animals euthanized for scientific purposes in 2022 in Germany amount to approximately 2.4 million laboratory animals. Liver-related basic research accounts for around 4% of animal studies (Bf3r 2022).

Lab animals are used for drug metabolism experiments, especially for pharmacokinetic and pharmacodynamic, as well as for toxicological studies. However, the relevance is discussed controversially. Bailey and Balls stated that there is currently no significant and publicly available evidence to support the scientific validity of these tests in accurately predicting human responses (Bailey and Balls 2019). Bailey and co-workers analyzed the most extensive quantitative database of publicly accessible experimental toxicology studies. He did find that experiments conducted on animals, specifically rats, mice, and rabbits, are remarkably inconsistent in their ability to predict toxic reactions in humans (Bailey et al. 2014).

In contrast, Claude Bernard, widely recognized as the father of physiology, declared, "Animal experiments provide clear evidence for the study of the effects of toxins and the maintenance of human health." He claimed that the effects of these chemicals were identical in humans and animals, the only difference being the degree of effect (Hajar 2011).

Therefore, translation of drug metabolism studies is difficult due to unknown species differences in terms of anatomy and functional activity of the liver. As a result, there is a need to explore the relevance of observations obtained in animal experiments for the clinical situation in a given scientific question.

2.3.1. Cross-species differences in liver anatomy and lobular geometry

In drug metabolism studies, different species are used. Larger animals, such as pigs or non-human primates, are often preferred as animal models when addressing surgical questions. This is because larger animals have anatomical and physiological similarities to humans, making them suitable for surgical procedures. For example, the size and structure of pig organs, blood vessels, and tissues closely resemble those of humans, allowing researchers to simulate surgical procedures and assess their efficacy and safety (Cozzi et al. 2009). On the other hand, smaller animals, such as mice and rats, are often preferred as animal models when investigating molecular processes. Their smaller size and shorter lifespan make them more cost-effective and easier to handle in laboratory settings. Additionally, mice and rats share a significant amount of genetic similarity with humans, making them valuable models for investigating the molecular pathways that underlie diseases and the interactions of drugs (Bryda 2013;Vinod and Mahalakshmi 2023).

The following striking variations are apparent when comparing liver gross anatomy, histology, and physiology in different species. Rat, mouse, and pig livers are composed of different lobes, whereas the human liver lacks distinct lobes. Humans, pigs, and mice possess gallbladders; however, rats do not have this organ (Kruepunga et al. 2019). Pigs possess interlobular septa

separating the liver lobes, whereas humans, rats, and mice do not exhibit this anatomical feature (Teutsch et al. 1999).

Lobular geometry is generally assumed to be of perfect regular structure and geometrical symmetries, as stated by (Rohan et al. 2021). However, little is known about the actual geometry. Therefore, the lobule is generally described as either a hexagon or polygon in shape, respectively polyhedron shape, when referring to 3D.

Even less is known about potential differences in lobular geometry in different species. However, this information is needed to better understand the potential impact of the hepatic microstructures on functional parameters. Anatomical and functional variations in the liver of different species may interfere with the accurate interpretation of findings.

2.3.2. Cross-species differences in zonation of CYP

The extent of species differences in the zonation of drug metabolism in relation to lobular geometry remains unknown. Few studies have investigated the expression, zonation, and distribution of CYP enzymes across species. The spatial resolution of expression was rarely taken into account. Prior work, such as that of Hammer and colleagues, has used targeted proteomics to obtain cross-species information regarding the abundance of CYP proteins. These investigations mainly focused on comparing various experimental settings, both *in vivo* and *in vitro*, in mice, rats, humans, and undifferentiated HepaRG cells (Hammer et al. 2021). Based on their observation, they found comparable and abundant expression levels of the CYP2D and CYP2E1 proteins across mice, rats, and humans. At the same time, CYP3A expression were similar but relatively moderate in clinical liver biopsies, rats, and mice. Moreover, they demonstrated moderate expression of CYP3A in humans, rats, and mice. Hrycay and Bandiera also comprehensively reviewed the similarities and differences in expression levels between mouse-human CYP proteins (Hrycay and Bandiera 2009). By analyzing a database of CYP gene expression, they concluded that the laboratory mice serve as an essential tool for understanding CYP-mediated activities. The findings suggest that using laboratory mice can provide valuable insights into the mechanisms of CYP-mediated reactions that support drug development and medical research. However, in both studies, the spatial distribution of CYP expression was not investigated.

A spatially resolved cross-species comparison of CYP expression based on histological data is not yet available. The expression pattern and the extent of expression variability need to be investigated in different species. This is important since the variability directly influences the number of liver lobules to be examined.

Such knowledge is crucial for comprehending drug metabolism and toxicity variations among different species. It is also useful for selecting a suitable animal model for evaluating drugs in

preclinical stages. This knowledge is equally important for clinical investigations, as liver tissue is frequently acquired through minimally invasive needle biopsies. Due to the limited size of these samples, there is also a need to determine the minimum number of lobules for reliable zonated quantification of CYP expression in a given species.

2.3.3. Implementation of Image analysis approaches for quantification of lobular geometry and zonation

Several approaches have been used to describe liver lobular geometries and their zonation patterns. Lau and co-workers employed Voronoi theory to examine the lobular geometry of the liver in both normal porcine and human livers to obtain a deeper understanding of the structural organization of classical liver lobules (Lau et al. 2021). In another study, zonal image analysis via Voronoi tessellation was used to determine the distribution of hypoxia markers in the hepatic lobule of steatotic livers in mice (Peleman et al. 2023). Both cases involved the manual annotation of central veins in stained porcine and human or mouse and human liver sections. This approach included the use of hematoxylin-eosin and immunohistochemical staining for glutamine synthetase (GS), which serves as a functional marker for hepatocytes located pericentrally. In a recent study by Rong and co-workers, a tissue positioning system was proposed as a deep learning-based analysis pipeline. This system aims to achieve spatial analysis and quantification of zonation within the liver lobule by utilizing differentially expressed markers in a mouse model (Rong et al. 2023). Nevertheless, the primary emphasis of this study was on zonation analysis, with no consideration given to lobular geometry.

Understanding liver lobular geometry in different species is still elusive. Likewise, it is necessary to establish a more precise tool to determine zonation patterns of CYP enzymes across different species, as the degree of their similarities or differences is still largely undetermined. Moreover, the intrahepatic interlobular variability in the zonal expression of CYP enzymes has not been thoroughly investigated despite its relevance. Interlobular variability is a major concern in human studies, especially when obtaining liver tissue through minimally invasive needle biopsies. Considering the limited availability of such samples, it is crucial to ascertain the minimum number of lobules necessary for accurate qualitative and quantitative diagnosis. One limitation in the field is the lack of a readily applicable mathematical framework that can accurately identify geometries and zonation patterns from whole slide images (WSI). This mathematical framework is necessary for standardized, accurate, and reproducible analysis.

3. Materials and methods

3.1. Experimental design

First, we studied the impact of zonal periportal steatosis on pericentrally located drug-metabolizing enzymes. As described before by Albadry and co-workers, male C57BL6/J mice were fed a high-fat diet, low in methionine and choline content (HF-diet) for a duration of either two weeks or four weeks (n=6/group) (Albadry et al. 2022). Unlike the methionine-choline deficient diet (MCD), this dietary protocol leads to the development of periportal steatosis in rats and mice but does not result in any weight reduction (Sun 2011;Deng et al. 2014;Schwen et al. 2016;Homeyer et al. 2018). The control group received a regular maintenance diet (n=4-6/group).

Pharmacokinetics was evaluated by injecting an intraperitoneal (i.p) drug cocktail of caffeine, midazolam, and codeine, followed by taking micro-blood samples at ten scheduled intervals over six hours. The micro-blood samples were analyzed using ultra-performance liquid chromatography-tandem mass spectrometry (UPLC-MS/MS) to measure drug elimination rate and level.

The animals were euthanized 24 hours after i.p injection of the drug cocktail. After applying buprenorphine in a dose of 0.3mg/kg subcutaneous (s.c.), the animals were anesthetized using 3% Isoflurane and subjected to laparotomy. Death was induced by an overdose of isoflurane, followed by exsanguination. Liver tissue samples were then obtained from four distinct liver lobes: the left lateral lobe (LLL), the right median lobe (RML), the right superior lobe (RSL), and the inferior caudate lobe (ICL). Afterward, the samples were either formalin-fixed, followed by paraffin embedding, or snap-frozen and stored at -80°C until needed.

The severity of steatosis was evaluated by measuring triglyceride levels (TG). Hepatic steatosis was also assessed histologically, considering the pattern (micro vs. macrovesicular), zonal lobular distribution (periportal vs. pericentral), and severity using automated computer-based quantitative analysis with Whole-Slide Image (WSI) scans.

Immunohistochemical staining was used to visualize the spatial distribution of four drug-metabolizing enzymes, namely, CYP1A2, CYP2D6, CYP2E1, and CYP3A4, and glutamine synthetase as a marker for pericentral hepatocytes. The activity of these enzymes was evaluated through five model reactions using either a photometric or a fluorometric assay, as depicted in (Figure 6A).

Second, we investigated the differences in liver lobular geometry and CYP distribution in mice, rats, pigs, and humans based on the WSI of the HE-stained liver section. We also determined the minimum number of liver lobules required for conducting a drug metabolism study across these

species. As described before by Albadry and co-workers, normal liver samples from four species (mice, rats, pigs, and humans) were selected and retrieved from the sample archive of the Experimental Transplantation Surgery Lab, Department of General, Visceral, and Vascular Surgery, University Hospital of Jena (Albadry et al. 2024).

Immunohistochemistry of the same four different CYPs was performed to visualize and semi-quantify the zonal expression pattern of CYP enzymes across the four species. An image analysis pipeline was established using WSI scans to quantify lobular geometries and zonation patterns. The minimum number of required lobules was calculated based on the method of determining sample size for estimating a population means, with a confidence level of 95% and a margin of 20% error (Figure 6B).

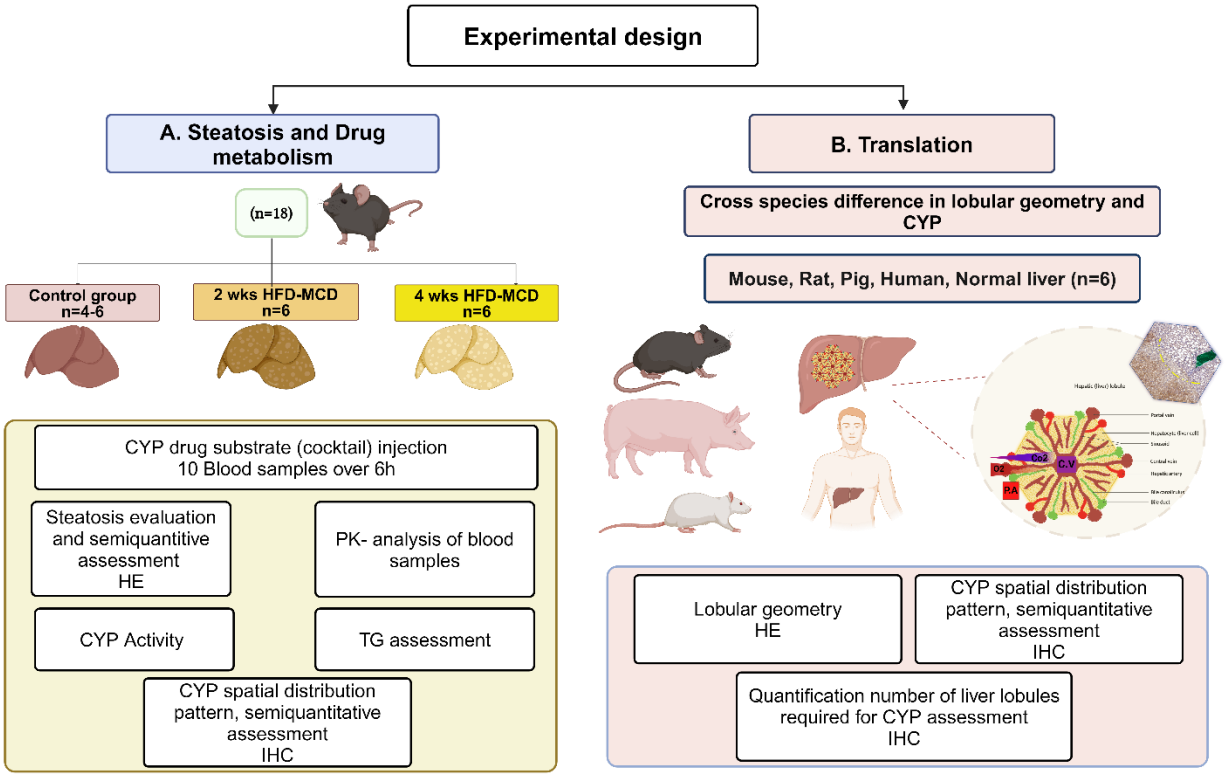

Figure 6. Overview of the experimental design for the two experiments. (A) Experiment A was designed to investigate the effects of periportal steatosis on the CYP enzymes in the pericentral region. (B) Experiment B was designed to determine the translational relevance of drug metabolism studies across different species in terms of lobular geometry and zonal distribution of CYP expression. The minimum number of liver lobules required for a reliable drug metabolism study in four species was also quantified. “Created with BioRender.com.”

3.2. Animals

3.2.1. Establishment of periportal steatosis model

First, to establish the model for periportal steatosis, a series of in-vivo studies were conducted using male C57BL6/J mice (Janvier, France) with a body weight of 28-30g and aged between 8-10 months (ex-breeder), with 4-6 mice per group. The mice were randomly housed in three groups and provided unrestricted access to food and water. The cages were maintained in a conventional animal facility under constant environmental conditions, including a twelve-hour light/dark cycle, a room temperature of 21±2°C, and relative humidity levels between 45-65%.

In this study (Albadry et al. 2022), mice were subjected to a high-fat (HF) low in methionine and choline diet for two or four weeks. The HF diet low in methionine and choline (E15652-94 EF R/M, high-fat MCD mod, Ssniff Spezialdiäten GmbH, Sulzfeld, Germany) was used to induce varying degrees of steatosis, as detailed in the appendix (Table S 1). The control group was fed a standard maintenance diet from Altromin Spezialfutter GmbH in Germany. Throughout the study, food intake and body weight gain were monitored daily.

3.2.2. Animal selection for quantifying cross-species variations in lobular geometry and CYP zonation

Archived formalin-fixed and paraffin-embedded from normal mice, rats, pigs, and human liver samples (n = 6/species) were used for the study.

The imaging data from the study (A) were used for the mouse liver tissue samples.

Normal male Lewis rats (Charles River, France) weighing 300-400 g and aged three months were used for in-vivo animal studies (n = 6/group). They were randomly housed in groups of three and given free access to food and water. The cages were maintained in a conventional animal facility under constant environmental conditions, including a twelve-hour light/dark cycle, a 21 ± 2 °C temperature, and a 45–65% relative humidity. The animals were euthanized humanely using an overdose of isoflurane with exsanguination.

Normal pig liver tissue samples were also collected for the study. The Prestice black-pied pigs, weighing 25-33 kg and aged three months, were used (n = 6; three males and three females). Pigs were kept in a conventional animal facility under constant environmental conditions with a twelve-hour light/dark cycle, room temperature of 21 ± 3 °C, and 60% relative humidity. General anesthesia was induced and maintained by intravenous injection of 10mg/kg ketamine (Narkamon-Spofa, Prague, Czech Republic), 5 mg/kg azaperone (Strensil - Jannsen Pharmaceutica NV, Beerse, Belgium), and 1 mg of atropine (Atropine Biotika - Hoechst Biotika, Martin, Slovak Republic), followed by intravenous injection of a 1% mixture of 5-10 mg/kg propofol

(Fresenius Kabi Norges, Halden, Norway). Under general anesthesia, animals were sacrificed with intravenous administration of potassium-rich T61 solution (MSD Animal Health, Kenilworth, NJ, USA) (Palek et al. 2020).

Normal human liver samples were collected in 2019 during liver surgeries at the University Hospital Jena. The human samples consisted of six individuals, two males and four females aged between 45 and 59 years, with normal liver morphology. The collection of human liver samples was supervised by Prof. Dr. Med. Utz Settmacher (Head of the Department of General, Visceral, and Vascular Surgery, University Hospital Jena, Jena, Germany) and PD. Dr. med. Hans-Michael Tautenhahn (previously UKJ and now Deputy Head of Hepatobiliary Surgery and Visceral Transplantation, Clinic and Polyclinic for Visceral, Transplantation, Thoracic and Vascular Surgery, University Hospital Leipzig, Leipzig, Germany). A board-certified hepato-pathologist, PD Dr. Med. Olaf Dirsch, Unfallklinikum Berlin., confirmed the absence of abnormal pathological findings such as fibrosis or steatosis.

3.3. Ethics statement

All procedures in the animal experiments were carried out in compliance with the German Law on the Protection of Animals/European Communities Council Directive (Directive 2010/63/EU), animal welfare guidelines, and the ARRIVE Guidelines for Reporting Animal Research.

The studies involving mice and rats were approved by the Thuringia State Office for Food Safety and Consumer Protection, Thuringia, Germany. Approval number for the mouse study: UKJ-19-020 (Albadry et al. 2022), and for the rat study Reg.-Nr.02-043-10.

The pig study was approved by the Commission of Work with Experimental Animals under the Czech Republic's Ministry of Agriculture, project ID: MSMT-15629/2020-4.

The human samples were collected at the University Hospital Jena during clinically indicated liver surgeries in 2019. The human study was approved by the institutional review board of the University Hospital of Jena, Germany (ethical vote: UKJ_2018-1246-Material). This ethical approval certifies that the study was performed according to the ethical standards in the Declaration of Helsinki.

3.4. Pharmacokinetics assessment

3.4.1. Drug cocktail injection

In experiment A, a combination of caffeine, midazolam, and codeine (at doses of 5 mg/kg, 2 mg/kg, and 2 mg/kg, respectively) was applied (Albadry et al. 2022). This drug cocktail is a commonly used combination of test compounds for studying pharmacokinetics, thereby indirectly measuring the activity of specific CYP isozymes (Schenk et al. 2017); see Table 1. To prepare the drug cocktail, 200 µl of sterile water was mixed with each drug to achieve the desired concentration (1

mg/ml for midazolam and codeine and 2.5 mg/ml for caffeine). The resulting three aliquots were combined to create a total volume of 600 µl. The amount of the drug cocktail given to a mouse was determined based on its weight, with a recommended amount of 180 µl/30 g of body weight. The administration of the drug cocktail was carried out via i.p injection. This method was preferred over oral and intravenous injections for several reasons. Firstly, it aimed to prevent any stress potentially caused to the animal by oral application via gavage. Secondly, it aimed to reduce any complications arising from the intravenous injection of the drug into the penis vein. Finally, it aimed to minimize the risk of drug contamination during injection and sampling from the same site, i.e., the tail vein, which may result in false-positive outcomes (Turner et al. 2011).

Table 1. Overview of drug concentration, dose, and source used to prepare the drug cocktail. (*dose per body weight; #needed volume of stock solution (µl)/100 g mouse diluted in a final volume of 200µl; *# final volume of diluted drug cocktail per 100gr body weight).

CYP test drug	Company	Respective CYP isoforms	Dose*(Schenk et al. 2017)	Concentration stock solution	volume stock solution#	final volume*#
Midazolam	B. Braun	CYP3A4	2 mg/kg	5 mg/ml	40 µl/100 g	600 µl/100 g
Caffeine citrate	Cooper	CYP1A2	5 mg/kg	25 mg/ml	20 µl/100 g	
Codeine phosphate hemihydrate	Lipomed	CYP2D6	2 mg/kg	5 mg/ml	40 µl/100 g	

For evaluation of drug elimination rates and blood levels, a total of ten micro-blood samples were collected from the animals at scheduled intervals over six hours (before injection, 15 minutes, 30 minutes, 1 hour (h), 1.5 h, 2 h, 2.5 h, 3 h, 4 h, and 6 h). The blood samples were collected from the tail vein using 9 µl heparinized calibrated end-to-end capillary tubes (Minicaps, Hirschmann). The accuracy was 0.5%, and the CV was less than 1%.

3.4.2. Ultra-performance liquid chromatography-tandem mass spectrometry (UPLC-MS/MS)

The concentration of the parent drugs and their metabolites was determined in heparinized whole blood, as described previously by Albadry and co-workers (Table 2) (Albadry et al. 2022). The measurement was conducted utilizing three specialized and highly sensitive UPLC-MS/MS methods using an Acquity UPLC System coupled to either the Xevo TQ-XS or TQ-S detector, both manufactured by Waters in Eschborn, Germany. The 9µL capillaries were completely shredded using an OMNI Bead Ruptor 24 (Bebensee, Germany) with a Yttrium-coated ceramic sphere. After that, they were enhanced with the corresponding deuterated internal standards: 12.5 ng/mL midazolam-d4 and OH-Midazolam-d4, or 250 ng/mL caffeine-d9, or codeine-d6, norcodeine-d3, codeine-6-glucuronide-d3, morphine-3-glucuronide-d3, and morphine-d6 (5.5 ng/mL each in whole blood). Following the process of protein precipitation and liquid/liquid extraction, the diluted supernatant was injected into the UPLC machine. A distinct

chromatographic technique was employed for each test substance. The midazolam/OH-Midazolam analysis was performed using a Waters CSH C18 1.7 µm, 2.1 x 150 mm column maintained at a temperature of 50°C. The process of gradient separation was performed within 6 minutes. A Waters BEH-Phenyl 1.7 µm, 2.1 x 100 mm column, maintained at a temperature of 40°C, was utilized for gradient separation of caffeine, completed within 2.5 minutes. A Waters HSS T3 column measuring 2.1 x 150 mm and having a pore size of 1.8 µm, maintained at a temperature of 50°C, was selected for gradient separation of codeine and metabolites. The duration of the chromatographic process was 9 minutes. The mass spectrometer was operated in ESI+ mode, monitoring three transitions in SRM for each analyte and two for the internal standards. The lower limits of quantification for caffeine were 10 ng/mL, while for all other analytes, it was at least 1.0 ng/mL. A multi-point matrix calibration was performed for each analyte. All methods were certified according to the DIN EN ISO 15189 standard. Midazolam, OH-Midazolam, and Opiates underwent accreditation for forensic use under DIN EN ISO 17025.

Table 2. A list of metabolites selected to assess CYP activity *in vivo* for indirect pharmacokinetic analysis.

Model reaction	CYP enzymes	Measured metabolite
Midazolam	CYP3A4	OH-Midazolam
Caffeine	CYP1A2	No metabolites
Codeine	CYP2D6	Norcodeine, Codeine-6-Glucuronide, Morphine-3-Glucuronide, Morphine)

3.4.3. Pharmacokinetic analysis

3.4.3.1. Area under the curve (AUC)

As described by Albadry and co-workers, the time course for clearance of the three test drugs after drug cocktail injection was parameterized for each replicate, assuming that there is an exponential decay after an increase to a maximum turning point. The experimental data was fitted using the function $\mathbf{x}(\mathbf{t}) = \mathbf{t} \cdot \mathbf{e}^{\mathbf{B}-\mathbf{At}}$ with parameters A and B (Albadry et al. 2022). The Python toolbox lmfit (Newville et al. 2016) was used to independently estimate these parameters for each replicate via least squares minimization. From each fitted curve, the peak concentration $\mathbf{x}_{\mathbf{peak}}$, the time of peak concentration $\mathbf{t}_{\mathbf{peak}}$, the time it took for the concentration to decrease by half (half-life) $\mathbf{t}_{1/2}$ and the area under the curve (AUC) was calculated (Figure 7).

The AUC was computed explicitly for the decay phase. This involved calculating the integral from the maximum turning point to t=6h of the fitted curve with scipy (Virtanen et al. 2020). The peak time $\mathbf{t}_{\mathbf{peak}}$ was calculated by minimizing the function $-\mathbf{x}(\mathbf{t})$ where x_peak represents the corresponding peak concentration at t_peak ($\mathbf{x}_{\mathbf{peak}} = \mathbf{x}(\mathbf{t}_{\mathbf{peak}})$).

The half-life time $\mathbf{t_{1/2}}$ was calculated by measuring the time it took for the peak concentration to decrease by half. For this, the equation $\frac{\mathbf{x_{peak}}}{\mathbf{2}} - \mathbf{t} \cdot \mathbf{e^{B-At}} = \mathbf{0}$ was solved for $\mathbf{t}$, whereby the half-life time results in $\mathbf{t_{1/2}} = \mathbf{t} - \mathbf{t_{peak}}$.

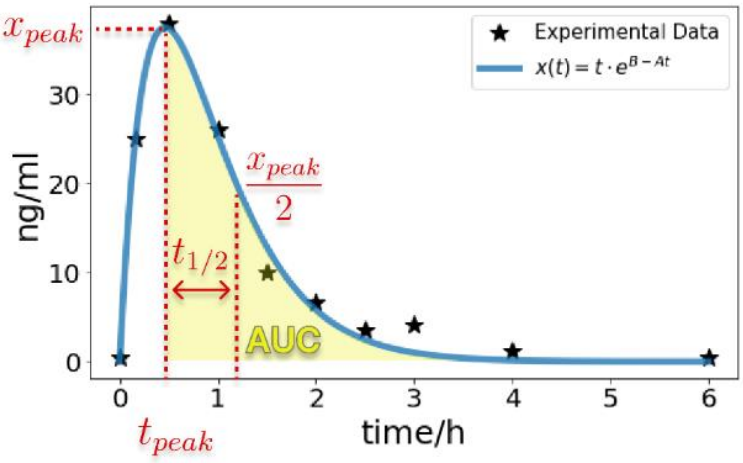

Figure 7. Pharmacokinetic parameters are computed by fitting exponential decay curves to the experimental data. The graph displays sample data from codeine-6-glucuronide control replicate 4 with parameters A=2.168 and B=5.397. The following pharmacokinetic parameters have been extracted: peak concentration $\mathbf{x_{peak}}$, time of the peak concentration $\mathbf{t_{peak}}$, half-life $\mathbf{t_{1/2}}$, and area under the curve from the maximum (AUC). "Reproduced with permission from Springer Nature" (Albadry et al. 2022).

3.4.3.2. Bayesian uncertainty quantification

The solution of an ordinary differential equation (ODE) $\dot{\mathbf{x}} = (\mathbf{1} - \mathbf{A} \cdot \mathbf{t}) \cdot \mathbf{e^{B-A \cdot t}}$ was interpreted as model $\mathbf{x(t)}$, and implemented in the Systems Biology Markup Language (SBML) format introduced by (Hucka et al. 2003;Keating et al. 2020). To create a parameter estimation problem, a PEtab parameter estimation problem (Schmiester et al. 2021) was generated using yaml2sbml, a tool developed by (Vanhoefer et al. 2021). Parameter estimation was performed using maximum likelihood estimation. Assuming independent additive normally distributed noise $\boldsymbol{\sigma}$, the likelihood function $\mathbf{L(\theta)}$ was calculated.

$$\mathrm{L}(\theta, \sigma) = \prod_{\mathrm{j}=1}^{\mathrm{N}} \prod_{\mathrm{k}=1}^{\mathrm{T}} \frac{1}{\sqrt{2\pi}\sigma} \exp\left(-\frac{\left(\mathrm{x}(\mathrm{t_k}, \theta) - \mathrm{m_j}(\mathrm{t_k})\right)^2}{2\sigma^2} \right),$$

where N represents the number of replicates conducted at T distinct measurement time points. $\mathbf{x(t_k, \theta)}$ represents the solution of the ODE while $\mathbf{m_j(t_k)}$ represents the measurement value of the j-th replicate at the time point $\mathbf{t_k}$. The likelihood function or probability density is encoded in the PEtab format and was employed to quantify Bayesian uncertainty. A uniform prior distribution within the interval [0, 100] was employed for the parameters A and B. Similarly, the previous for $\boldsymbol{\sigma}$ was consistently selected within the range of [0, 1000].

The parameters were sampled using Markov Chain Monte Carlo (MCMC) with the pyPESTO software package (Schälte et al. 2021). The adaptive parallel tempering sampler (Vousden et al. 2016), consisting of four chains and 200,000 samples, was conducted to evaluate the posterior distribution. To ensure the accuracy of our results, we used the Geweke test (Geweke 1991) to check the convergence of the MCMC chains and remove the burn-in samples. If the Geweke test recommended a smaller number, we cut the initial 100 samples to ensure that only samples from the converged chain were included in the ensemble. The convergence of the chains was also inspected visually and via computation of the Effective Sample Size (ESS) to ensure reliability. All chains had an ESS of over 13,900 samples. An ensemble of parameters was generated using the posterior distribution of the parameters in pyPESTO and then simulated using AMICI (Fröhlich et al. 2021). The credibility intervals of the posterior prediction distributions for the model outputs were calculated using forward simulations. All the necessary files, including the comprehensive data, the SBML model, the YAML file that outlines the parameter estimation problem, the complete parameter posterior sample, the estimated parameters, AUC values, half-lives, and a visualization of the sampling traces, are available on FAIRDOMHUB [https://doi.org/10.15490/FAIRDOMHUB.1.STUDY.1070.1].

3.5. Histology

3.5.1. Hematoxylin-Eosin (HE) staining

The liver samples were fixed in 5% neutral buffered formaldehyde (PZN 02653137, Otto Fischer GmbH & Co. KG, Germany) and then embedded in paraffin. Sections of 3µm thickness were cut. Some were subjected to HE-staining to evaluate steatosis, whereas others were used for immunohistochemistry. For HE staining, paraffin-embedded sections were subjected to deparaffinization using xylol and rehydration using a descending ethanol series. The sections were then rinsed with distilled water and stained with hematoxylin (CS700, Dako, Denmark) at room temperature for 15 minutes. Following the staining, the sections were washed and submerged in tap water for 15 minutes. Eosin (HT110132, Sigma-Aldrich, Germany) was applied to the sections for 2 minutes at room temperature. Finally, the slides were dehydrated, mounted, and covered using coverslips.

The stained sections were digitized at 40x magnification using a whole slide scanner (L11600, Hamamatsu, Japan) equipped with the NDP.view2Plus Image viewing software (Version U12388-02).

3.5.2. Qualitative steatosis assessment

A qualitative assessment of the type and distribution of steatosis was performed on WSI obtained from HE-sections. Based on the size of lipid droplets in hepatocytes, we distinguished between micro- and macrovesicular steatosis as well as the mixed pattern. Steatosis was also analyzed based on zonation patterns such as periportal, midzonal, and pericentral steatosis. In mouse livers, the intrahepatic distribution of steatosis was studied by analyzing one section from each of the four collected liver lobes.

3.5.3. Image analysis-based steatosis quantification

In order to determine the severity of steatosis, we analyzed sections from four distinct liver lobes of the same animal (Albadry et al. 2022). Our objective was to increase the relative sample size to ensure the validity of our findings. The mean severity of steatosis was calculated based on the total surface area occupied by each lobe, which is proportional to the surface area covered by lipid droplets, including macro- and microvesicular steatosis.

The severity and extent of steatosis were measured using Histokat, a proprietary software based on a machine-learning algorithm developed by Fraunhofer MEVIS, Germany. The algorithm splits the entire slide scan into small square tiles of a predetermined size. By utilizing a minimum of 30 tiles per image from the four separate liver lobes on one section and various representative images of the series, the software was trained to recognize single events such as lipid droplets (event recognition algorithm) or specific patterns (pattern recognition algorithm).

We first evaluated the relative surface area in the WSI covered by lipid droplets, regardless of their size (Figure 8B and C). Figure 8A displays the results for a normal liver.

Next, we utilized a pattern recognition algorithm (generic classification 128) to determine the relative surface area covered by hepatocytes containing lipid droplets. We then calculated the relative surface area covered by micro- and macrovesicular steatotic hepatocytes separately.

The sum of these areas gives the total surface area covered by steatotic hepatocytes (Figure 8E and F). Figure 8D displays the results for a normal liver.

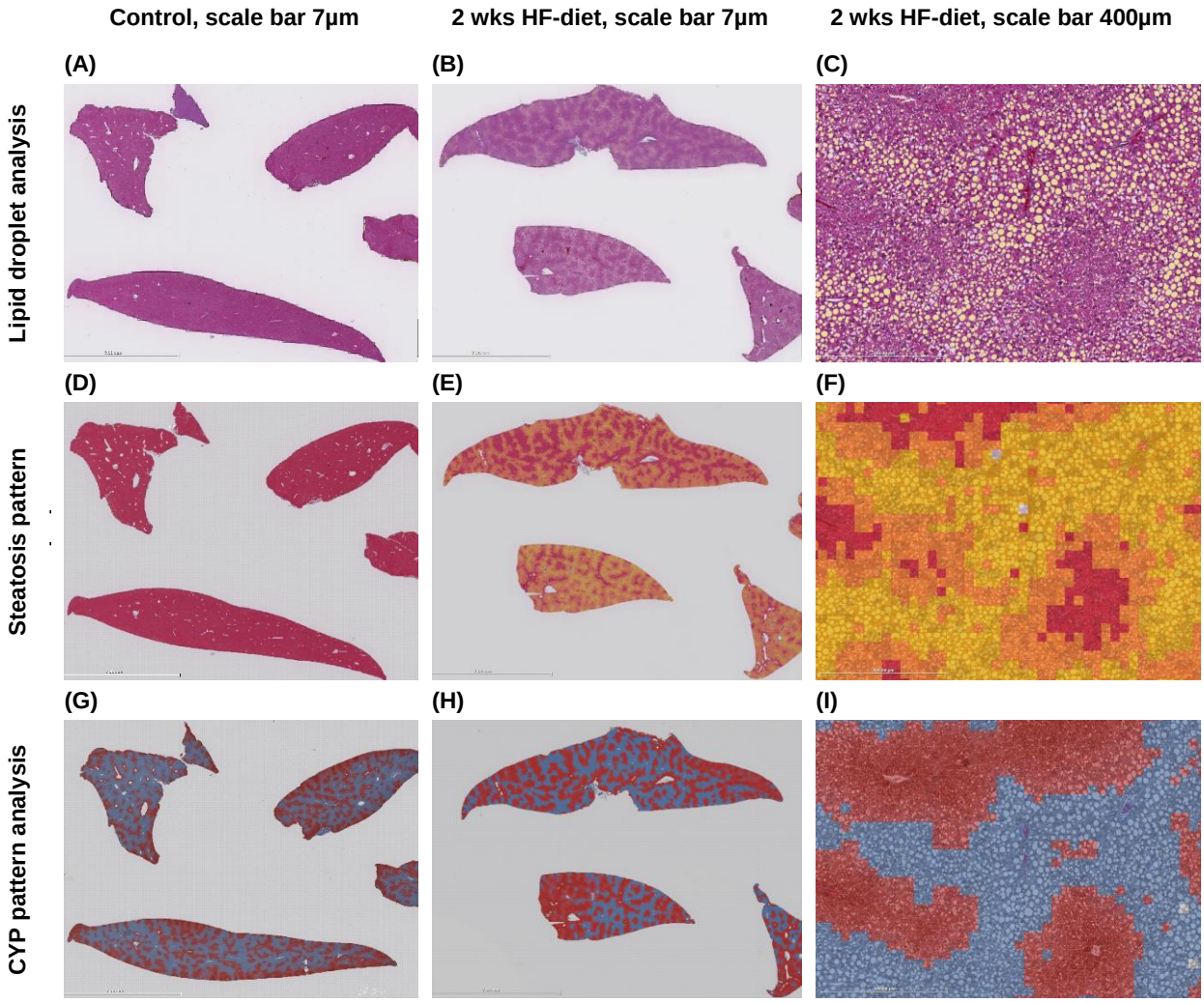

Figure 8. Image analysis of WSI with sections from four different liver lobes using Histokat event recognition and pattern recognition algorithm. (A) An overlay WSI of a normal liver with lipid droplets color-coded in yellow. (B, C) An overlay WSI of a steatotic liver with lipid droplets color-coded in yellow. (D) An overlay image of a normal liver with different patterns color-coded for quantification. (E, F) Overlay images of a steatotic liver with different patterns color-coded for quantification. Square tiles are classified into three color classes (orange for microvesicular steatosis, yellow for macrovesicular steatosis, and red for non-steatotic hepatocytes; the lumen of the vessels was excluded). (G) An overlay WSI of normal liver following color-coding the immunohistochemical visualization of CYP3A4 zonal expression. (H, I) Overlay images of the steatotic liver following color-coding of the immunohistochemical visualization of CYP3A4 zonal expression. Square tiles are categorized into two color classes (blue for the CYP-negative or mild-stained hepatocytes and red for strong to moderate CYP-stained hepatocytes). “Reproduced with permission from Springer Nature” (Albadry et al. 2022).

3.5.4. Immunohistochemistry

Immunohistochemistry was conducted using 3 µm thick liver tissue sections fixed in formalin and embedded in paraffin. We employed different antibodies to detect CYP3A4, CYP1A2, CYP2D6, CYP2E1, and GS (Table 3). The liver tissue sections underwent deparaffinization and rehydration

using descending ethanol concentration. Antigen retrieval was then carried out with Trisodium-citrate buffer (ph 6.1) in a steamer at 100°C for 30 minutes. The sample was then allowed to cool for 20 minutes. Peroxidase blocking was performed on the tissue segment to inhibit the activity of the endogenous peroxidase enzyme. A commercially available protein block (ab64226, Abcam, Germany) was used to inhibit non-specific binding to hydrophobic protein side chains or Fc receptors in the tissue. The tissue slides were incubated with the respective CYP antibody overnight at 4°C, as shown in Table 3. For rabbit polyclonal primary antibodies (CYP3A4, CYP2D6, and CYP2E1), the signals were amplified using a Rabbit-specific HRP/DAB IHC detection system (ab236469, Abcam, Germany) for 40 minutes at room temperature. For mouse monoclonal primary antibodies (CYP1A2 and GS), primary antibodies were first biotinylated using the Dako Animal Research Kit Peroxidase (K3954, Dako, Denmark). In this instance, an extra step of blocking was carried out using the Avidin/Biotin Blocking kit (ab64212, Abcam, Germany) before the application of the biotinylated primary antibody. Subsequently, the Avidin-HRP complex was applied.

The reaction was visualized by applying the 3,3′-Diaminobenzidine (DAB)-chromogen for 3 minutes at room temperature. The counterstaining was performed using Dako hematoxylin (CS700, Dako, Denmark) for 6 minutes. A negative reagent-control slide was included in each run using identical techniques but without applying the primary antibody.

Table 3. List of CYP antibodies employed for IHC-detection of CYP and GS spatial distribution and zonal expression pattern in liver tissue sections (m for mouse, r for rat, p for pig, and h for human).

Antibody	Company	Order-Nr	Dilution	Detection systems
Anti-CYP2D6 (Rabbit polyclonal antibody)	Abcam, Germany	ab230690	1/3000 (m), 3000 (r), 1/2000 (p), 1/200 (h)	Rabbit-specific HRP/DAB Detection IHC Detection Kit - Micro-polymer (ab236469, Abcam, Germany)
Anti-CYP2E1 (Rabbit polyclonal antibody)	Sigma-Aldrich, Germany	HPA009128	1/400 (m), 1/300 (r), 1/800 (p), 1/800 (h)	
Anti-CYP3A4 (Rabbit polyclonal antibody)	Abcam, Germany	ab3572	1/2000 (m), 1/2000 (r), 1/1000 (p), 1/1500 (h)	
Anti-CYP1A2 (Mouse monoclonal antibody)	Abcam, Germany	ab22717	1/500 (m), 1/200 (r), 1/2000 (p), 1/2000 (h)	Dako Animal Research Kit Peroxidase for Mouse primary antibody, (K3954, Dako, Denmark)
Anti-GS (Mouse monoclonal antibody)	Merck, Germany	MAB302	1/1000 (m), 1/1000 (r), 1000 (p), 1/1000 (h)	

3.5.5. Qualitative assessment of CYP expression

To perform a qualitative assessment, we evaluated the zonal distribution of the CYP signal, with specific attention paid to its localization within periportal, midzonal, and pericentral areas in the liver lobules. We also classified the signal intensity as mild, moderate, or strong.

3.5.6. Image analysis-based quantification of zonal expression of CYP enzymes

To perform a quantitative assessment of CYP zonal expression, we used the HistoKat generic 128 algorithm, which was also used for steatosis analysis. This algorithm was utilized to determine the relative surface area of hepatocytes expressing a certain CYP signal (Figure 8H and I). For a normal liver, see Figure 8G.

3.5.7. Pipeline for automatic quantification of lobular geometries and zonation patterns in WSI

The image analysis pipeline involved several successive processes, including detecting the region of interest (ROI) from the WSIs (where ROI represents large contiguous tissue regions), image registration, stain separation, and segmentation of liver lobules. The WSIs were supplied as RGB images shown in NDPI format. HE and hematoxylin 3,3′-Diaminobenzidine (HDAB)-stained WSI for GS, CYP1A2, CYP2D6, GYP2E1, and CYP3A4 were provided for each subject. All WSIs of a singular subject were derived from a series of consecutive sections.

3.5.7.1. Region of Interest Detection

First, the tissue samples on the WSIs, provided in NDPI format, were annotated using QPath. The slide images were imported onto the lowest resolution level using an open slide (Goode et al. 2013). The images were then converted to grayscale and subjected to thresholding using a binary threshold. The contour detection was applied to convert the binary mask into polygons, subsequently enabling an in-depth analysis of the tissue annotation. The polygons were meticulously examined and assigned based on their inclusion of the coordinates corresponding to the tissue annotation.

Subsequently, the bounding boxes of the assigned polygons were utilized to import the ROI of the liver tissue from the source image in full resolution. The ROIs were stored in the OME-TIFF format. Subsequently, the bounding boxes of the assigned polygons were utilized to import the ROI of the liver tissue from the source image in full resolution. The ROIs were stored in the OME-TIFF format. In the case of mouse tissue, each slide comprised four ROIs, each representing a separate liver lobe. Once the ROI was detected, the ROIs were matched by assessing the similarity of the tissue mask created from Otsu's thresholding. However, the matching process was unsuccessful in cases where lobes had similar shapes, and the ROIs had to be mapped manually. Contour

detection and thresholding techniques were implemented using OpenCV (Bradski and Kaehler 2008).

3.5.7.2. Image registration

The images for each ROI set were registered using VALIS, a virtual alignment tool for multi-gigapixel pathology WSI developed by Gatenbee and his team in 2023 (Gatenbee et al. 2023). The default settings were used during registration, and the registered ROIs were saved in OME-TIFF format.

3.5.7.3. Stain separation

After the registration process, stain separation was performed, generating two distinct single-channel pictures for the H-stain and the DAB or E-stain, respectively. The images obtained were saved in the ZARR format with eight pyramidal layers. The color deconvolution algorithm proposed by Macenko et al. (2009) was employed for stain separation (Macenko et al. 2009).

3.5.7.4. Lobule segmentation

A conventional image analysis methodology was employed to segment the boundaries of the lobules. The image set for each subject and the ROI of the dataset were subjected to the following procedures:

(1) The DAB stain for the image sets (GS, CYP1A2, CYP2D6, GYP2E1, and CYP3A4) was loaded with a resolution level of 5 (equivalent to a magnification of 1.25x). The registered protein ROIs were stacked in a 5-channel image. Protein images with a foreground pixel count of less than 80% of the median foreground pixel count across all protein images were excluded from the analysis.

(2) The protein images were inverted to align bright sections with high absorbance (high expression). Pixels in which one of the channels was zero, specifically the background channel, were assigned a value of zero. Subsequently, image filters were implemented on each channel. Initially, a median filter was implemented, followed by convolution of the picture to achieve a resolution level of 6 (0.625x). Adaptive histogram normalization was employed to mitigate global disparities in illumination and staining. Subsequently, after applying a median filter, the image was convolved to a resolution level of seven (0.3125x). Additionally, each channel was normalized to the maximum intensity of that channel.

(3) OpenCV's super-pixelization implementation was used to segment the 5-channel images by merging comparable pixels into a larger superpixel.

(4) The image superpixels were sorted into two categories based on their pixel values - foreground and background. A superpixel was considered background if more than 10% of its pixels had a zero value.

(5) Foreground pixels were further classified into three zones - pericentral, midzone, and periportal - for better analysis and understanding. As a result, the superpixels were transformed into linear vectors consisting of 5-channels, with each element representing the mean intensity of the channel within the superpixel. The K-means algorithm implementation of scikit-learn (Pedregosa et al. 2011) was applied to cluster the vectors into three distinct clusters. The cluster labels were arranged in ascending order based on the Euclidean distance of the cluster centers. The ordered labels corresponded to the periportal, midzonal, and pericentral regions based on the high expression of CYPs in the pericentral zone and low expression in the periportal zone. The superpixel representation was employed to assign labels to each foreground pixel, classifying them as pericentral, periportal, or midzone.

    The background pixels were used to generate a mask, which was subsequently subjected to contour detection, resulting in the identification of vascular contours and tissue boundaries. The vascular contours were then categorized as pericentral and periportal. The binary mask was generated by transforming each contour. Furthermore, a second mask was generated by expanding the dimensions of this contour mask. The XOR operator calculated the disparity between the contour and the dilated mask. The utilization of the difference mask facilitated the identification of the neighboring pixels of the vessel within the foreground image. Each label (pericentral, midzone, periportal) was quantified. A higher number of pericentral labels was expected for pericentral vessels, while a lower number was anticipated for periportal vessels. Based on this reasoning, the count vectors for all vessels were clustered into two groups using the K-means algorithm.

(6) A grayscale image was generated by combining the clustered foreground and vessel outlines. The pericentral vessels were assigned a color of black (zero), whereas the periportal vessels were assigned a color of white (255). The foreground zones were uniformly distributed throughout the grayscale spectrum, with the pericentral and periportal zones being characterized by dark and light, respectively.

(7) The grayscale image was skeletonized using an OpenCV version of a thinning algorithm. The remaining layers accurately depict the central positions of periportal zones and vessels, thus marking the potential boundaries.

(8) The line segments that could be polygonized were extracted from the skeletonized images. A line segment comprises neighboring pixels, each having a maximum of two neighbors in the

intersecting pixels. A pixel-walking method was implemented, resulting in the generation of line segments that include the connected pixels. The algorithm iteratively expands a line segment. The algorithm examines the adjacent pixels of the most recent appended pixel for a specific line segment. Appending a neighbor to a segment is repeated if only one neighbor is identified. The section is ended if no neighbor is identified. The segment is terminated if several neighbors are identified, and new segments are generated for each neighbor. Upon completion of a segment, the subsequent beginning segment is selected from the designated list of initial segments. The procedure above is iterated until there are no initial segments left.

(9) Finally, the shapely library was employed (Gillies et al. 2023) to polygonize the line segments obtained in the preliminary stages. This process involved excluding all line segments that did not form a complete closed circle. The resulting polygon represented the shape of the initial set of line segments and served as a valuable tool for subsequent analyses.

3.5.7.5. Generating the portality map

To analyze the gradients of expression, we calculated the relative position of each pixel within a lobule. The portality p was depicted as

$$p(x,y) = 1 - \frac{dc(x,y)}{dc(x,y)+dp(x,y)} \in [0,1],$$

where dc and dp are the distance of a position to the nearest central and portal pixel, respectively. A periportal and pericentral border mask were constructed for each identified lobule. Within the pericentral boundary mask, any pixels within a central vessel or having a weighted intensity across all channels falling within the 99% quantile were designated as false. Within the portal boundary mask, any pixel that fell outside the lobule boundary or was situated within a portal vessel was assigned a false value. The OpenCV distance transform function was used to calculate the portal and center distance of these masks. This function computes the distance between each pixel and the closest background pixel. The lobule border polygon and the vessel polygons were used to create the periportal and pericentral masks. The distance transformation for these masks was subsequently computed using the OpenCV implementation.

For each protein, the intensity was background corrected and normalized by

$$I_N(x,y) = (I(x,y) - I_{bg})/(I_{max} - I_{bg}) \in [0,1],$$

Where I(x,y), Ibg, and Imax represent the pixel intensity, background intensity, and the maximum intensity of the slide, respectively, the maximum intensity was assumed to be the 99% quantile of the foreground pixels. The background intensity was estimated for each subject using the 20% percentile of the foreground pixels on the GS slide. The expression of GS is limited to a tiny region

of the lobule, whereas the rest serves as a robust background estimate. The normalized intensity and portality of each pixel were recorded in a data frame for further investigation.

3.5.7.6. Lobular geometries

The geometric parameters for each identified lobule were calculated using the polygon representing the lobule boundary. These values include perimeter, area, compactness, and minimum spanning distance.

3.5.8. Calculation of the number of required lobules

3.5.8.1. Geometric parameters

The number of lobules (n) required for quantifying lobule geometries was calculated using the sample size determination method for estimating a population mean. The methodology relies on the margin of error (ME), which determines the desired degree of accuracy for the results. It also considers a confidence level of 95%, denoted as α = 0.05, which indicates the desired confidence level for the results. Additionally, it considers the estimated values for the mean and standard deviation (sd).

$$P\left(\left|\underline{x} - \mu\right| > z_{\alpha/2} \cdot \sqrt{\frac{N-n}{N} \cdot \frac{\sigma^2}{n}}\right) = \alpha$$

$$z_{\alpha/2} \cdot \sqrt{\frac{N-n}{N} \cdot \frac{\sigma^2}{n}} = d = \mu \cdot ME$$

$$n = \frac{1}{\frac{d^2}{z_{\alpha/2}^2 \cdot \sigma^2} + \frac{1}{N}}$$

For an analyzed subject and a geometric parameter, N represents the total number of lobules, μ is the mean of the parameter over all lobules of a subject, σ the corresponding sd (provided in Appendix Tables S 8 - S 10), d represents the distance to the mean based on the ME, and z is the z statistic for a given α value.

3.5.8.2. Zonation patterns

The quantification of zonation patterns was determined by calculating the number of lobules (n) similar to the geometric parameters. One n was determined for every subject and protein in the 12 zones. The mean μ represents the mean intensity value for a specific location over the lobule, σ represents the standard deviation, and N represents the total number of lobules for a given subject. A margin of error ME of 20% and a confidence level of 95% (α=0.05) were used for the calculation.

3.5.8.3. Normalized intensity of CYP expression

The normalized expression of each lobule was calculated for each protein by summing all of the normalized intensities in that lobule. We then used the mean (μ) and standard deviation (σ) of the normalized expression for all lobules in a subject to determine the required number of lobules (n), where N is the total number of lobules for that subject. A margin of error (ME) of 20% and a confidence level of 95% (α=0.05) were used for the calculations.

3.6. Hepatic triglyceride assessment

As described before (Albadry et al. 2022), hepatic TG concentration was assessed using a TG quantitative colorimetric assay kit per the manufacturer's instructions (ab65336 Abcam, Germany). Lipids were extracted from 100 mg of snap-frozen liver tissue through homogenization in a 1 ml 5% Igepal/double-distilled water solution. The samples were gradually heated in a thermomixer at 95°C for four minutes before being cooled and then re-heated to solubilize all triglycerides in the solution. Following centrifugation to remove insoluble material, the supernatants were diluted 1:10 with double-distilled water. All reactions were performed in duplicate. A transparent 96-well plate was utilized, and 50 µl of the respective samples, standard, and 50 µl of sample for background control were added. 2 µl lipase and assay buffer were added for standard and sample wells, while 2 µl TG assay buffer was added to the sample background control. The reactions were incubated at room temperature with constant agitation for 20 minutes. After that, the triglyceride reaction mix was added to all reaction wells. The 96-well plate was then incubated in the dark at room temperature with constant agitation for 60 minutes. The output was measured on a microplate reader (Synergy™ Neo2 Multi-Mode Microplate Reader, BioTek Instruments Inc, USA) at OD570.

3.7. CYP activity assessment

The determination of CYP activity was performed using model reactions. These included ethylmorphine-N-demethylation (EMND), which serves as an indicator of CYP3A activity (Kleeberg and Klinger 1982), Ethoxycoumarin-O-Deethylation (ECOD) which indicates CYP1A, 2A, 2B, and 2C activity (Aitio 1978), Ethoxyresorufin-O-Deethylation (EROD) which represents CYP1A activity (Pohl and Fouts 1980), p-Nitrophenol-Hydroxylation (PNPH) which measures CYP2E1 activity (Chang et al. 2006), and Pentoxyresorufin-O-Depentylation (PROD) which reflects CYP2B activity (Pohl and Fouts 1980).

To prepare the samples, a 0.1 M sodium phosphate buffer (pH 7.4) was used to homogenize the liver samples (1:2 w/v). Subsequently, the homogenized samples were centrifuged at 9000 xg for 20 minutes at 4 °C. The resulting 9000g supernatants were used to assess the CYP activities.

The protein content was determined using a modified Biuret method, and the CYP activity was related to the protein content of the 9000g supernatant.

For each model reaction, the reaction mixture contained the 9000g supernatant, substrate, NADPH, MgCl2, glucose-6-phosphate, and buffer. The reaction was initiated by adding NADPH, and the samples were incubated at 37 °C for 5 minutes (EROD), 10 minutes (ECOD, PROD, EMND), or 30 minutes (PNPH), respectively. The reaction was then stopped by adding ice-cold trichloroacetic acid (ECOD, PNPH, and EMND) or methanol (EROD, PROD). The main metabolites were determined in the supernatant using photometric or fluorometric techniques. For PNPH and EMND, the main metabolites 4-nitrocatechol or formaldehyde were measured photometrically using Spekol 1100. The ECOD reaction was assessed fluorometrically by quantifying the concentration of the main metabolite 7-hydroxycoumarin. For EROD and PROD, the concentration of the main metabolite resorufin was determined fluorimetrically using RF-1502 (Shimadzu, Kyoto, Japan); see Table 4.

Table 4. Overview of model reactions used to assess hepatic CYP activity.

Model reaction	CYP enzymes	CYP-isoforms	Measured metabolite
Ethylmorphine-N-Demethylation (EMND)	CYP3A (Kleeberg and Klinger 1982)	3A1, 3A11, 3A13, 3A16, 3A2, 3A4	formaldehyde
Ethoxycoumarin-O-deethylation (ECOD)	CYP1A, 2A, 2B, 2C (Aitio 1978)	1A2, 2A1, 2A6, 2B1, 2B6, 2C11, 2C9	7-hydroxycoumarin
Ethoxyresorufin-O-deethylation (EROD)	CYP1A (Pohl and Fouts 1980)	1A1, 1A2	resorufin
p-Nitrophenol-hydroxylation (PNPH)	CYP2E1 (Chang et al. 2006)	2E1	4-nitrocatechol
Pentoxyresorufin-O-Depentylation (PROD)	CYP2B (Pohl and Fouts 1980)	2B1, 2B6,	resorufin

3.8. Statistical analysis

A descriptive ordinary one-way ANOVA was utilized to investigate the effects of the dietary induction protocol on TG levels (biochemical assay), steatosis severity (relative surface covered by lipid droplets, macro-, and microvesicular steatosis), CYP zonal expression levels (relative surface covered by a given CYP signal), CYP activity (model reaction), immunohistochemistry expression, and the AUC derived from the PK-analysis. Furthermore, the same test was employed to evaluate the CYP zonal expression across four distinct species (mice, rats, pigs, and humans). Tukey's multiple comparisons test was conducted using GraphPad Prism version 9.3.1(471) for Windows, GraphPad Software, San Diego, California USA, www.graphpad.com. The resulting

data was presented as mean ± sd. Statistical significance was considered when p-values were below 0.05.

Geometrical parameters were tested for significance using the Kruskal–Wallis and Mann–Whitney U tests with significance levels as follows: * $p<0.05$, ** $p<0.01$, *** $p<0.001$, **** $p<0.0001$.

3.9. Correlation analysis

The Pearson correlation coefficient (r) was employed to evaluate the potential linear correlation between steatosis severity, measured by lipid droplet analysis, relative percentage of hepatocytes containing lipid droplets, and CYP activity. The correlation analysis was conducted with a 95% confidence range and a two-tailed P value. GraphPad Prism was utilized to evaluate the linear relationship between macrovesicular and microvesicular steatosis and the area under the curve (AUC). A linear correlation (r-value) less than zero shows a negative correlation. In contrast, a positive correlation is indicated by an r-value greater than zero.

According to (Mukaka 2012), a correlation is deemed strong when the r-value is greater than 0.7, moderate when the r-value falls between 0.7 and 0.5, fair when the r-value falls between 0.5 and 0.3, and weak when the r-value is less than 0.3. This classification applies regardless of whether the coefficient is positive or negative.

The Pearson correlation coefficient was also used to compute the correlation matrix. The Benjamini and Hochberg method was employed to adjust the p-values for multiple testing. The R version 4.2.1 and the corrplot package were utilized for the analysis.

4. Results

4.1. Periportal steatosis affects certain parameters of zonated drug metabolism

4.1.1. Characterization and quantification of hepatic steatosis

4.1.1.1. Histology

All animals tolerated the dietary intervention, which consisted of a high-fat (HF), methionine, and choline-reduced diet without showing any apparent side effects. They did not experience any weight loss as observed when applying a methionine choline-deficient diet (Deng et al. 2014). The feeding regimen resulted in mixed steatosis, predominantly localized in the periportal and midzonal regions of liver lobules (Deng et al. 2014;Albadry et al. 2022). Moreover, a non-uniform heterogeneous distribution was observed within and between the liver lobes (Figure 9).

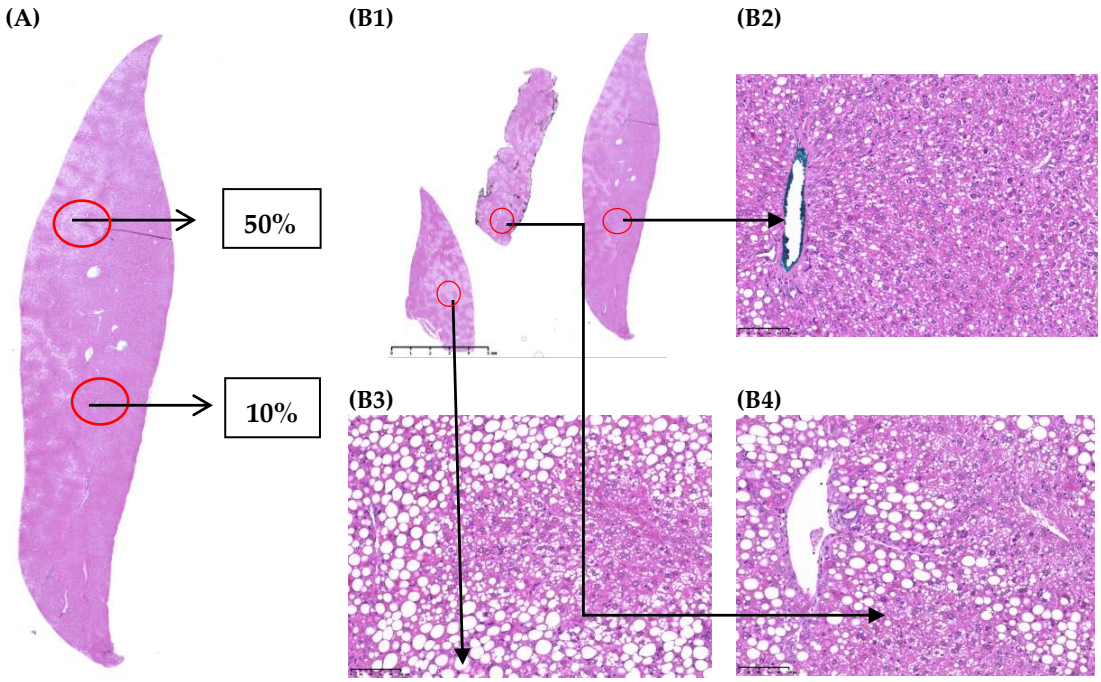

Figure 9. Inhomogeneous distribution of fat-laden hepatocytes in a mouse liver (animal-ID MNT-042); (A) Intralobar variation: in this lobe (left lateral lobe) the relative surface covered by fat-laden hepatocytes ranged from 10%-50%; (B) Interlobar variation: comparing regions of interest in 3 different lobes, the relative surface covered by steatotic hepatocytes ranged from 5% in the left lateral lobe (see B2), to 20% in the right superior lobe (see B4) and 60% in the left median lobe (see B3). “Reproduced with permission from Springer Nature” (Albadry et al. 2022).

The histological evaluation indicated a transition from predominantly micro- to predominantly macrovesicular steatosis over time. A mixed but predominantly microvesicular steatosis pattern

was observed when feeding the animals for two weeks. In the immediate vicinity of the portal tract, a small rim of hepatocytes was found to contain large fat vacuoles. However, most hepatocytes contained microvesicular lipid droplets in the outer periportal and midzonal areas.

The ratio of microvesicular to macrovesicular steatosis patterns was reversed when feeding the mice for four weeks. Large fat vacuoles were found to fill the hepatocytes in the periportal zone and part of the midzonal area. In contrast, a relatively small rim of hepatocytes in the midzonal to the pericentral area contained small lipid vesicles.

4.1.1.2. Image analysis-based quantification of steatosis

We utilized two distinct image algorithms to quantify the severity and pattern of steatosis.

First, we examined the relative surface area covered by lipid droplets, a commonly used method for image analysis-based severity assessment (Mashek 2020;Seebacher et al. 2020). In animals fed HF-diet for two weeks, the lipid droplets covered a relative surface area ranging from 8% to 11%. However, in animals fed HF-diet for four weeks, the relative surface covered by lipid droplets was significantly larger ($p = 0.001$). Although the "relative surface" difference was not high, it was still notable (9.3 ± 1.3 % versus 13.9 ± 2.7 %), as demonstrated in Figure 10A. However, this type of analysis may underestimate the impact of microvesicular steatosis, as a high number of hepatocytes containing small fat vacuoles may not contribute substantially to the relative surface.

Subsequently, we assessed the relative percentage of hepatocytes containing lipid droplets, which is a more accurate method compared to the traditional histological evaluation used in clinical practice. Clinicians estimate the relative number of hepatocytes containing lipid droplets, regardless of their size, which is a more reliable indicator of the severity of fatty liver disease (Brunt 2007). Steatosis was categorized as mild if it ranges between 5% and 33% of hepatocytes containing fat, moderate if it ranges between 33% and 66%, or severe if it exceeds 66% (Kleiner et al. 2005). The two-week feeding period resulted in severe steatosis compared to the rat model, as evidenced by the relative surface area covered by fat-laden hepatocytes exceeding 66% (Figure 10A). Applying a pattern recognition algorithm to determine the total area covered by fat-laden hepatocytes revealed no significant difference between the two groups that underwent either a two-week or a four-week steatosis-induction period. This finding was also observed in the TG analysis (Figure 10B).

Nevertheless, we could distinguish between micro- and macrovesicular steatosis by applying our pattern recognition algorithm. As previously mentioned, the short feeding duration was associated primarily with a microvesicular steatotic pattern. Microvesicular steatotic hepatocytes occupied approximately 48.6 ± 12.9% of the relative surface, while macrovesicular steatotic hepatocytes occupied 20.7 ± 7.1%, indicating a 2.4:1 ratio of micro-to macrovesicular steatosis. On the other

hand, the more extended induction period resulted in a macrovesicular steatotic pattern. Following a four-week feeding period, the relative surface covered by microvesicular steatotic hepatocytes was 33.4 ± 10.2%. In contrast, the relative surface covered by macrovesicular steatotic hepatocytes was 39.9 ± 8.6%, resulting in a ratio of 0.8:1. In other words, there was a substantial shift in the micro- to macrovesicular steatosis ratio.

This pattern illustrates how steatosis develops, beginning in the periportal region and progressing to the pericentral zone, where little lipid droplets accumulate. As more fat accumulates in the hepatocytes over time, the droplets grow more extensively, resulting in macrosteatosis, as previously reported by (Gluchowski et al. 2017).

4.1.1.3. Biochemical assessment of triglycerides

Biochemical assessment of severity showed a similar level of TG. After administering the steatosis-inducing diet, the average TG amount per 100 mg homogenized liver significantly increased. In both experimental groups, the TG concentration was at least twice as high as in the control group. We found that the lowest value was 192.7 nmol/100mg tissue in the two experimental groups compared to the mean of 99.6 ± 42.3 nmol/100mg tissue in the control group. This resulted in a highly significant difference between the control and experimental groups ($p = 0.0002$), as demonstrated in Figure 10B.

The mean TG level in the livers of animals fed for four weeks was higher than those fed for two weeks. After four weeks, the concentration was 296.1 ± 91.6 nmol/100mg of tissue, while after two weeks, it was 252.8 ± 43.0 nmol/100 mg of tissue. However, the difference between the two sets of animals was not statistically significant ($p=0.48$).

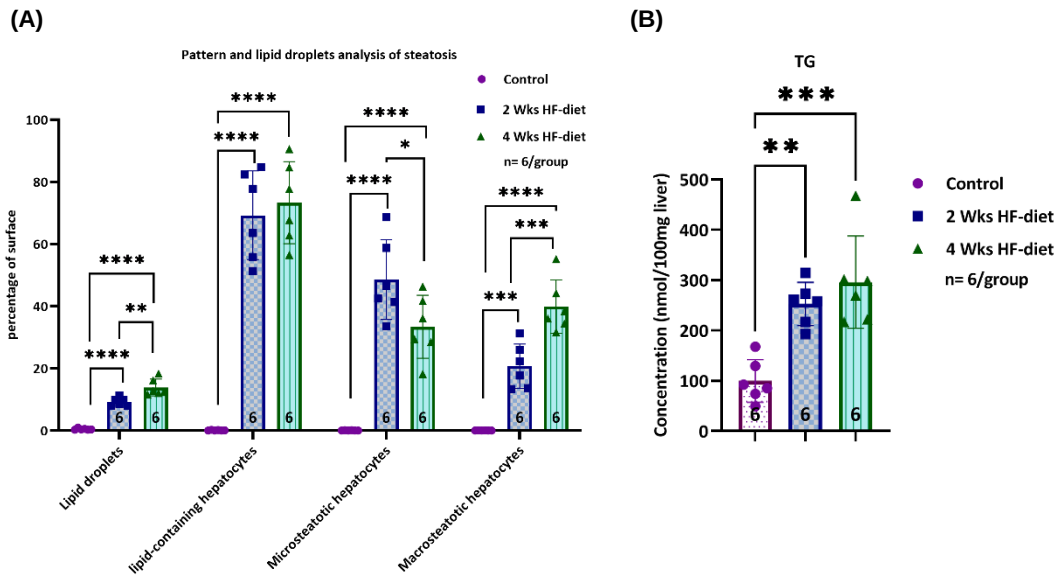

Figure 10. Overview of severity assessment of hepatic steatosis. (A) Image analysis using different algorithms detected specific differences in severity when subjecting animals either to two or four weeks of feeding the special diet. Analysis of lipid droplets revealed a significantly higher surface area covered by the droplets. When micro- and macrovesicular steatosis were separately assessed using a pattern analysis, a significantly larger surface area covered by microvesicular steatotic hepatocytes was observed after two weeks of feeding, while a larger surface area covered by macrovesicular steatotic hepatocytes was observed after four weeks of feeding. The total surface area covered by steatotic hepatocytes was similar in both groups. (B) Total triglyceride level depending on diet. Total triglyceride levels varied, with significantly higher levels observed in the HF-diet groups compared to the control group, but no significant differences were observed between the groups subjected to two and four weeks of HF-diet. (*significance level < 0.05, **significance level < 0.01, *** significance level < 0.001, **** significance level < 0.0001, sample size of each group displayed at the bottom of the bar). “Reproduced with permission from Springer Nature” (Albadry et al. 2022).

4.1.2. Zonal expression of CYP enzymes

Steatosis did not affect the zonal distribution and extent of CYP expression. As expected, CYP enzymes were expressed in the pericentral region, albeit with varying extent. Quantitative assessment of the relative surface area covered by CYP3A4-positive hepatocytes revealed no significant difference among the three groups (Figures 11 and 12).

CYP1A2 staining was characterized by a strong signal in the initial 2-3 lines of perivenous hepatocytes, followed by a moderate signal extending across the pericentral third of the lobule. The steatosis-inducing diet did not affect the pattern or extension of the signal (Figure 11C and 12A).

The zonal expression of CYP2D6 was observed throughout the whole lobules (panlobular). Nevertheless, the intensity of the signal was highest in the vicinity of the central vein. A total of 1-2 lines of hepatocytes stained with dark brown were detected in the vicinity of the central vein.

The hepatocytes that remained exhibited a moderate signal across the lobules. The steatosis-inducing diet did also not affect the pattern or extension of the CYP2D6 signal (Figures 11D and 12B).

The pattern of CYP2E1 staining was slightly different compared to CYP1A2. In the control and experimental groups, we observed 4 to 5 lines of hepatocytes presenting signals of strong intensity around the central vein. Also, for CYP2E1, the pattern and extension were not affected by the steatosis-inducing diet (Figure 11E and 12C).

The zonal expression of CYP3A4 exhibited a comparable pattern to that of CYP1A2. CYP3A4 staining showed a consistent pattern in the first 2-3 lines of hepatocytes surrounding the central vein and a moderate signal intensity in the pericentral area of the lobule. Upon calculating the relative surface covered by strong and moderate signals, we found no significant difference in the CYP3A4 surface between the three groups (Figure 11F and 12D).

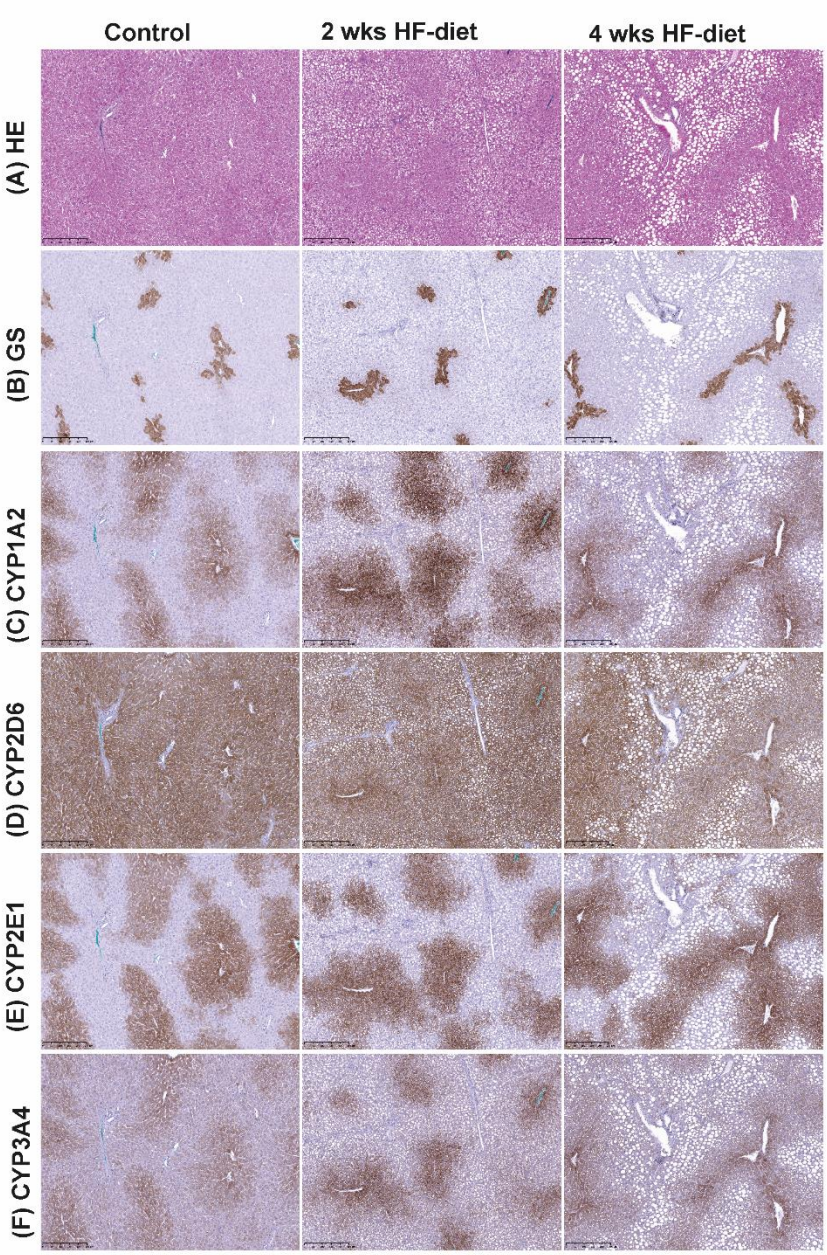

Figure 11. Visualization of steatosis and CYP expression in normal and experimental animals subjected to two weeks, respectively, four weeks of HF diet. (A) HE-staining shows periportal steatosis with a predominantly microvesicular pattern after two weeks of feeding and a predominantly macrovesicular pattern after four weeks of feeding. (B) Glutamine synthetase (GS)-staining was performed to mark pericentral hepatocytes for better discrimination of periportal from pericentral zones. (C) CYP1A2 staining also present in pericentral location without substantial differences in the distribution of positive signals between the three groups. (D) CYP2D6 expressed almost in the whole lobules with 1–2 lines of dark brown stained hepatocytes around the central vein with a similar pattern in all three groups. (E) CYP2E1 staining was present in pericentral location with 4-5 lines of hepatocytes presenting signals of strong intensity around the central vein, but also no differences between groups. (F) CYP3A4 was slightly different compared to CYP2E1 without substantial differences in the distribution of positive signals between the three groups. Scale bar 250µm. “Reproduced with permission from Springer Nature” (Albadry et al. 2022).

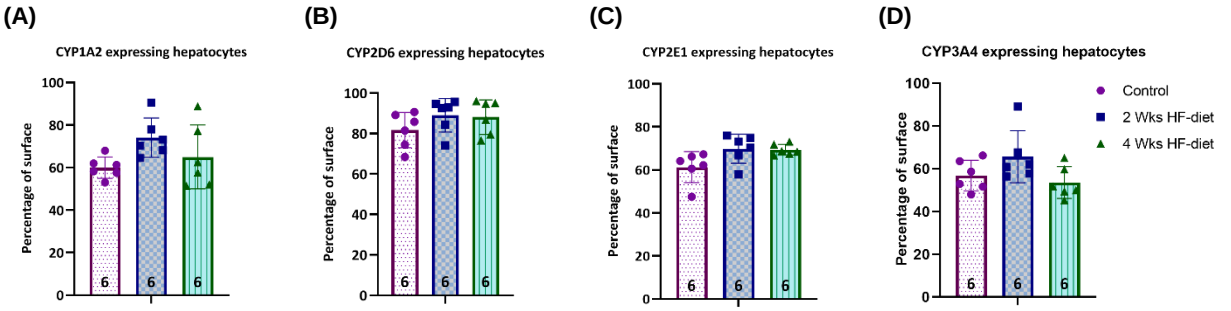

Figure 12. Quantification of zonal distribution of CYP expression using the pattern recognition algorithm (A, B, C, D). There was no significant difference in the expression pattern of CYP1A2, CYP2D6, CYP2E1, and CYP3A4 in terms of the relative surface covered by positively stained hepatocytes. The sample size of each group is displayed at the bottom of the bar. “Reproduced with permission from Springer Nature” (Albadry et al. 2022).

4.1.3. *Ex-vivo* activity of selected CYP enzymes

The activity of CYP in liver tissue was assessed by utilizing four model reactions that spanned various combinations of CYP enzymes. We first calculated the protein content per gram of liver and then correlated the activity to the mg protein in the tissue. The relative protein content of the normal control samples varied between 67.4 and 79.2 mg/ml (Figure 13A). In contrast, the steatotic liver samples had a significantly reduced relative protein content, ranging from 64.0 to 69.2 mg/ml after two weeks of feeding and from 62.2 to 69.2 mg/ml following four weeks of feeding. The activity of CYP1A (EROD assay), CYP3A (EMND assay), and CYP2E1 (PNPH assay) was affected by the duration of feeding (Figure 13 but not ECOD and PROD (Appendix Figure S 1). In the first step of the analysis, we investigated the influence of feeding duration on CYP activity. CYP3A activity, as measured by the EMND reaction, and CYP1A activity, as measured by the EROD reaction, were both significantly lower in the livers of animals that had been fed for four weeks compared to control tissue from healthy animals ($p = 0.029$ and $p = 0.005$, respectively) (Figures 4B and D). The activity of CYP2E1 was nearly twice as high in the livers obtained from animals fed for an extended period compared to the control group ($p = 0.0003$) (Figure 4C).

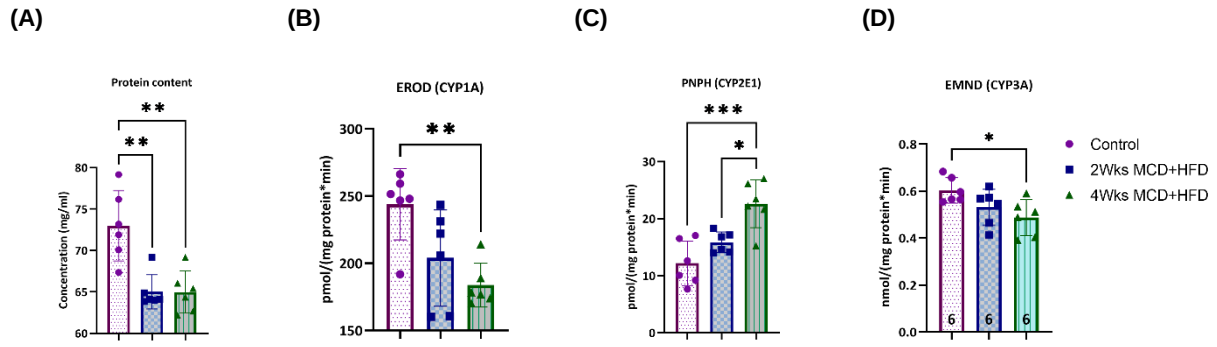

Figure 13. Overview of *Ex-vivo* CYP activity assessment. (A) The protein content in liver samples was considerably lower in steatotic samples compared to the control group, while both experimental groups had equal protein concentrations. (B) The EROD assay results indicated a notable decrease in CYP1A activity in the samples from animals exhibiting severe steatosis. (C) The PNPH assay for CYP1E1 activity revealed increased activity with increasing steatosis severity. (D) The EMND assay showed that the CYP3A activity was much lower in samples from animals with severe steatosis, as shown by the lipid droplet analysis**.** "Reproduced with permission from Springer Nature" (Albadry et al. 2022).

The severity of steatosis influenced the *ex-vivo* activity of CYP1A2 and CYP2E1. The linear correlation between the severity of steatosis and the CYP activity was calculated in the second step of the analysis using the lipid droplet quantification results of the individual animals. Consistent with our initial analysis, we observed a strong negative correlation between CYP1A activity and the EROD assay (Figure 14A1). A strong positive correlation was observed between the severity of steatosis and the activity of CYP2E1, as assessed using the PNPH assay (Figure 14A2). Additionally, we demonstrated a moderate negative correlation between the relative surface of hepatocyte-containing lipid droplets and CYP3A activity, as determined by the EMND assay (Figure 14A3).

The pattern of steatosis modulated the *ex-vivo* activity of CYP1A and CYP2E1. In the third step, we investigated the correlation between the prevalent pattern of steatosis and CYP activity. In contrast to the droplet analysis, the extent of microvesicular steatosis (%) showed a moderate negative correlation with CYP1A activity (Figure 14B1). However, it was not significantly correlated with the results of EMND and PNPH, reflecting primarily the activity of CYP2E1 and CYP3A (Figure 14B2 and B3). Additionally, the degree of macrovesicular steatosis exhibited a moderate correlation with CYP1A, a strong positive correlation with CYP2E1 activity, and no significant correlation with CYP3A (Figure 14C1-3).

Overall, specific characteristics of periportal steatosis significantly influenced the functionality of CYP enzymes located in the pericentral region of the hepatic lobule. There was a negative

correlation between the severity of steatosis and the activity of CYP1A and CYP3A, while there was a positive correlation with the activity of CYP2E1.

In addition to the severity, the steatosis pattern also influenced CYP activity. The activity of CYP1A exhibited a negative correlation with macrovesicular steatosis, while the activity of CYP2E1 had a positive correlation. The observations above indicate an intricate relationship between alteration in the periportal zone and the corresponding molecular response in the pericentral area.

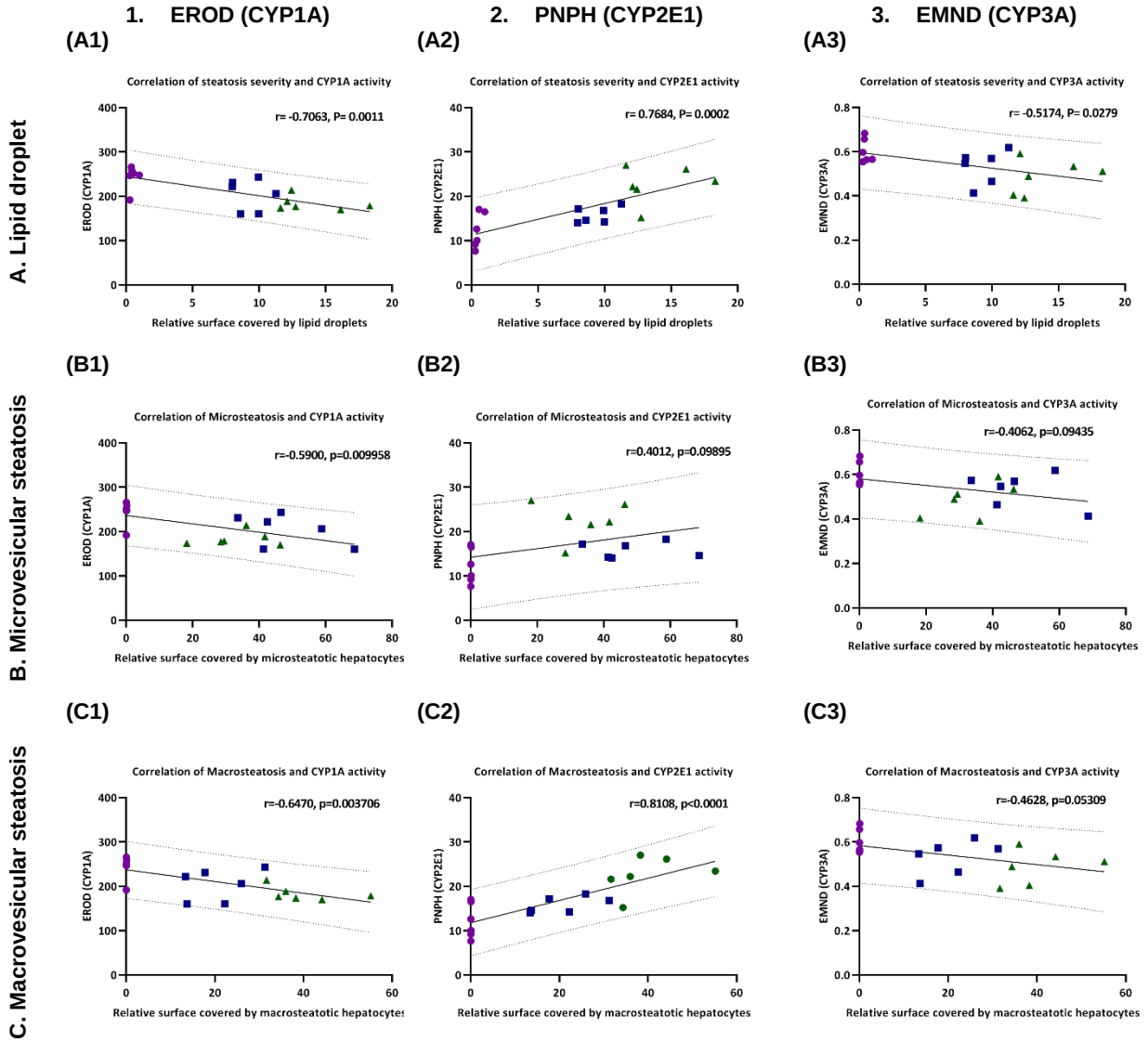

Figure 14. Correlation between steatosis severity and CYP activity. (Row A) Severity of steatosis as determined by lipid droplet analysis in percent of surface; (Row B) Extent of microvesicular steatosis, in percent of surface; (Row C) Extent of macrovesicular steatosis, expressed in percent. (Column 1) Correlation of steatosis type and severity with activity of CYP3A; (Column 2) Correlation of steatosis type and severity with activity of CYP1A; (Column 3) Correlation of steatosis type and severity with activity of CYP2E1. Control as magenta circles, two weeks HF-diet as blue squares, four weeks HF-diet as green triangles. “Reproduced with permission from Springer Nature” (Albadry et al. 2022).

4.1.4. Pharmacokinetic study (to assess the in-vivo activity of CYP enzymes)

First, we analyzed the drug clearance curves for all three experimental groups. Second, we calculated the half-lives, peak concentrations, and peak times for each drug (supplemental Table S 5) and compared the AUCs of the experimental and control groups. In the third and fourth experiments, we used the linear correlation to examine the effects of steatosis pattern and severity on the AUC.

As anticipated, the pharmacokinetic analysis revealed that all three drugs exhibited a comparable exponential clearance pattern. The drugs were eliminated within 4-6 hours, with the highest concentration observed within 15-60 minutes (Figure 15); for metabolites, see supplementary Figure S 3. The shaded region represents the 95% confidence interval derived from the Bayesian analysis. Credibility intervals that do not overlap show a significant variation in the dynamics at this particular moment. Nonetheless, when credibility intervals partially overlap in time, it becomes challenging to predict an overall different behavior.

The duration of feeding influenced the AUC of all three test drugs. We calculated the pharmacokinetic parameters and assessed each group for statistically significant disparities. AUC values were employed as a comprehensive tool for analyzing the time courses to draw definitive conclusions on overall variations between conditions. This parameter includes the time required to attain the maximum concentration (Cmax) and the half-life, making it the most appropriate for conducting a comprehensive analysis.

Two weeks of feeding, which resulted in primarily microvesicular steatosis, accelerated caffeine clearance, as seen by the smaller AUC. Notably, after four weeks of the same diet, the AUC levels returned to normal, suggesting they were becoming "tolerant" of the effect. Conversely, four weeks of feeding decreased the rate at which midazolam and codeine were eliminated, as seen by the larger AUC.

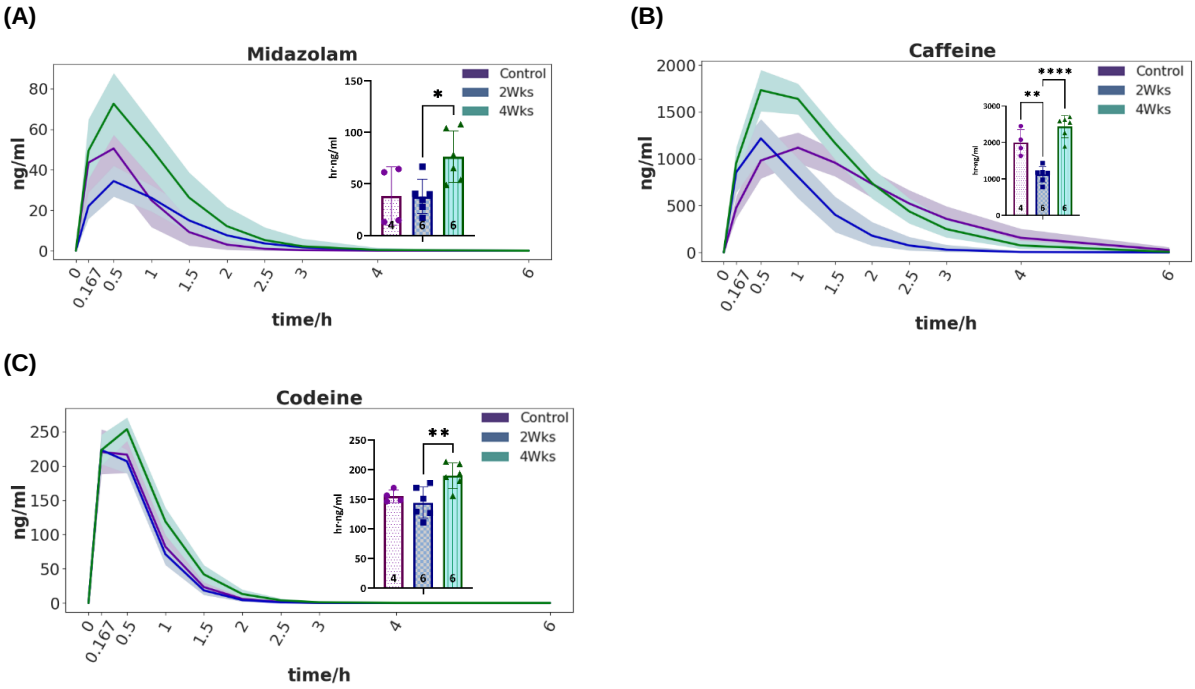

Figure 15. Drug clearance curves of the test drugs and their metabolites, as well as their corresponding AUC. Midazolam, caffeine, and codeine are represented in figures A, B, and C, respectively. *significance level < 0.05, **significance level < 0.01, *** significance level < 0.001, **** significance level < 0.0001. The sample size for each group is displayed at the bottom of the bar. The solid lines in the figures represent the mean, while the shaded areas correspond to the 95% credibility interval from the Bayesian analysis. “Reproduced with permission from Springer Nature” (Albadry et al. 2022).

Next, we analyzed the correlations between the severity of steatosis, irrespective of feeding time, and the corresponding AUC (see Figure 16 for the parent drugs and Figures S4, S5, and S6 in the Appendix for the metabolites). The severity of steatosis exhibited a moderately positive correlation with the AUC of midazolam and codeine, indicating a slower clearance of both test drugs (Figure 16, row A and row C). However, as expected based on the group analysis results (Figure 16, row B), we did not observe a correlation between the severity of the transiently occurring microvesicular steatosis and the AUC of all three test drugs.

The AUC of codeine and midazolam correlated with the steatosis pattern as well. Correlating the steatosis patterns with the AUC yielded similar results. As seen in Figure 16, rows C, the macrovesicular steatosis pattern had a moderate positive correlation with the AUC of midazolam and codeine, indicating a slower rate of midazolam and codeine clearance.

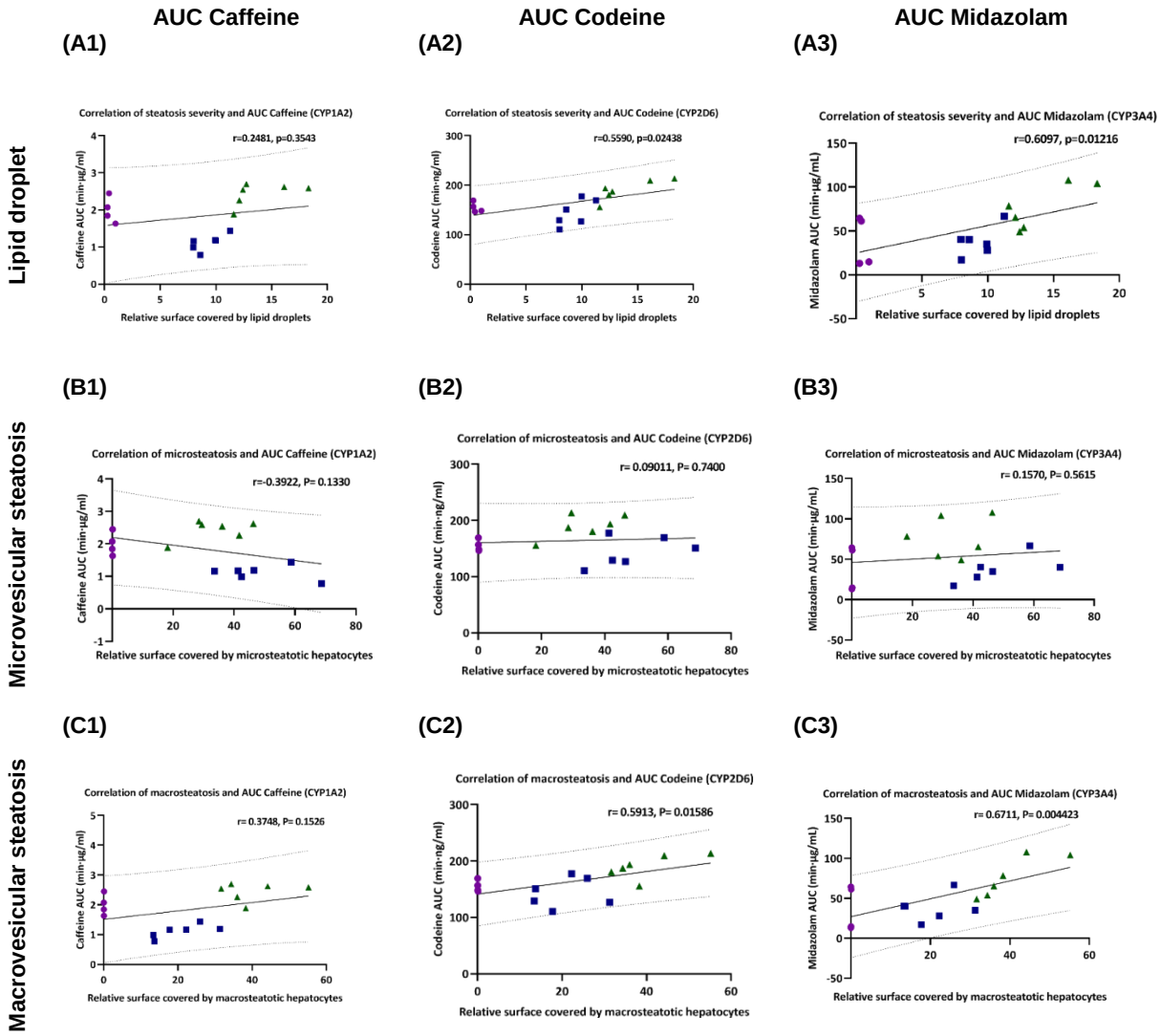

Figure 16. Correlation between the severity of steatosis and AUC (A-C). **(Row A)** The severity of steatosis is assessed by lipid droplet analysis of the relative percentage of the surface. **(Row B)** The extent of microvesicular steatosis is expressed in the relative percentage of the surface. **(Row C)** The extent of macrovesicular steatosis is expressed in percent. **(Column 1)** Correlation of steatosis type and severity with AUC of Midazolam. **(Column 2)** Correlation of steatosis type and severity with AUC of caffeine. **(Column 3)** Correlation of steatosis type and severity with AUC of codeine. Magenta color circles indicate the control group, blue color squares represent the two weeks HF-diet group, and green color triangles show the four weeks HF-diet group. “Reproduced with permission from Springer Nature” (Albadry et al. 2022).

4.1.5. Summary of correlation analysis

We conducted a comprehensive matrix correlation analysis, briefly summarizing the main findings and relationships identified (Figure 17).

To summarize,

(a) The variables related to steatosis, such as lipid droplets, microvesicular steatosis, macrovesicular steatosis, and triglyceride levels, exhibited a highly significant positive correlation with each other.

(b) The zonal expression of CYP3A4 and CYP1A2 did not show any significant correlation with steatosis variables, whereas CYP2E1 showed a slightly positive correlation.

(c) Steatosis parameters and protein content exhibited a significant negative correlation.

(d) Steatosis parameters displayed a negative correlation with CYP activity, as measured by EROD (CYP1A) and EMND (CYP3A), while PNHP (CYP2E1) showed a strong positive correlation.

(e) The AUC of midazolam and codeine positively correlated with lipid droplets and macrosteatosis.

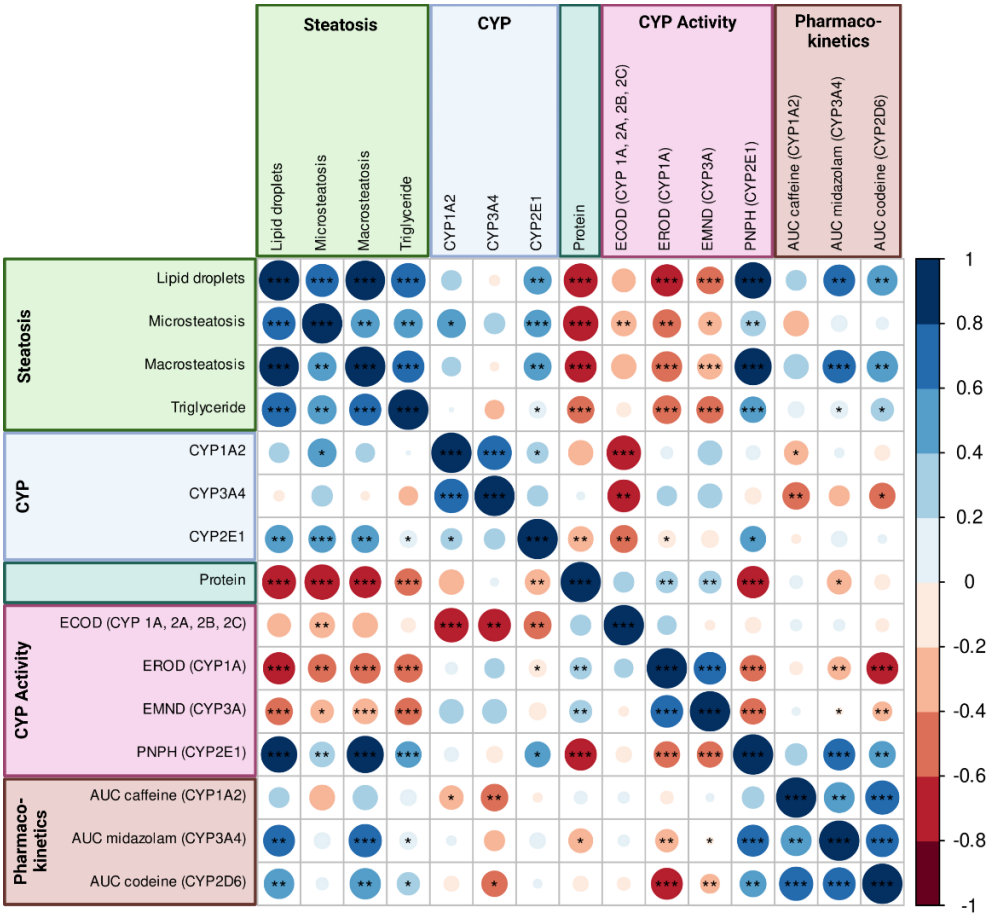

Figure 17. Correlation matrix based on Pearson correlation. Positive correlations are in blue, while negative ones are in red. The size of the circles corresponds to the strength of the correlation coefficient. Significance levels are *0.05, **0.01, and ***0.001, with p-values adjusted for multiple testing using Benjamini & Hochberg. Features have been sorted by category. “Reproduced with permission from Springer Nature” (Albadry et al. 2022).

4.2. Cross-species variability in liver lobular geometry and CYP zonation

When evaluating drug metabolism in various species, three important characteristics must be considered: lobular geometry, spatial distribution, and zonation of CYP enzymes. Lobular geometry in four species (mouse, rat, pig, and human) was quantified using HE-stained liver tissue sections. The five enzymes (GS, CYP1A2, 2D6, 2E1, and CYP3A4) were subsequently visualized in the four species. We systematically analyzed these features within the liver lobule, employing two distinct approaches.

Initially, the WSIs underwent classical analysis, which included a qualitative assessment of lobular geometry and staining patterns. Subsequently, a statistical comparison was conducted to determine the relative surface area occupied by the target protein. However, this method is not suitable for quantifying zonation patterns.

In the second step, we established an automated image analysis approach to determine and compare lobular geometry in all four species. This approach was followed by quantifying CYP zonation and calculating the minimal number of lobules needed for the reliable assessment of a given target protein.

4.2.1. Classical descriptive approach for identifying species-specific differences in lobular geometry and spatial expression of CYP enzymes

Comparing the lobular geometry across different species has always posed a challenge owing to their subtle differences. On the contrary, it is relatively more straightforward to describe the extent of zonal expression, which varies among target proteins within a given species and for the same protein across different species, as illustrated in Figure 18.

Regarding lobular geometry, the most striking difference between various species is the presence of interlobular septa in pigs. In porcine liver lobules, septa encircle the hepatic lobule, allowing for convenient identification of the lobule. The portal fields are interconnected by the septa, resulting in an appearance analogous to bridging fibrosis in other species. Even the portal fields of terminal vessels in pigs contain a substantial amount of connective tissue.

Assessing lobular geometry is difficult in the other three species because of the absence of well-defined boundaries. The radial structure of the sinusoids can aid in identifying lobular boundaries. However, measuring lobular architecture through quantitative morphometric analysis presents a challenge. Mice and rats resemble each other to a great extent, and even experienced pathologists find it challenging to differentiate between their livers by using morphological criteria. In contrast to pigs, the portal area of the terminal vessels lacks extracellular connective tissue and contains few histiocytes. While human and porcine livers have visible arteries, those in rodent livers are poorly visualized. As a result, human lobular geometry appears to be more similar to

that of rodents than to that of pigs. Nevertheless, hepatic arteries are easily visible due to the distinct appearance of the tunica media of the vascular wall.

Qualitative and quantitative evaluation of CYP expression confirmed that all CYP enzymes are expressed to varying degrees in the pericentral zone of the hepatic lobules in all four species (Figure 18 and Appendix Tables S 6 and S 7)

The zonal expression of GS in humans, pigs, rats, and mice follows a comparable pattern (Figure 18, row B). GS is expressed in two to three lines of pericentral hepatocytes. A quantitative analysis of the relative surface area showed that the relative coverage of lobules ranged from 5 to 13%. The species difference between mice and pigs was nearly two times greater. No statistically significant difference was observed in the relative coverage of GS-stained hepatocytes across all species compared to human tissue.

The zonal expression of CYP1A2 is likewise remarkably similar in humans and mice, with a strong pericentral signal that extends from zone 3 into zone 2 (Figure 18, row C). In the rat, the signal was primarily restricted to the pericentral three to four lines of hepatocytes in zone 3 and was less intense. Pigs did not exhibit zone-specific expression of the enzyme; instead, it was distributed throughout the lobule. A quantitative examination of the percentage area covered by CYP1A2 in humans and mice revealed a similar zonated expression pattern, covering the hepatic lobule by around 55.1 ± 11.9% and 60 ± 5.1%, respectively. Pigs had a far higher amount of expression, covering around 81.76 ± 7.7% of the lobular surface, while rats had a significantly lower extent of expression, covering only 32.5 ± 5.5% of the lobular surface.

The zonal expression of CYP2D6 followed a panlobular pattern across all four species, with homogeneous expression in humans and pigs. (Figure 18, row D). The expression pattern in rats was rather heterogenous. In contrast, we observed a stable expression pattern in mouse livers with a strong signal in the first pericentral line of hepatocytes and relatively weaker signals in the remaining zones. A quantitative examination of the relative lobular area covered by CYP2D6 revealed similar levels of zonal spatial expression. For more information, see Appendix Tables S 6 and S 7.

The zonal expression of CYP2E1 exhibited a consistent pattern and spatial distribution across the four species (Figure 18, row E). Specifically, a prominent pericentral signal extended from zone 3 to zone 2. The quantitative examination of the relative area covered by CYP2E1 positive hepatocytes in the liver showed coverage rates of 61.3% ± 7.2%, 65.4% ± 7%, and 56 ± 8.4% in mice, rats, and pigs, respectively. In humans, it was approximately 72.2% ± 9.4%.

CYP3A4 zonal expression was similar in humans and mice, with a moderate to strong pericentral signal limited to zone 3 and extending into zone 2 (Figure 18, row F). On the contrary, the rat liver

exhibited a strong signal limited to the first line of pericentral hepatocytes, with a moderate to weak signal extending into the second zone of the liver. CYP3A4 was shown to be distributed throughout the lobule in pigs, spanning all three hepatic zones. A consistent pattern was seen in the quantitative study of CYP3A4 across humans, rats, and mice, covering roughly 50% of the lobular surface. The inter-individual heterogeneity in the extent of zonal expression and distribution of CYP3A4 was larger in rat liver tissues. Conversely, in the porcine liver, CYP3A4-positive hepatocytes occupied roughly 90.6 ± 2% of the lobular surface.

In conclusion, mice are the ideal choice for pre-clinical experimental drug metabolism research unless larger species are needed, such as in studies looking into the impact of intricate hepatobiliary surgery on drug metabolism. This conclusion is based on the observed similarities between humans and animals. The CYPs should be chosen according to the species under investigation, with CYP2E1 being the preferred choice for cross-species studies in mice, rats, pigs, and humans. When conducting a comparative analysis between rodents (mice and rats) and humans, CYP1A2 can be selected. In addition, CYP3A4 is also relevant if the investigation is restricted to mice and humans.

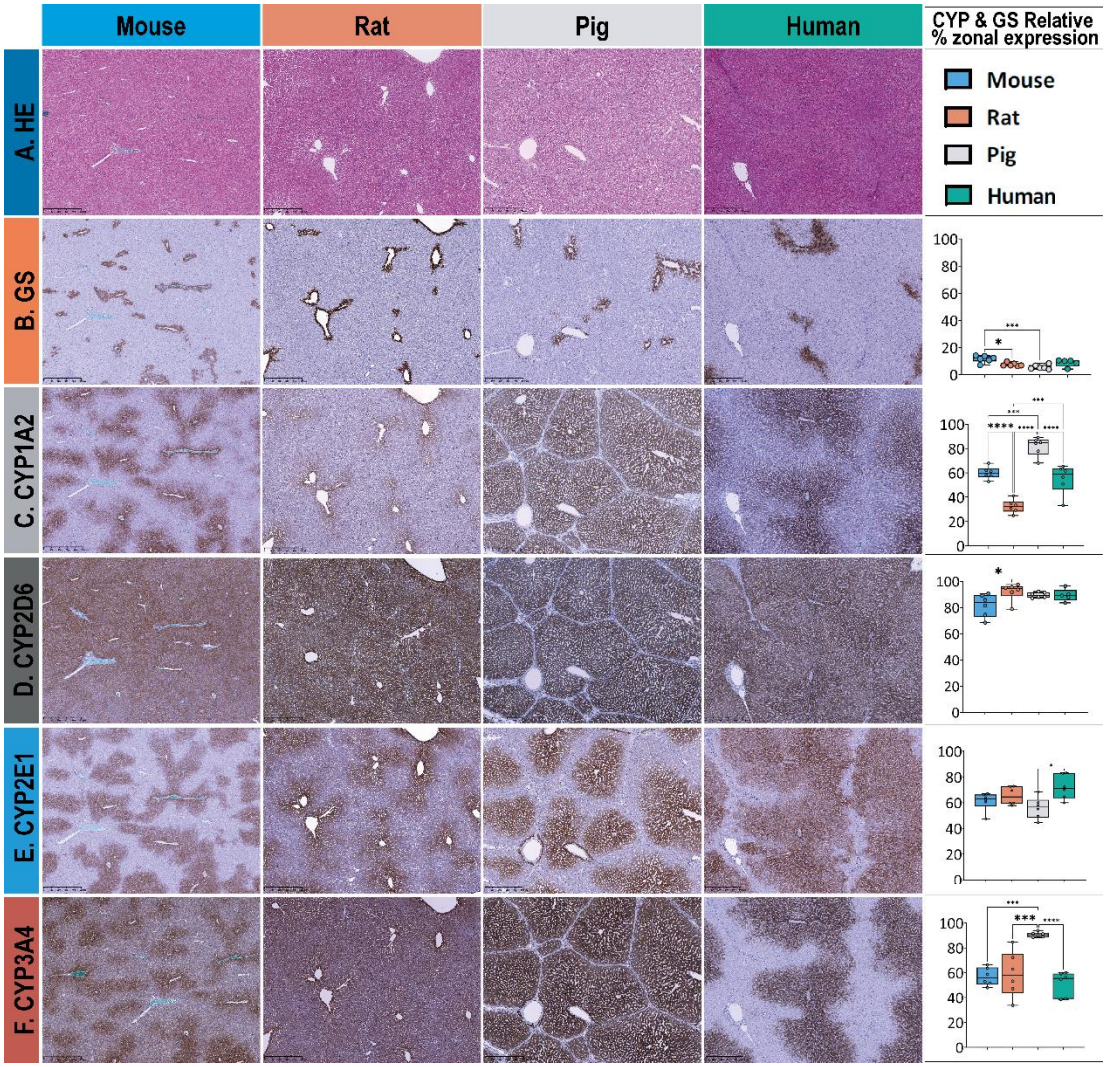

Figure 18. Overview of HE and extent of zonal expression as indicated by the relative surface covered by GS and CYP in liver tissue in mice, rats, pigs, and humans. The different stainings are depicted in rows, with columns 1-4 corresponding to the different species and column 5 presenting the results of the statistical analysis. (A) HE staining of normal liver tissue was used to depict lobular morphology in all species. The lobular structure appears similar except for the pig liver, where the lobules are separated by interlobular collagenous septae. (B) Glutamine synthetase (GS) staining is used to identify pericentral hepatocytes surrounding the central vein and to distinguish periportal from pericentral zones. Zonated expression is relatively similar across species, except for mouse and pig liver tissue, which show a significantly different distribution. (C) CYP1A2 staining shows a similar pericentral spatial distribution and zonated expression in mice and humans while demonstrating a significantly different zonated expression pattern in rats (pericentral) and pigs (panlobular). (D) CYP2D6 exhibits almost panlobular and similar distribution across four species. (E) CYP2E1 is observed in the pericentral region in all four species, with no substantial difference. (F) CYP3A4 shows almost identical pericentral to midzonal expression patterns in mice and humans but panlobular in both rats and pigs. Scale bars 500 µm. Colors represent different species, with blue for mice, orange for rats, gray for pigs, and green for humans. Significance levels according to descriptive one-way ANOVA: * Significance level < 0.05, ** Significance level < 0.01, *** Significance level < 0.001, **** Significance level < 0.0001 (One-way-ANOVA) . “Reproduced from Frontiers in Pharmacology” (Albadry et al. 2024).

4.2.2. Image analysis pipeline for determination of lobular geometry, quantification, and analysis of zonation patterns

An image analysis pipeline was established using WSI of stained liver sections to quantitatively assess lobular geometry and zonation patterns of proteins (Figure 19; additional details provided in the Method section). The pipeline comprises the subsequent steps:

(a) ROI detection in the WSI field enables tissue section identification.
(b) Registration of adjacent WSI ROIs applying Valis (Gatenbee et al. 2023) enables the generation of multiplexed protein WSIs for subsequent analysis.
(c) Color channel separation in the immunostained whole slide image enables color deconvolution-based access to the corresponding protein data.
(d) Lobular segmentation of WSIs yields positional information and lobule boundaries (portality).

Notably, the approach described in this study does not necessitate the manual annotation of central veins. Furthermore, it has been effectively utilized in examining lobular geometries and the quantification of proteins in WSI, encompassing single and multiple liver lobes, in various animal models, including mice, rats, pigs, and humans.

Using this image analysis approach, we systematically compared the lobular geometry and zonation patterns of key CYP450 enzymes across four species (Figure 20). Lobular geometry was quantified by measuring the lobular perimeter, area, compactness, and minimum bounding radius. Subsequently, a statistical analysis was performed to examine the variations among the different species. The zonal gradient intensity and expression of GS and the four CYPs (CYP1A2, 2D6, 2E1, and CYP3A4) were analyzed to ascertain the variations in zonation patterns in mice, rats, pigs, and humans.

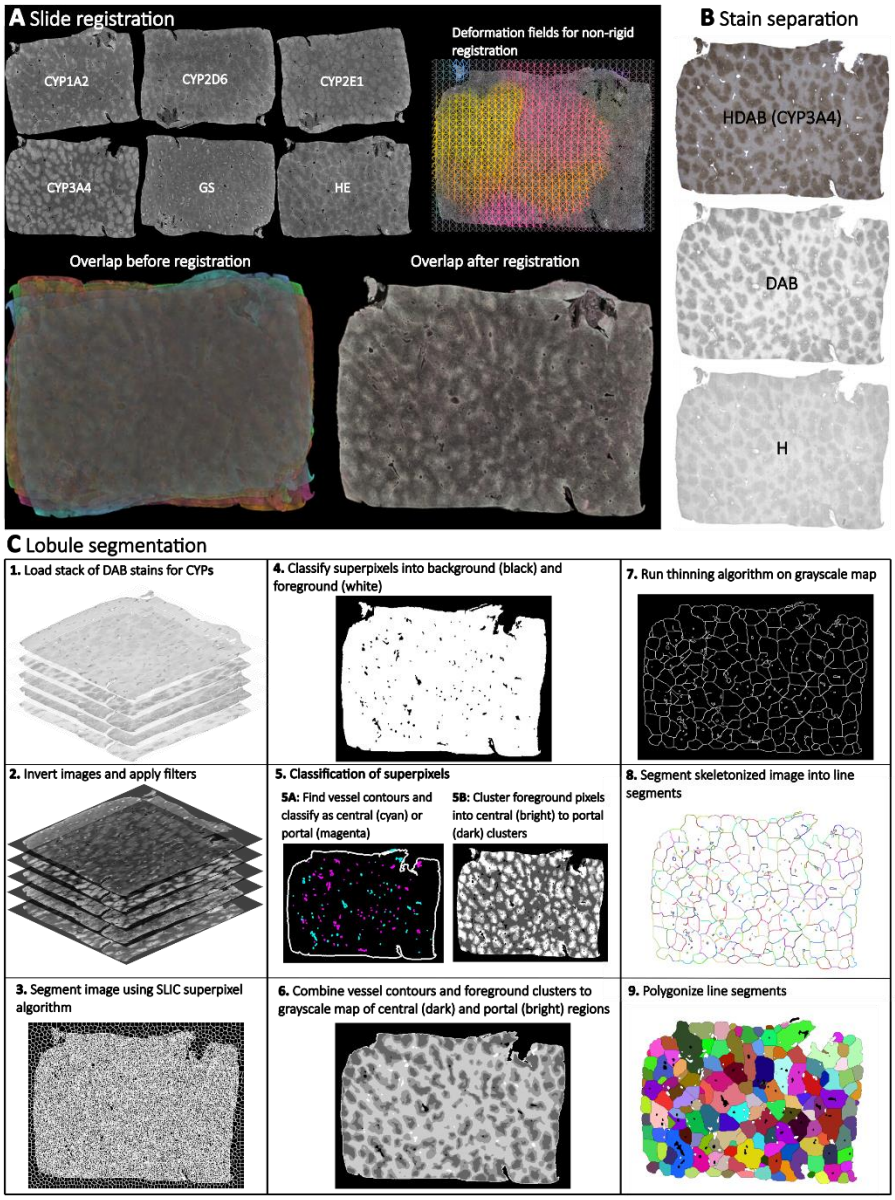

Figure 19. Overview of the image analysis pipeline for quantifying lobular geometry and CYP zonation patterns. The pipeline consists of three main steps: (A) Registration of HE, GS, and CYP WSI using Valis, allowing multiplexed WSIs to be generated. (B) Color channel separation in the WSI. HE WSIs are separated into blue (hematoxylin) and pink (eosin), and IHC WSIs are separated into blue (hematoxylin) and brown (DAB) using color deconvolution. (C) Lobular segmentation of WSIs consists of several steps: 1. Load a stack of DAB stains for CYPs and GS. 2. Perform black and white image inversion and filter application. 3. Perform Image segmentation using SLIC (Simple Linear Iterative Clustering) superpixel algorithm to generate uniform size and regular contour superpixels. 4. Classify superpixels into background (black color) and foreground (white color). 5. Classify the superpixels: 5. A. Find vessel contours and classify vessels as central (cyan) and portal (magenta), 5.B. Cluster foreground pixels, intro central (bright) to portal (dark) clusters. 6. Combine vessel contours and foreground clusters to create a grayscale map of central (dark) and portal (light) regions. 7. Apply a thinning algorithm to the grayscale map to create a skeleton. 8. Segment the skeletonized image into line segments. 9. Polygonize the line segments to create closed polygons. Reproduced from Frontiers in Pharmacology" (Albadry et al. 2024).

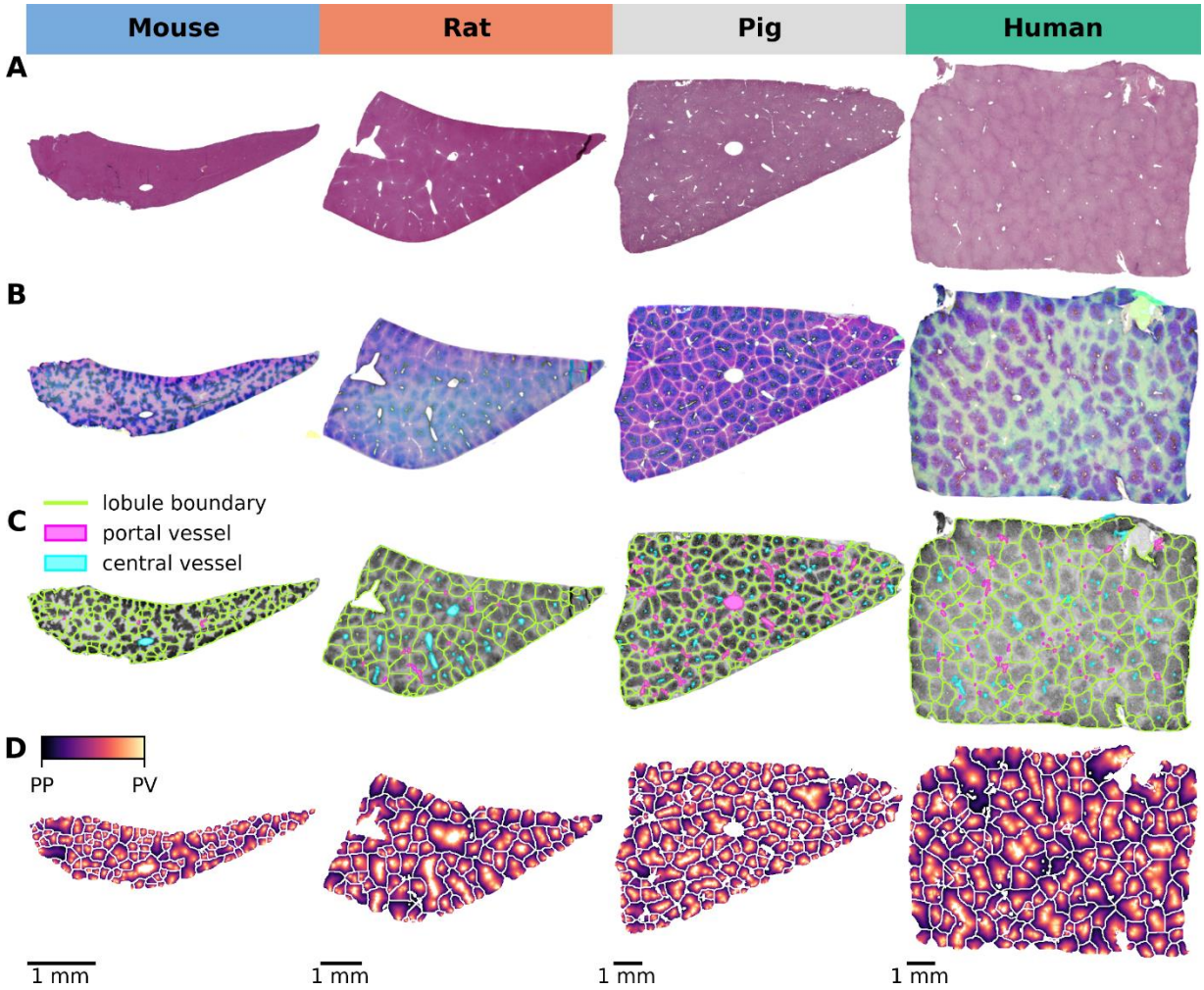

Figure 20. Lobular detection and position calculation. (A) HE staining of normal liver tissue from all four species showing lobular architecture. (B) Image normalization and stain separation to ensure optimal comparisons across species. (C) Detection of lobular regions providing a clear visual representation of lobular boundaries, distribution of lobules, central vessel, and portal vessels on CYP2E1 staining. (D) Mapping of the central-portal distance on each lobule, allowing a quantitative analysis of the spatial arrangement of the lobules. “Reproduced from Frontiers in Pharmacology” (Albadry et al. 2024).

4.2.2.1. Species-specific lobular geometry

Four main measurements were used to determine the species-specific lobular geometry of the segmented lobule. These were the perimeter, the area, the compactness, and the minimum bounding radius. The perimeter is calculated as the circumferential length of the outer edge of the lobule. The area represents the surface area of the lobule. The compactness is calculated as the ratio of the area of the lobule polygon to the area of a circle with an identical perimeter. The minimum bounding radius is calculated as the radius of the minimum bounding circle enclosing the lobule. The geometric parameters obtained for the various species and the correlation between them are illustrated in Figure 21. The corresponding numerical values are in the Appendix, Tables S 8 - 10.

Geometric parameters were determined for segmented lobules in mice, rats, pigs, and humans, with 1530, 669, 698, and 1074 lobules examined, respectively. The findings suggest that lobule size increases proportionally with species size, with larger species having larger lobules. The smallest lobule radius and perimeter were measured in mice, whereas human lobules were twice as large. In detail, the murine lobular boundary radius had a mean value of 375 ± 216 µm, whereas the mean bounding radius for human lobules was 637 ± 473 µm.

Similarly, the mean perimeter of liver lobules was found to increase with species size, with mice having a mean perimeter of 2233 ± 1397 µm and humans having a mean perimeter of 3966 ± 3200 µm. The minimum bounding radius of the lobules, a measure of their size, also nearly doubled from 375 ± 216 µm in mice to 637 ± 473 µm in humans. As expected, the area of the lobules increased significantly from 299281 ± 36009 µm² in mice, 467614 ± 729369 µm² in rats, 718451 ± 57536 µm² in pigs, to 966234 ± 1357480 µm² in humans, representing a four-fold increase across species.

Conversely, the compactness of the lobules, a measure of their roundness, decreased slightly with increasing species size. Mice had the highest compactness (0.64 ± 0.10), followed by rats (0.62 ± 0.11), pigs (0.61 ± 0.10), and humans (0.59 ± 0.12). The results of this study indicate that as the size of the species increases, the lobes exhibit an increase in size and a decrease in roundness.

The statistical comparison of medians revealed significant differences in lobular size, while compactness varied little between species. All species exhibited a similar level of individual variability in geometric parameters, with humans displaying slightly more significant variability than the other species. A high degree of consistency was observed in the geometric parameters of different subjects. Sections from four liver lobes were available for mice and were also compared. However, geometric parameters for the different lobes were comparable, and no differences were

detected between the left lateral lobe (LLL), median lobe (ML), right lobe (RL), and caudate lobe (CL). In other words, neither intra-lobe variability in mice nor intra-subject variability in mice, rats, pigs, and humans were observed in the geometric parameters, but significant differences were observed between species.

Nevertheless, high interlobular variability in geometric parameters was observed, possibly due to variations in the lobular position, size, and 3D shape relative to the 2D sectioning plane, as evidenced by the large standard deviations and interquartile ranges in all four species.

The correlation structure for the various geometric parameters was highly consistent across species, as depicted in Figure 21B. In particular, area and perimeter exhibited a strong positive correlation ($r=0.99$) across all species, indicating that hepatic lobules with a larger area also have a larger perimeter. Conversely, compactness was observed to have a weak to moderate negative correlation with perimeter (r in $[-0.54, -0.63]$) and area (r in $[-0.44, -0.55]$), implying that larger lobules are less compact and may appear ovaloid due to variable sectioning angles.

The similarities in the median and range of the geometric parameters across species (Figure 21A) and the comparable correlation structure between species in the geometric parameters (Figure 4B) suggest that the internal, complex 3D structure of the hepatic lobule may be rather similar. As such, lobular geometry is a robust feature with low inter-individual and interspecies variability but high variability between different lobules.

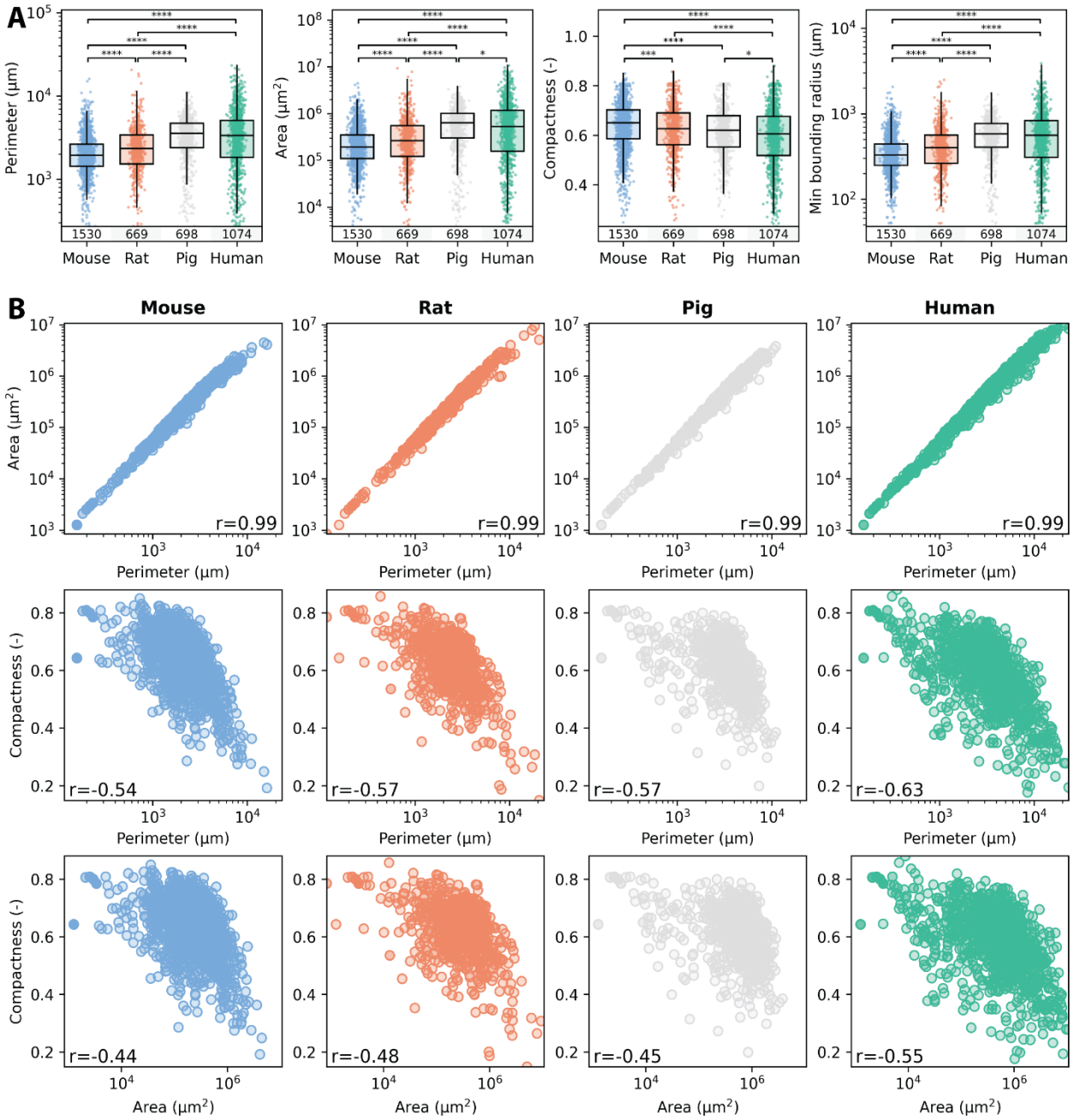

Figure 21. Comparison of lobular geometry in the four different species. (A) Quantification of species-specific lobular geometry. For all species, the lobular perimeter, area, compactness, and minimum bounding radius were calculated for all lobuli per section. Box blots and point clouds of these parameters are depicted. Boxes represent quartiles Q1 and Q3. The upper whisker and lower whisker extend to the last datum less than Q3 + 1.5 * IQR and the first datum greater than Q1 - 1.5 * IQR, respectively. IQR denotes interquartile range (Q3-Q1). Significance levels: * p<0.05, ** p<0.01, *** p<0.001, **** p<0.0001. (B) Correlation between the geometric parameters was assessed using the Spearman rank correlation coefficient. Colors represent different species, with blue for mice, orange for rats, gray for pigs, and green for humans. “Reproduced from Frontiers in Pharmacology” (Albadry et al. 2024).

4.2.2.2. Quantification of zonated expression from whole slide images: Gradient intensities and zonation patterns

In the subsequent analysis, the zonated expression of CYP enzymes along the portal-venous axis was assessed in all liver lobules of the four species (Figure 22). We identified the position-dependent protein expression based on the computed positions within the segmented lobules. In particular, we assigned each pixel in a lobule, from periportal (0) to perivenous (1), according to its proximity to the closest periportal or perivenous area. Using these positions, we identified the GS and CYP protein zonation patterns across lobules and species. Examining the collective zonal expression of all markers unveiled unique patterns corresponding to the various species and proteins.

HE staining appeared consistent and flat across all species. This result was expected as HE staining is used to delineate the morphological structure of the hepatic lobule. There are no anticipated zonation differences in HE staining.

GS exhibited similar gradient and zonal distribution patterns in the four species studied along the portal-venous axis. The superimposed plots of normalized staining intensity showed that GS was predominantly localized in zone 3, encompassing the 2-3 lines of pericentral hepatocytes. No periportal distribution pattern was observed in any of the four species.

CYP1A2 displayed relatively similar gradient and zonation patterns in mice, rats, and humans. It was mainly localized in zone 3 and extended into zone 2 within the adjacent 5-6 rows of pericentral hepatocytes. However, in pigs, the gradient distribution of normalized intensity was mainly observed in zones 3 and 2 and extended into zone 1 of the periportal hepatocytes.

CYP2D6 presented a uniform and constant zonal distribution pattern across the four species studied. It exhibited a panlobular distribution within the liver lobules along the portal-venous axis. Of all the CYP enzymes analyzed, CYP2D6 was the only one that did not show a clear zonation pattern and had higher protein content in the perivenous region than in the periportal region.

CYP2E1 revealed a linear gradient distribution of normalized intensity throughout the liver lobules of different species. It was mainly observed in zones 3 and 2. In rats, there was a higher intensity in zone 1, with a flatter gradient than in the other species.

The gradient intensity of CYP3A4 was comparable between humans and mice, particularly in zone 3 and extending to zone 2. Rats and pigs, on the other hand, showed a gradient distribution across the liver lobules that was similar to but distinct from that of mice and humans. The normalized intensity of CYP3A4 was higher in zones 3 and 2, and it extended to periportal hepatocytes in zone 1. Humans were shown to have the strongest periportal to perivenous gradient.

This automated image analysis approach to quantify zonation enables quantitative comparative analysis of zonation patterns of multiple target proteins (like the four different CYP proteins) in a single species and between different species. The overlaid curves reveal the zonated expression patterns in humans and mice to be quite similar, while those in rats and pigs are more dissimilar.

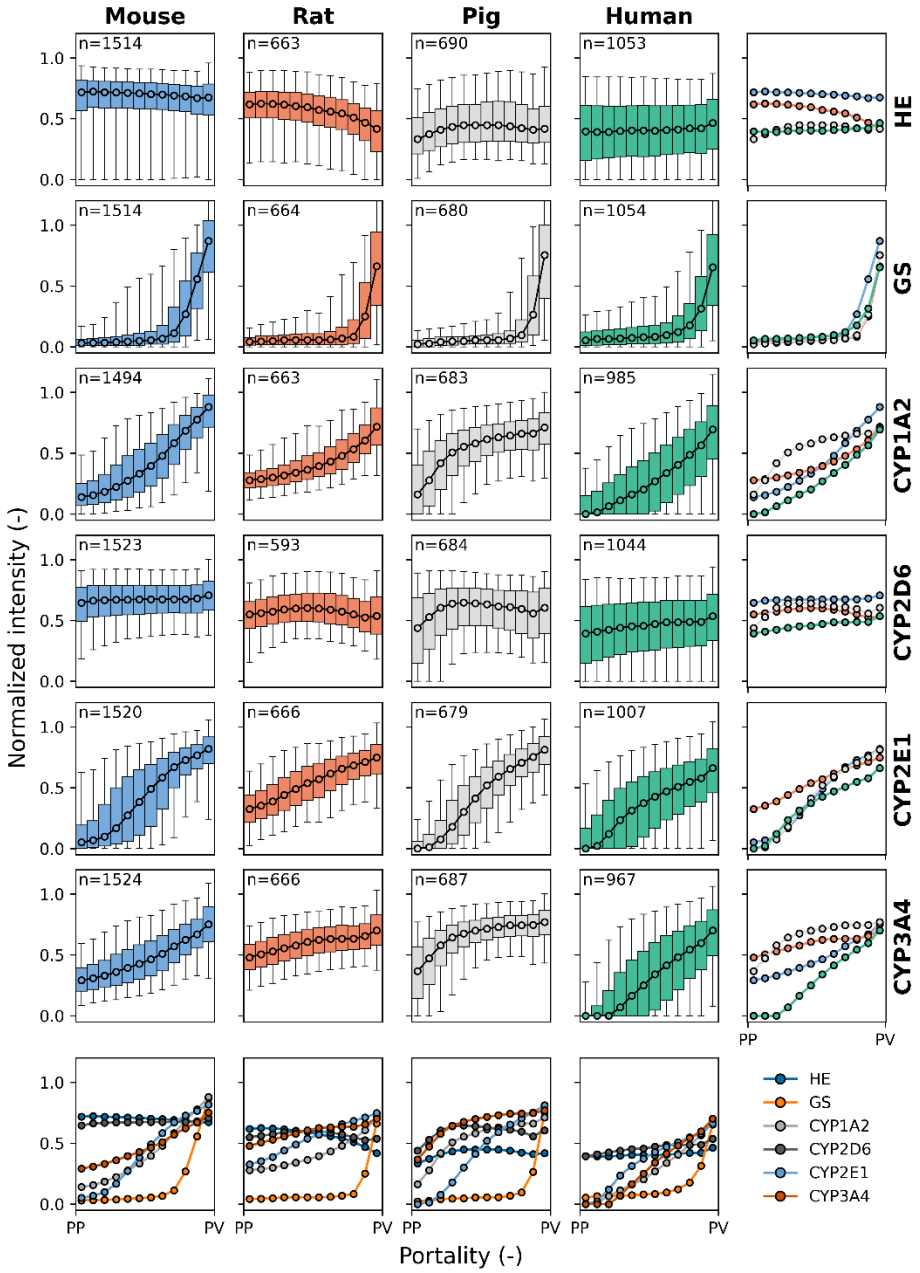

Figure 22. Species comparison of protein zonation. Zonation patterns of HE, GS, CYP1A2, CYP2D6, CYP2E1, and CYP3A4 in mouse (blue), rat (orange), pig (gray), and human (green). Normalized staining intensity (per slide) is plotted against portality (relative position between periportal (PP) and perivenous (PV) zones in each lobule). Data were binned in 12 bins from PP to PV. Median values are shown for all lobuli of all individuals. Box plots correspond to the median, interquartile range with whiskers at 5%, 95% percentile. Colors represent different species: blue for mice, orange for rats, gray for pigs, and green for humans. n: number of lobuli for the respective analysis. “Reproduced from Frontiers in Pharmacology” (Albadry et al. 2024).

4.2.2.3. Number of lobules required to determine geometric parameters and relative expression

Subsequently, we calculated the number of lobules needed for a representative evaluation of geometric characteristics, zonation patterns, and relative expression (Figure 23).

We first calculated the number of lobules required to calculate mean geometric parameters with a 95% confidence at a specified margin of error (Figure 23A, data in Appendix Tables S 9 - 11). For instance, in mice, rats, pigs, and humans, the minimum number of liver lobules needed to compute compactness with a 95% confidence level and a 20% margin of error is 2.2 ± 1.1, 2.7 ± 1.5, 2.4 ± 0.8 and 3.8 ± 2.9, respectively.

Key findings of the analysis indicate that:

(a) A larger margin of error results in fewer lobules being required for analysis. The relationship between the number of lobules required and the margin of error is highly non-linear, meaning that a minor relaxation of the potential margin of error necessitates far fewer lobules.

(b) The accurate determination of human geometric parameters requires a higher number of lobules than needed for mice. The number of lobules required for pigs and rats is intermediate to those required for humans and mice.

(c) Different geometric parameters require different numbers of lobules for accurate evaluation. For instance, the area requires more lobules than the perimeter and minimum boundary radius, while compactness requires the fewest for precise quantification.

(d) There is a significant amount of variability between biopsies of the same species. This variability raises the possibility of some intrahepatic variability in geometric parameters, leading to marginally differing lobule counts needed for a given level of targetting accuracy in a given biopsy.

We then calculated the number of lobules necessary to calculate zonation patterns with 95% confidence and a 20% margin of error (Figure 23B). The number of lobules necessary for the zonation pattern varied depending on the protein of interest and the species.

In some instances, less than 25 lobules were sufficient to calculate mean expression levels for several positions and proteins in a given zone. For the investigation of GS and CYP2E1 in mice, however, the required number of lobules increased to 150 and 100, respectively. Similarly, 120 lobules were needed to quantify human periportal protein levels for CYP3A4. An essential factor in determining the number of lobules required was the coefficient of variance of the intensity at the given position. A high variability in protein expression at a specific location resulted in more lobules needed to determine the mean intensity. Although the protein pattern in a liver lobule is similar for

most proteins, the degree of interlobular and interindividual variability differs among the four species.

Moreover, the number of lobules was determined to ascertain the normalized expression of proteins within a lobule with a 95% confidence level and 20% error (Figure 23C, data in Appendix Table S 11). The number of lobules required for GS staining was almost the same across different species, with up to 42 in humans. When determining the normalized expression of different CYP proteins in mice and rats, the required number of lobules was relatively similar and fewer than in other species, with a maximum of 35 lobules for CYP1A2, 17 for CYP2D6, 27 for CYP2E1, and 31 for CYP3A4 in humans.

A significant finding is that determining the normalized expression of a protein in a lobule requires significantly fewer lobules than determining the lobular pattern. Regarding determining normalized protein expression, the highest number of lobules was required for human liver tissue, followed by pig, rat, and mouse liver tissue.

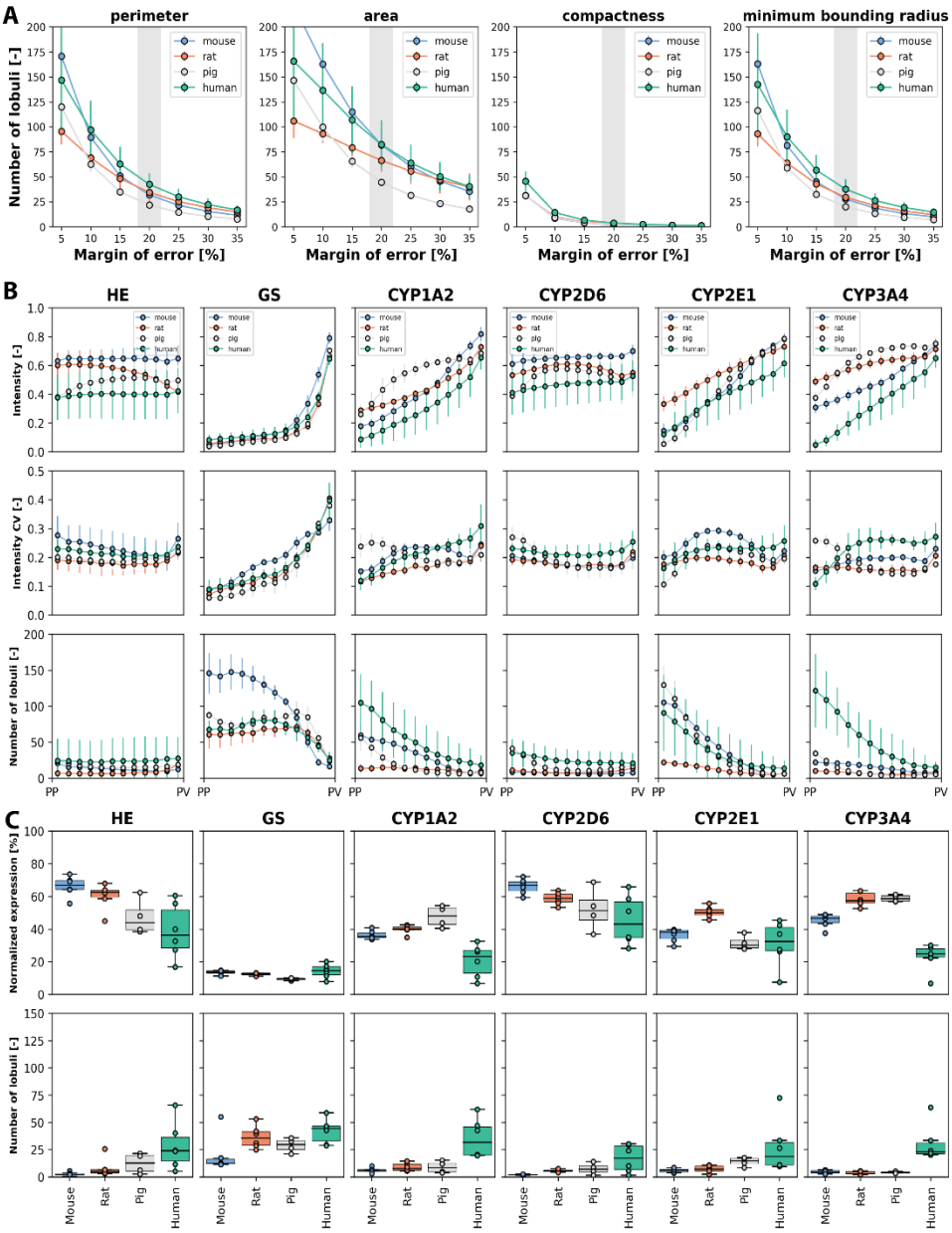

Figure 23. Number of lobules required to determine geometric parameters, zonation patterns, and relative expression. Species are color-coded as mouse (blue), rat (orange), pig (gray), and human (green). (A) Number of required lobules to determine the geometric parameters area, perimeter, compactness, and minimum boundary radius for a given margin of error (5% to 35%) and a confidence level of 95%. Data expressed as mean ± SD for the subjects. (B) Number of required lobules to determine the protein zonation pattern, i.e., the normalized intensity for the 12 bins with a confidence level of 95% and a margin of error of 20%. Depicted are the normalized intensity mean ± SD for the subjects (top), the coefficient of variation of the normalized intensity as mean ± SD for the subjects (middle), and the required number of lobules for estimation of the zonation pattern as mean ± SD for the subjects (bottom). (C) Number of required lobules to determine the relative protein expression per lobule with a confidence level of 95% and a margin of error of 20%. Relative expression as mean values for individual subjects (averaged over all lobuli per subject) and the corresponding boxplot of the means (top). Number of lobules required for individual subjects and the corresponding boxplot (bottom). “Reproduced from Frontiers in Pharmacology” (Albadry et al. 2024).

5. Discussion and perspectives

5.1. Summary of findings and perspectives

In this thesis, we obtained two seemingly unrelated key results.

In experiment A, we investigated the impact of zonated steatosis patterns on specific zonated features of drug metabolism in a mouse model. As described above, periportal steatosis did affect certain distinct features of the pericentrally located drug metabolism, a phenomenon named portalization. Here, mainly the activity of CYP1A and CYP3A was reduced, and CYP2E1 activity was induced, whereas clearance of midazolam and caffeine reflecting the activity of CYP1A2 respectively, CYP3A4 was delayed. As a next step, we want to investigate the translational relevance of these findings to human liver function and disease. Therefore, we plan an observational clinical study to study this phenomenon in depth.

In experiment B, we performed a detailed comparison regarding the spatial expression of key drug metabolizing enzymes using a newly established image analysis pipeline. Using this pipeline, we observed the increasing similarity in lobular geometry and CYP expression between pigs, rat, mice, and humans. However, it is crucial to understand that the results obtained in controlled laboratory conditions may only partially reflect the complexity of the human liver. To ensure that the findings are applicable to clinical translation, we want to conduct further cross-species studies, taking into account species-specific features of drug metabolism and comparing them to human counterparts.

5.1.1. Periportal steatosis affected specific parameters of pericentrally zonated drug-metabolizing enzymes

Experiment A resulted in four main findings:

(1) A high-fat diet low in methionine and choline resulted in periportal steatosis distributed heterogeneously throughout the liver.
(2) The severity and pattern of periportal steatosis did not correlate with the zonated expression of the different CYP proteins as visualized by IHC.
(3) The degree and pattern of periportal fat accumulation were correlated with the alterations in the *ex-vivo* activity of CYP1A, CYP2E1, and CYP3A.
(4) The severity and pattern of fat accumulation in the periportal hepatocytes correlated with alteration in the in-vivo pharmacokinetics of caffeine and midazolam but not codeine.

To investigate the impact of a clearly defined zonated distribution of steatosis on pericentrally located processes, we selected a dietary model of periportal steatosis. Our primary objective was to investigate the effect of this periportal pathology on drug metabolism, which is one of the key

metabolic processes taking place in the pericentral zone. Based on previous experiences with the rats, we used a high-fat diet with reduced methionine and choline content to induce periportal hepatic steatosis (Deng et al. 2014). After two weeks of feeding, the mice developed periportal, mainly microvesicular, steatosis. In contrast, after four weeks of feeding, the type of steatosis changed from mainly microvesicular to predominantly macrovesicular pattern.

Interestingly, the same diet also caused periportal, mainly macrovesicular steatosis, in rats within one week of feeding (Sun 2011;Deng et al. 2014). Extension to the midzonal region was seen within two weeks of feeding. Severe steatosis spanning from the periportal to the pericentral region was induced within four weeks of feeding.

Mice did react slower to this induction protocol, as expected based on a recent review by Zhong and co-workers (Zhong et al. 2020). They concluded that rats were more susceptible to a high-fat diet than mice, as indicated by a faster progression of the histological alterations.

Furthermore, the pattern of steatosis observed in mice showed specific differences compared to rats. Mice exhibit both macrovesicular and microvesicular steatosis. Microvesicular steatosis was more pronounced after two weeks of feeding than four weeks. This finding conforms to the pathogenesis of steatosis, that the accumulation of tiny lipid droplets in a few hepatocytes is involved in the development of steatosis (Satapathy et al. 2015;Gluchowski et al. 2017). The small droplets can coalesce into a single large vacuole, giving the hepatocyte the signet-ring appearance that characterizes macrovesicular steatosis. Hence, the development of macrovesicular steatosis takes more time and is rather the result of a more chronic process, whereas microvesicular steatosis represents an early stage of disease.

Microvesicular steatosis can result from several underlying causes. It may arise due to an acute or toxic insult to the liver (Miele et al. 2017), e.g., drug-induced liver injury (Fromenty 2019). Furthermore, it may manifest as a result of a mitochondrial disorder that impairs beta-oxidation of fatty acids (Silva et al. 2011), potentially impacting metabolic function.

The severity of hepatic steatosis has been assessed through four complementary approaches. We quantified hepatic TG levels biochemically. We determined the relative surface of fat-laden hepatocytes to differentiate between normal and steatotic livers. Lipid droplet analysis was employed to determine the more subtle differences between the type of steatosis resulting from two induction protocols for steatosis. This analysis is frequently used and involves the quantification of the white area of lipid droplets in relation to the remaining area (Marsman et al. 2004;Yersiz et al. 2013;Homeyer et al. 2015;Homeyer et al. 2018). However, the tiny droplets of microvesicular steatosis cannot be identified unambiguously, making an exact quantification difficult. To overcome this limitation, a pattern recognition algorithm has been trained to separately

quantify micro- and macrovesicular steatosis more precisely. This approach is similar to previous research in the field (Brunt 2007;Deng et al. 2014) and more comparable to clinical routine diagnosis. The clinical assessment of the severity of steatosis is based on estimating the relative percentage of hepatocytes with lipid droplets (Kleiner et al. 2005;Brunt 2007). However, pathologists must also report zonal distribution (periportal versus pericentral steatosis) and the steatosis pattern (macrovesicular versus microvesicular steatosis), albeit only qualitatively.

The present study has revealed three observations that provide insight into the influence of periportal steatosis on drug metabolism, deserving further verification. As mentioned, periportal steatosis did not influence the pericentral zonal expression pattern of the four essential CYP enzymes examined. However, the activity of CYP1A, CYP2E1, and CYP3A was found to be impacted by periportal steatosis. Additionally, the elimination of caffeine (CYP1A2) and midazolam (CYP3A4) was found to be decelerated by periportal steatosis, whereas that of codeine (CYP2D6) remained unchanged.

5.1.1.1. Influence of periportal steatosis on the zonal expression of CYP enzymes

The influence of steatosis patterns or zonal distribution on the level and distribution of CYP expression was rarely investigated. We characterized steatosis in terms of severity, type, and zonal distribution. Neither micro- nor macrovesicular periportal steatosis affected the spatial distribution of CYP enzyme expression. However, we saw distinct effects on CYP activity and drug clearance. It is plausible that even if zonation patterns remain unaffected, total mRNA and protein expression levels may be reduced in a severely steatotic liver. Additional spatial profiling techniques are required to elucidate this issue better.

Most currently available publications dealing with the impact of steatosis on drug metabolism studies do not report the type or zonal distribution of steatosis (as outlined in Appendix, Table S 2 and S 3). These studies focus on the reduced protein or mRNA expression level in steatotic livers from human patients (Fisher et al. 2009), rats (Stärkel et al. 2003;Zhang et al. 2019), and mice (Li et al. 2017), as demonstrated by western blot or qPCR (presented in Appendix, Table S 4). However, alterations in mRNA levels do not necessarily indicate corresponding changes in protein levels and are even less suitable as reliable indicators of protein activity. Various posttranscriptional, translational, and posttranslational regulatory mechanisms can influence protein expression and activity (Jamwal et al. 2017).

In conclusion, the regulation of CYP zonal expression levels, distribution, and activity in steatosis appears rather complex, as it may be related to the etiology or the animal model used. For instance, the upregulation of CYP2E1 in fatty liver disease is attributed to diverse mechanisms, as recently outlined in a comprehensive review by (Massart et al. 2022). Conversely, in alcoholic

liver disease, it was postulated that the heightened levels of CYP2E1 result from the inhibition of degradation by ethanol. However, the mechanism inducing an increased CYP2E1 expression in non-alcoholic fatty liver disease still needs to be elucidated. A vicious cycle has been proposed, commencing with elevated concentrations of fatty acids and insulin resistance that promote the expression of CYP2E1. The resulting increased protein levels of CYP2E1 may, in turn, elicit lipid peroxidation and oxidative damage and exacerbate insulin resistance, ultimately exacerbating liver fat accumulation.

Nevertheless, there are certain liver pathologies that affect the zonation and staining intensity of the CYP protein. This is evident when the vitality of pericentral hepatocytes is impacted, as often happens after intoxication. CCl4-induced toxic liver injury with pericentral necrosis results in a decrease in the expression and staining intensity of CYP proteins (Schenk et al. 2017). However, changes in CYP expression can also arise in the event of periportal morphological impairment. The study of Ghallab and co-workers (2019) is the best example of this, as they found a loss of CYP expression not only in the case of pericentral but also in the case of periportal fibrosis (Ghallab et al. 2019). Nonetheless, morphological damage is not always a prerequisite for an altered CYP expression. Despite normal morphology in a mouse model of chronic intermittent hypoxia mimicking sleep apnea, Zhang and colleagues (2018) observed selective loss of CYP1A mRNA and protein expression (Zhang et al. 2018).

The above observations indicate that certain cellular or molecular events in the periportal region may lead to a molecular response of cells in the pericentral areas. As previously mentioned, Ghallab proposed that in the case of periportal fibrosis, inflammatory mediators might stimulate the cellular response of hepatocytes located in the pericentral region, which is similar to what is observed in the case of pericentral fibrosis (Ghallab et al. 2019).

5.1.1.2. Influence of periportal steatosis on CYP activity

Periportal steatosis did affect the activity of certain CYP enzymes, but the expression pattern remained constant. In our study, we noticed a decrease in the activity of the CYP1A and CYP3A families in liver tissue as the severity of steatosis increased. In contrast, the activity of CYP2E1 increased with increasing steatosis severity. The observations above align with the conclusions found by other research groups, as outlined in a recent review (Cobbina and Akhlaghi 2017). Furthermore, as shown in Appendix (Table S 4), our literature work-up confirms these findings. Nevertheless, the aforementioned investigations primarily examined the global effects of steatosis without taking severity, patterns, or zonated distribution into consideration.

The downregulation of enzymes belonging to the CYP3A family was observed in cases of steatosis, regardless of the species involved. This effect was shown in both humans with NASH

(Kolwankar et al. 2007;Fisher et al. 2009;Woolsey et al. 2015) and mice that were fed a high-fat diet (Woolsey et al. 2015), as well as rats (Day 2006). Similarly, others found that the activity of CYP1A enzymes was reduced in humans (Fisher et al. 2009) and rats (Zhang et al. 2019) but not mice.

Limited research has been conducted on regulating CYP2E1 activity in relation to steatosis. Most studies focusing on CYP2E1 have primarily examined mRNA or protein expression. CYP2E1 activity seems to be correlated with the dietary regimen. Stärkel and colleagues compared two distinct dietary models and found that applying 5% orotic acid resulted in increased activity. However, the animals fed an MCD diet for 2-6 weeks exhibited decreased activity (Stärkel et al. 2003). In the latter case, the simultaneous and significant inflammation appeared to impact activities negatively.

In our study, we examined the correlation between the degree of micro- and macrovesicular steatosis and the activity of CYP enzymes. We found substantial differences between the two patterns in terms of CYP2E1 activity. Microvesicular steatosis did not impair CYP2E1 activity. On the contrary, a positive correlation was observed between macrovesicular steatosis and CYP2E1 activity. This observation differs from the findings reported by Stärkel, who observed a decrease in CYP2E1 expression in rats with macrovesicular steatosis induced by the MCD diet (Stärkel et al. 2003). Based on these findings, it becomes evident that the role of etiology, steatosis pattern, and concurrent inflammation needs additional investigation.

Nevertheless, the scope of these considerations is limited by the challenge of differentiating and assessing CYP enzyme activity that aligns with the expression of individual CYP isoforms. However, it is essential to closely monitor the zonal distribution of CYP isoform expression to elucidate the correlation with the severity of steatosis. Limited information is available regarding the potential cross-reactivity of the CYP isoform antibodies employed.

In contrast to the other four activity assays, one of them predominantly measures the activity of a single isoform, as demonstrated in Table 4. Specifically, the PNPH assay primarily evaluates the activity of a distinct isoform, the CYP 2E1. Conversely, the EROD assay assesses the activity of subfamily 1A and its major isoform 1A2, while the PROD assay is designed to assess the activity of the CYP2B family with key isoforms 2B6 and 2B1. In contrast, the EMND assay provides a more comprehensive assessment, covering subfamily CYP3A and its major isoforms 3A4, 3A1, and 3A2, as well as other isoenzymes such as Cyp3a11, 3a13, and 3a16 (Baillie and Rettie 2011). The ECOD assay is also broad in scope, as it measures the combined activity of isoforms 1A1, 1A2, 2A1, 2A6, 2B1, 2B6, 2C9, and 2C11.

Furthermore, the typically used test drug midazolam is metabolized by other CYP isoenzymes found in other subfamilies (Van Waterschoot et al. 2008). Therefore, it is challenging to clearly attribute the enzyme activities to the expression of each isoform and pertain to the severity of steatosis.

However, It should be noted that the zonal distribution pattern of CYP2E1 was unaffected by steatosis, while, the activity displayed a positive correlation to the severity of steatosis, with high significance ($p<0.001$) observed when comparing severely steatotic samples to controls. Additionally, the zonal distribution pattern of CYP1A2 was similar in all three groups, while the activity displayed a negative correlation to the severity of steatosis, with moderate significance observed when comparing severely steatotic samples to controls. It is important to note that we did not investigate the zonal protein expression levels of each isoform in mouse liver, as was done in the technically challenging study by (Tachikawa et al. 2018).

5.1.1.3. Influence of periportal steatosis on pharmacokinetic parameters

Additionally, we examined how the pattern and severity of steatosis affected the pharmacokinetics of three test drugs. We observed the pharmacokinetics of each test drug. It is challenging to compare our findings to those of other studies because the majority of them do not provide a detailed characterization of steatosis. However, there has been controversy regarding the effect of steatosis on drug metabolism in earlier research (Lickteig et al. 2007;Woolsey et al. 2015;Kulkarni et al. 2016;Li et al. 2017;Bang et al. 2019). This implies that a multitude of factors, in addition to the presence or absence of steatosis, may influence drug metabolism.

The smaller AUC suggests that microvesicular steatosis primarily accelerated the pharmacokinetics of caffeine. Nevertheless, this impact was temporary. After the animals exhibited a predominance of macrovesicular steatosis, the elimination rate returned to its normal state, as evidenced by the statistically significant increase in the AUC. In contrast, Li et al. (2017) observed a considerably greater AUC for caffeine in a model with more severe macrovesicular steatosis in ob/ob mice fed an MCD diet compared to the control group (Li et al. 2017). Based on these findings, the metabolism of caffeine, which is indicative of the activity of CYP1A2, is significantly influenced by the pattern of steatosis but with opposing effects.

However, the pharmacokinetics of midazolam and codeine were unaffected by microvesicular steatosis. In contrast, midazolam clearance was slower in individuals with primarily macrovesicular steatosis, as evidenced by the significantly higher AUC compared to the group with microvesicular steatosis. Using an alternate steatosis induction protocol, Li and co-workers did not observe any effect of steatosis on midazolam clearance (Li et al. 2017). In contrast, Woolsey and colleagues found that the induction of NASH in humans resulted in an elevation of

the AUC of midazolam and a delay in the clearance rate (Woolsey et al. 2015). Nevertheless, they failed to provide details about the zonation and distribution pattern of steatosis. These results indicate that not only the species and pattern may have an impact but also the etiology of steatosis. In the present study, periportal steatosis did not significantly influence the clearance rate of intraperitoneally administered codeine, which is indicative of CYP2D6 activity. In a study conducted by (Bang et al. 2019), it was observed that severe steatosis in a rat model fed a diet containing 1% orotic acid had a notable influence on the AUC and clearance rate of orally administered metoprolol, which is also a drug substrate of CYP2D6. However, this effect was not observed when metoprolol was administered intravenously. This observation implies that the method of administration may potentially have an impact. The statistical analysis determined a moderate correlation between the severity and extent of macrovesicular steatosis and the AUC of midazolam and codeine.

In contrast, no correlation was observed between the severity and the pattern of steatosis and the AUC of caffeine. In addition, no correlation between microvesicular steatosis and the AUC of any of the three test drugs under investigation was observed. These results support that severity and pattern are relevant factors affecting selected drug metabolism parameters.

The findings of our study indicate a significantly greater level of complexity in the connection between steatosis and drug metabolism. This work is the initial documentation of the observation that drug metabolism is not only influenced by steatosis but also associated with the extent and pattern of fat accumulation. Although steatosis did not affect the distribution pattern, the severity of periportal macrovesicular steatosis was correlated with the activity of pericentrally expressed CYP enzymes and the corresponding drug elimination, as measured by the AUC.

Consequently, regulation of the activity of pericentrally located CYP enzymes could potentially be influenced by factors beyond the presence or absence of fat in the pericentral hepatocytes, suggesting some signaling mechanism as proposed by Ghallab in the case of periportal fibrosis (Ghallab et al. 2019).

This finding is consistent with the previous study by Ghallab and colleagues (Ghallab et al. 2019), which found that periportal fibrosis has a similar impact on metabolic zonation as pericentral fibrosis. In another study (Campos et al. 2020), they proposed an inflammation-associated suppression of metabolic gene networks in acute and chronic liver disease. Moreover, it was revealed that various types of acute and chronic inflammatory stimuli elicited activation of the same gene regulatory networks. Simultaneous upregulation of inflammatory genes and downregulation of metabolic genes were observed. The concept referred to as "Molecular economy of the hepatic acute phase reaction" was introduced by (Ramadori and Christ 1999).

The observation of periportal steatosis altering the activity of particular CYP enzymes could be explained by the assumption that hepatic steatosis, even without significant steatohepatitis, can serve as a moderate inflammatory stimulus. Nevertheless, the observation in the mouse model of chronic intermittent hypoxia suggests that drug metabolism can be modified even without morphological changes. This finding suggests the existence of alternative signaling pathways (Zhang et al. 2018).

These observations call for additional and more comprehensive investigations to explore drug metabolism and potential intralobular signaling pathways. To obtain a comprehensive evaluation of drug metabolism, it is imperative to consider several facets, such as the distribution, expression level, activity, and pharmacokinetics of CYP enzymes. When considering steatosis, it is essential to consider not only the causes, degree, type, and location of fat accumulation but also the presence of inflammatory mediators or other signaling molecules. This approach will aid in understanding the currently observed controversial findings.

5.1.2. Translational relevance and cross-species variability of lobular geometry and zonation of CYP protein expression

The primary objective of experiment B was to examine the interplay between lobular geometry and the zonated expression of essential CYP proteins in four species, namely mice, rats, pigs, and humans.

By utilizing WSIs and our newly developed image analysis pipeline, we successfully measured the lobular geometry and zonal expression of CYP proteins in the liver of all four species, eliminating the need for manual annotation.

5.1.2.1. Automated image analysis pipeline

Our image analysis pipeline facilitated a comprehensive and systematic evaluation of lobular architectures and the spatial arrangement of crucial CYP450 enzymes across four species: mouse, rat, pig, and human. Notably, our approach eliminates the need for manual annotation of the whole slide images, a laborious process that is required by prior techniques for segmenting hepatic lobules (Schwen et al. 2016;Lau et al. 2021;Peleman et al. 2023;Rong et al. 2023). Our pipeline can be seamlessly expanded to measure additional proteins and image modalities, including immunofluorescence, provided that stable zonation markers like GS are present in the staining data. Moreover, our pipeline has the potential to be effortlessly adapted to examine various other tissues, such as the kidney.

Similar to our approach, the tissue positioning system (TPS) presented recently by Rong employs information from various stains to identify the position of the hepatocyte within the lobule based

on K-means clustering (Rong et al. 2023). Our methodology takes an additional step by using positional data to segment the lobular geometry. Compared to TPS, our approach relies on a sequence of serial sections stained with various antibodies, and the corresponding WSI is registered. In contrast, TPS necessitates a single fluorescence WSI involving DAPI, GS, and the proteins of interest. As previously stated, our method can be easily modified for immunofluorescence images, whereas implementing the TPS for conventional IHC may present more difficulties. Implementing image registration and stain separation would require additional computational steps and the recalibration of artificial intelligence (AI) vessel detection. We have successfully showcased the efficacy of our pipeline on samples from various species and liver lobes, while the TPS was exclusively employed on mouse samples. It is interesting to determine if the TPS can be applied to different species, as the geometric variations in size could pose a difficulty for the trained image algorithm.

5.1.2.2. Lobular geometry

Our study has demonstrated that lobular geometry exhibits high robustness and stability, displaying minimal variation within the liver. This holds for both liver lobes and biological replicates while displaying more pronounced differences across different species. We observed increased area and perimeter of the lobules with increasing species size, from mouse to rat, pig, and human. Although the absolute number of liver lobules differs according to the size of the organ in different species, the liver microarchitecture exhibits notable robustness among various species, with only slight variations observed in the corresponding two-dimensional (2D) geometric parameters. This finding has substantial implications for computational liver modeling. It enables the utilization of lobular mathematical models of the liver in various species for simulation purposes, with only slight adjustments required (Ricken et al. 2015;Lambers et al. 2023).

The area and perimeter of the liver lobules were significantly correlated (correlation coefficient $r = 0.99$), whereas compactness and area, respectively compactness and perimeter, were moderately and negatively correlated ($r < 0.65$). This observation implies that the three-dimensional (3D) structure of a hepatic lobule resembles a more or less asymmetric ovoid sphere. To achieve a comprehensive 3D reconstruction of entire hepatic lobules, it is necessary to undertake additional technical efforts beyond simply registering a stack of stained sections to extract the 2D lobular shape. It is imperative to ascertain the 3D structure and arrangement of the liver lobules within the framework of the vascular tree. However, the comprehensive 3D reconstruction of the hepatic lobule, vascular tree, and sinusoidal network presents further computational challenges beyond the current approach.

As part of the work, we created a robust method for non-rigid registration of a small stack of WSI sections, resulting in multiplex protein images. Although the registration process results in a loss of spatial resolution, the obtained results are adequate for identifying lobular geometries and zonation patterns of proteins. However, these results do not provide sufficient information to resolve subcellular details. The workflow described is highly suitable for immunofluorescence WSIs containing multiple proteins. This workflow enables the accurate determination of zonation patterns and lobular geometries with a high level of spatial resolution.
Establishing an image processing workflow is essential for subsequent investigations in imaging and modeling. The established automatic registration and lobule segmentation without prior annotation are also essential for extending the analysis to larger datasets, such as 3D reconstruction of the hepatic lobule and extraction of the vascular and sinusoidal network. Both prerequisites are necessary for simulating flow using actual lobular geometry, which is essential for further simulating the relationship between perfusion and function.

5.1.2.3. CYP zonal expression

Drug metabolism studies have been conducted in human subjects and experimental animals from various species over many years. All these studies are based on the assumption that the findings obtained from animal studies reflect the clinical situation.
However, there has been limited focus on the spatial distribution and zonal expression of CYP proteins in various species despite its potential relevance in elucidating variations in drug metabolism and toxicity across species. We systematically analyzed the spatial distribution and zonation patterns of four CYP450 enzymes (CYP1A2, CYP2D6, CYP2E1, and CYP3A4) in four species, namely mice, rats, pigs, and humans. We only found one other study regarding the zonal distribution and expression of CYPs, comparing the panlobular expression of CYP3A4 in the liver of adult minipigs. They also described the reported pericentral to midzonal expression observed in humans (Van Peer et al. 2014).
The extent and zonal distribution of CYP expression are likely to impact metabolic activity significantly and can be crucial for interpreting translational studies. Significant similarities were observed in zonal GS and CYP2E1 expression across different species. Our findings are consistent with previous research conducted by (Martignoni et al. 2006), which also reported a high level of similarity in catalytic activity. The researchers concluded that there were no significant variations in CYP2E1 activity across different species, and the ability to extrapolate between species was quite reliable. On the other hand, our study has observed substantial interspecies variations in the expression pattern and catalytic activity of the species-specific isoforms of CYP1A, namely -2C, -2D, and -3A (Martignoni et al. 2006;Dalgaard 2015). The observed

variations in hepatotoxicity may be attributed to variations in the degree of expression and catalytic activity.

Understanding the distinct characteristics of drug metabolism in different species, including variations and similarities in CYP patterns, will enhance our ability to predict efficacy and toxicity in a given species. This knowledge could influence drug testing and preclinical drug development and contribute to the development of safer and more efficient therapeutic strategies.

5.1.2.4. Minimal number of lobules

In clinical pathology, assessing a minimum number of lobules is strongly advised to achieve a sound pathological diagnosis. Misdiagnosis can occur due to insufficient sample size, particularly in cases where the minimum number of portal fields is not acquired, the disease process is confined to a specific area, and the interpreter needs more expertise. According to (Sherlock and Dooley 2002), the ideal length for a liver biopsy is 1-4 cm, and the weight should be between 10-50 mg. According to (Bravo et al. 2001), most hepato-pathologists rely on biopsy specimens that include a minimum of six to eight portal triads. This is particularly relevant for diagnosing and grading chronic liver disease, where the severity may differ between hepatic lobules. According to a recent study conducted by (Agarwal et al. 2022), it has been found that to accurately diagnose allograft rejection, a clinical liver biopsy should represent a minimum of 10 complete portal fields. This number comes exclusively from pathological expertise and does not rely on precise measurement of lobular shape and staining patterns.

In the present study, we determined the minimum number of lobules necessary for calculating geometric parameters such as area and perimeter, protein zonation patterns, and percentage of stained area. Notably, the minimum number of lobules necessary for a reliable quantitative examination of lobular geometry differed depending on the parameter and the accepted error margin for the estimate. On the one hand, the compactness exhibited the highest level of robustness, necessitating only 2.2 to 3.8 lobules for the desired diagnostic reliability. On the other hand, the area exhibited a lower level of robustness, requiring a range of 44.5 to 82.4 lobules to achieve a confidence level of 95% with a margin of error of 20%. The need for a substantial number of lobules to obtain a reliable estimation of lobular geometry arises from substantial variations in geometric parameters observed among different lobules within a single subject. On the contrary, the mean values among individuals or even species exhibit high similarity.

The quantification of the minimum number of lobules necessary for evaluating the zonated distribution exhibited significant variations across different species. The primary determinant of the large number of required lobules was the substantial coefficient of variation in the protein quantity across spatial locations. In other words, as the zonation patterns between different lobules

within a sample became more heterogeneous, the number of lobules required for a dependable estimation increased. The observed variations in zonation patterns across distinct lobules may have significant consequences for the toxicity or the spatial regulation of drug metabolism.

When conducting the same calculation for CYP staining, it was found that a significantly smaller number of lobules was needed to achieve the same level of confidence regarding the relative area covered by a specific stain. Reliable quantification in rat and mouse livers required fewer than ten lobules. For pig liver, 10-20 lobules were needed, and for human livers, 10-50 lobules, depending on the CYP enzyme. In other words, the number of lobules required was related to the specific protein and the species under investigation.

In this study, we only examined normal livers from the four species. Structural abnormalities are highly likely to increase the minimum number of lobules. As anticipated, an increase in the variability of the measurement of interest across various lobules necessitates a greater number of lobules to obtain a dependable estimation of the parameter. Even basic measurements like the lobular area necessitate a substantial number of lobules, which can be acquired from a WSI of a large liver sample but not from a single liver core biopsy. Significant spatial variability in numerous parameters employed in histopathological scoring systems poses a considerable obstacle to achieving reliable assessment.

Taken together, the minimum number of lobules is related to various factors, including the species, the parameters in question, and potentially the morphology of the liver. In numerous instances, this numerical value exhibits a significant disparity compared to the standard pathological criteria for clinical diagnosis. The findings of our study indicate that it is advisable to be cautious when interpreting quantitative analyses of clinical biopsies. The findings of this study may have significant implications for clinical pathology, where the number of lobules determined here cannot be acquired with a single biopsy.

In conclusion, we have introduced an automated approach to evaluating the shape and pattern of lobular structures using WSI without manual image annotation. With this approach, we can systematically compare the lobular structures and the distribution and expression of crucial CYP enzymes (CYP1A2, CYP2D6, CYP2E1, and CYP3A4) and GS in different animal species (mouse, rat, pig, and human).

Based on our resulrs, zonated CYP expression in mice is most similar to humans. Therefore, mice appear to be the most appropriate species for drug metabolism studies unless larger animals are required for other reasons, e.g., when studying the impact of surgical procedures on drug metabolism. CYP2E1 and CYP2D6 could be the CYP enzyme of choice to analyze when comparing the four different species. CYP1A2 could also be considered an additional CYP

enzyme for comparing rodents and humans. If only mice and humans were compared, CYP3A4 could also be used.

In summary, our image analysis pipeline and recommendations for species and CYP enzyme selection can help improve cross-species and translational drug metabolism studies.

5.2. Implications for future studies

5.2.1. Impact of steatosis on zonated parameters of drug metabolism in humans

As mentioned before, the impact of steatosis on CYP-mediated drug metabolism has been discussed controversially. Experimental and clinical studies consistently reveal that CYP3A4 is downregulated in fatty liver, either in terms of its activity, expression level, and/or pharmacokinetics (Weltman et al. 1996;Stärkel et al. 2003;Bell et al. 2010;Hata et al. 2010;Merrell and Cherrington 2011;Kostrzewski et al. 2017). In contrast, most but not all human and animal studies report that CYP2E1 activity or expression is upregulated in non-alcoholic steatohepatitis (Weltman et al. 1996;Weltman et al. 1998;Bell et al. 2010;Jiang et al. 2016;Rey-Bedon et al. 2022). However, some authors observed contradictory observations, as summarized in Appendix, Table S 3. For example, Fisher et al. (2009) reported a decrease in the mRNA and protein expression of CYP2E1 in patients with hepatic steatosis (Fisher et al. 2009). Similarly, as mentioned before, Stärkel et al. (2003) observed that CYP2E1 activity and mRNA expression decreased in rodents fed an MCD diet (Stärkel et al. 2003). So far, little emphasis has been placed on a detailed description of the underlying etiology affecting the degree, type, and zonation of fat accumulation. These factors may influence CYP expression patterns and activity, thus, CYP-mediated functions such as drug metabolism.

Our finding that periportal steatosis affects distinct parameters of pericentrally located drug metabolism supports the groundbreaking observation of Ghallab and his group (Ghallab et al. 2019). He demonstrated that periportal fibrosis affects pericentral metabolic processes similarly to pericentral fibrosis. However, they did not investigate the functional activity of the CYP enzymes. Complementary to Ghallab, we observed that even moderate periportal steatosis did affect not all but distinct parameters of pericentral drug metabolism.

Our findings from the first study are noticeable from a scientific point of view and could even have a certain translational impact. It is scientifically of interest to better understand metabolic zonation, the processes impairing it, and the resulting impact on overall function. The findings could also be of clinical relevance to better understand the potential side effects of drugs in patients with hepatic steatosis.

For instance, patients with hepatic steatosis may experience altered clearance rates of certain drugs, such as paracetamol and tamoxifen, leading to increased drug concentrations and a higher

risk of toxicity (Massart et al. 2017). As reported by Miele in 2017, “there is growing awareness of the potential risk factors for drug-induced liver injury due to the underlying metabolic condition” (Miele et al. 2017). Furthermore, steatosis patients may suffer from aggravation of NAFLD in case of being treated with drugs affecting lipid metabolism (Tarantino et al. 2009). These examples highlight the importance of understanding the potential side effects of drugs in this patient population.

In experiment A, we showed that steatosis did affect the activity of certain CYP enzymes that metabolize potentially hepatotoxic drugs such as methotrexate. This could increase the risk of developing drug-induced liver injury or drug-induced steatohepatitis.

Nevertheless, it is important to acknowledge that the translation of findings from animal models to humans may not always be straightforward due to underlying biological differences. Results obtained in controlled laboratory conditions may only partially reflect the complexity of the human liver. Further research is required to validate the findings in humans and to determine the extent of their relevance in the clinical context. Therefore, we want to continue our cross-species analysis in two directions to improve prediction and select more species-independent parameters. Firstly, we need to examine the spatial expression of drug-metabolizing enzymes in steatotic samples from the four species. Secondly, we need to investigate other features of drug metabolism, such as mRNA expression, protein expression, and activity.

In a further step, we plan to investigate the effect of zonal steatosis on drug metabolism in humans. We will compare the effect of predominantly periportal versus pericentral steatosis. If the results obtained by (Ghallab et al. 2019) using a mouse model of periportal fibrosis and our results using a mouse model of periportal steatosis can be translated. We anticipate a similar effect on periportal versus pericentral steatosis. However, this effect is likely to be limited to specific aspects of drug metabolism, such as CYP 1A2 and 2E1, but may not necessarily affect drug metabolism in total, which makes it impossible to come up with a general recommendation.

5.2.2. Cross-species analysis of fat distribution and implications on spatial expression of drug-metabolizing enzymes

So far, as described in the translational study in experiment B, we have examined exclusively normal livers in the four species. Structural abnormalities are quite likely to cause an increase in the minimum number of lobules. We expect that higher variability in the targeted readout among different lobules will require to examine a higher number of lobules to obtain a reliable estimate of the parameter. The spatial distribution of expression in healthy animals is not necessarily predictive of the expression under disease conditions.

Therefore, we want to develop our image analysis pipeline further for the zonated quantification of steatosis. Here, we plan to include livers with steatosis from the four species to assess the impact of the disease on lobule variability. By examining livers with steatosis, we aim to determine whether the structural abnormalities caused by the disease result in a further increase in the minimum number of lobules required for accurate parameter estimation. Additionally, we aim to investigate whether the spatial distribution of CYP expression in steatotic livers from different species differs from that of healthy livers.

Furthermore, the spatial distribution of CYP expression is not necessarily predictive of the activity of the given CYP enzyme. Various factors influence enzyme activity, such as post-translational modifications, protein-protein interactions, and co-factors (Kokkinidis et al. 2020). Therefore, we plan a subsequent study to investigate mRNA expression, protein content, and *in vitro* activity across various species, including mice, rats, and humans. By doing that, we will gain insights into the impact of steatosis on features of drug metabolism in different species. This knowledge will help to better select a suitable animal model for translational drug metabolism studies.

5.2.3. Heterogeneity of fat distribution as an additional factor influencing result interpretation

Hepatic steatosis can manifest with a widespread, almost diffuse, segmental, or localized distribution. Diffuse fatty infiltration of the liver can result in hepatomegaly, which is even detectable upon clinical examination due to the round borders of the liver. In cases of non-diffuse steatosis, the fat might be distributed anatomically (segmental steatosis) or non-anatomically (focal steatosis) (Bazzocchi et al. 2008). This is not an uncommon finding and has been reported repeatedly (Capitan et al. 2012;Choi et al. 2015;Keramida et al. 2016). However, clinical assessment of hepatic steatosis is mainly based on imaging technologies with a much lower resolution compared to histology. In other words, the extent of heterogeneity in fat distribution and the impact of fat distribution on drug metabolism have not yet been fully explored clinically.

Based on histological data, we observed in mice (Schwen et al. 2016), but also in rats (Homeyer et al. 2018), a striking heterogeneity in the lobar distribution of hepatic steatosis on all levels, in terms of interlobular variation, lobar variation, and inter-individual variation. One extreme example of this striking heterogeneity is shown in (Figure 9).

However, the reason for the heterogeneous spatial distribution of fat in the liver is unclear. This heterogeneity may pose problems when only obtaining a small biopsy from the large liver, as done clinically (Arun et al. 2007). In this case, it remains rather unclear whether the given sample truly represents the condition of the total organ. Therefore, we subjected tissue from four distinct liver

lobes of each animal for histological analysis to reach a sound quantification. Using WSI facilitated the automated analysis of these large samples.

To get a better idea of the spatial distribution of drug metabolism enzymes, we plan to examine not only the heterogeneity of steatosis but also the key parameters of drug metabolism in the mouse model. Here, we want to quantify steatosis in whole mouse livers based on image analysis of whole slide scans and biochemical quantification in cryo samples. Furthermore, we want to investigate CYP mRNA, protein, and activity in multiple samples of mouse livers. By doing so, we will estimate the heterogeneity of fat distribution and its eventual impact on drug metabolism.

5.2.4. Computational modeling as an additional tool to support further investigations Improvement of study design Improvement of understanding using computational modeling

Computational modeling is crucial for predicting physiological responses under different conditions and will, in the long run, facilitate the clinical translation of data (Lerapetritou et al. 2009). In a recent joint cooperative work (Lambers et al. 2024), we created a multiscale mathematical model to simulate fat zonation and metabolism by incorporating hepatic lobular geometry, physiologically relevant microperfusion, and oxygen distribution on lobular and cellular scales (Figure 21). This mathematical computational model facilitates the prediction of zonated fat accumulation in the hepatic lobule by considering aspects such as perfusion, oxygen levels, plasma-FFA content, oxidative processes, and triglyceride generation.

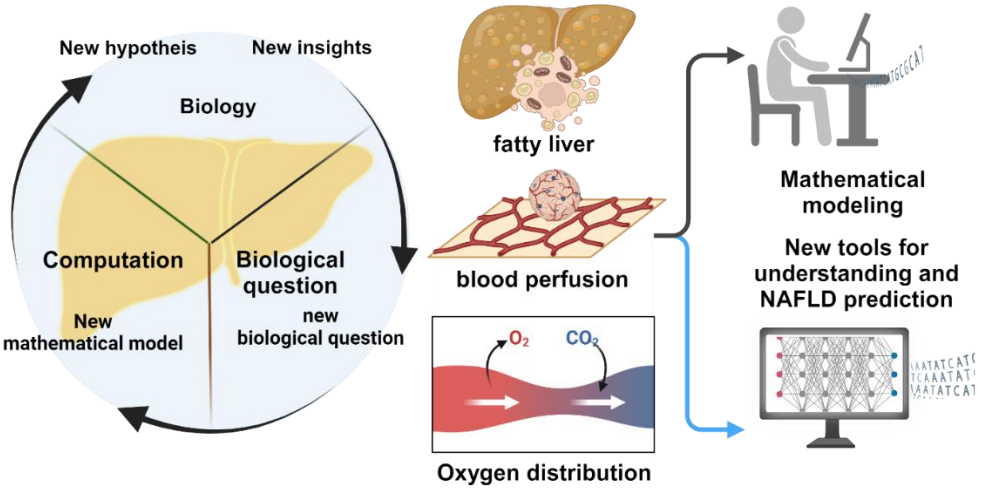

Figure 24. Overview of modeling implication for better understanding of NAFLD. “Created with BioRender.com.”

In a subsequent recent computational study (Steffen et al. 2024), the perfusion-zonation-function relationship for drug-induced lobular necrosis pattern was modeled. A partial differential equation-

based porous media approach for the liver lobule was coupled with Ordinary differential equation-based models on a cellular scale. In this approach, the Ordinary differential equation-based models on a cellular scale were used to describe hepatic metabolism and distribution of drug-metabolizing enzymes. In contrast, the porous media-based models represented transport and tissue-mechanical properties and deformations on the lobulus scale.

Implementing these modeling approaches in the planned observational clinical study will hopefully contribute to a better understanding of the impact of periportal respectively pericentral steatosis on the portalization of drug-metabolizing enzymes.

6. Summary

Background: It was recently reported that periportal fibrosis in mice did affect the expression of CYP proteins, a set of pericentrally located drug-metabolizing enzymes. This observation suggests an interplay between zonated morphological disorders and metabolic zonation, a potentially clinically relevant finding. Therefore, we raised the hypothesis that periportal steatosis in mice may affect zonated drug metabolism parameters. Cross-species variation has not yet been systematically explored with respect to hepatic lobular geometry and CYP expression as needed for clinical translation. We hypothesized that lobular geometry as an anatomical feature is species-independent, whereas CYP zonal expression as a functional parameter is species-dependent.

Method: We performed a detailed drug metabolism study in mice with periportal steatosis induced by feeding a high-fat methionine-choline reduced diet applied over two, respectively, four weeks. Drug metabolism was assessed in terms of the spatial distribution of drug-metabolizing CYP enzymes, CYP activity, and a pharmacokinetic study. For the cross-species analysis, we involved four species: mouse, rat, pig, and human. We developed an automated pipeline based on whole slide images (WSI) of hematoxylin-eosin-stained liver sections and immunohistochemistry to quantify lobular geometry and zonated expression of key cytochrome P450 (CYP) enzymes.

Results: Periportal steatosis did not alter the pericentral expression pattern of the CYP enzymes. However, the activity of selected CYPs was related to the type and severity of steatosis. Caffeine elimination was accelerated by microvesicular steatosis, whereas midazolam elimination was delayed in macrovesicular steatosis. Using the newly developed automated image analysis pipeline, we observed that hepatic lobular geometry is rather robust, whereas zonated expression shows species-specific features, with mice being most similar to humans.

Conclusion: In this thesis, we demonstrated that periportal pathology such as steatosis could affect certain features of hepatic drug metabolism, a metabolic process taking place in the pericentral region. We demonstrated the robustness of lobular geometry in four different species and described the impact of the given species on the spatial distribution of CYP proteins in normal livers.

Perspective: Our planned future studies include assessing species-specific features of steatosis, including heterogeneity, and their implications for the spatial distribution of CYP expression. Based on this data, we want to perform a translational study using human samples to confirm the impact of periportal and pericentral steatosis on distinct parameters of drug metabolism**.**

7. Zusammenfassung

Auswirkungen der Steatose auf den Arzneimittelstoffwechsel der Leber: Funktionelle und translationale Implikationen

Hintergrund: Vor kurzem wurde berichtet, dass die periportale Fibrose bei Mäusen die perizentrale Expression von Proteinen des Arzneimittelstoffwechsel (CYP-Enzymen), beeinträchtigt. Diese Beobachtung impliziert eine Wechselwirkung zwischen zonierten morphologischen Störungen und metabolischer Zonierung, einem potenziell klinisch relevanten Phänomen. Daher stellten wir die Hypothese auf, dass die periportale Steatose bei Mäusen die Parameter des zonierten Arzneimittelstoffwechsels beeinflussen könnte. Speziesübergreifende Unterschiede in Bezug auf die hepatische Läppchengeometrie und CYP-Expression wurden noch nicht systematisch untersucht, was für weitere translationale Stedien jedoch wichtg ist. Daher postulierten wir, dass die lobuläre Geometrie als anatomisches Merkmal spezies-unabhängig ist, während die Zonale CYP Expression als funktioneller Parameter spezies-abhängig ist.

Methode: Wir untersuchten den Arzneimittelstoffwechsels bei Mäusen mit periportaler Steatose, die durch eine fettreiche, methionin-cholinreduzierte Diät über 2 bzw. 4 Wochen induziert wurde. Der Arzneimittelstoffwechsel wurde anhand der räumlichen Verteilung der CYP-Enzyme, der CYP-Aktivität und einer pharmakokinetischen Studie untersucht. Für die speziesübergreifende Analyse haben wir vier Spezies herangezogen: Maus, Ratte, Schwein und Mensch. Wir haben eine automatisierte Bildanalyse-Pipeline entwickelt, die Ganzbildaufnahmen (WSI) von Hämatoxylin-Eosin- und immunhistochemisch gefärbten Leberschnitten nutzt, um die lobuläre Geometrie und die zonierte Expression von Cytochrom P450 Enzymen zu quantifizieren.

Ergebnisse: Die periportale Steatose veränderte das perizentrale Expressionsmuster der CYP-Enzyme nicht. Die Aktivität ausgewählter CYPs war jedoch mit Schweregrad und Typ der Steatose assoziiert. Die Eliminiation von Koffein wurde durch mikrovesikuläre Steatose beschleunigt, während die von Midazolam bei makrovesikulärer Steatose verzögert war. Mit der automatisierten Bildanalyse-Pipeline konnten wir feststellen, dass die lobuläre Geometrie der Leber recht robust ist, während die zonierte Expression artspezifische Merkmale aufweist.

Zusammenfassung: Wir haben gezeigt, dass die periportale Steatose bestimmte Merkmale des hepatischen Arzneimittelstoffwechsels beeinflussen kann. Wir haben die Robustheit der lobulären Geometrie bei vier verschiedenen Spezies nachgewiesen und die Spezies-abhängige räumliche Verteilung der CYP-Proteine in normalen Lebern beschrieben.

Ausblick: Künftig wollen wir die speziesabhängigen Auswirkungen der Steatose und ihrer heterogenen Verteilung auf die zonierte Expression von CYP-Enzymen untersuchen. Auf der Grundlage dieser Daten planen wir eine translationale klinische Studie, um die Auswirkungen der

periportalen und perizentralen Steatose auf verschiedene Parameter des Arzneimittelstoffwechsels zu bestätigen.

8. References

Abdelmegeed, M. A., A. Banerjee, S.-H. Yoo, S. Jang, F. J. Gonzalez and B.-J. Song (2012):

Critical role of cytochrome P450 2E1 (CYP2E1) in the development of high fat-induced non-alcoholic steatohepatitis.

Journal of Hepatology 57: 860-866. DOI: 10.1016/j.jhep.2012.05.019.

Agarwal, A. N., J. Nania, L. Qiu, B. Lewis and D. D. Mais (2022):

Impact of Liver Biopsy Size on Histopathologic Evaluation of Liver Allograft Rejection.

Arch Pathol Lab Med 146: 1530-1534. DOI: 10.5858/arpa.2021-0257-OA.

Aitio, A. (1978):

A simple and sensitive assay of 7-ethoxycoumarin deethylation.

Anal Biochem 85: 488-491. DOI: 10.1016/0003-2697(78)90245-2.

Albadry, M., S. Höpfl, N. Ehteshamzad, M. König, M. Böttcher, J. Neumann, A. Lupp, O. Dirsch, N. Radde, B. Christ, M. Christ, L. O. Schwen, H. Laue, R. Klopfleisch and U. Dahmen (2022):

Periportal steatosis in mice affects distinct parameters of pericentral drug metabolism.

Scientific Reports 12: 21825. DOI: 10.1038/s41598-022-26483-6.

Albadry, M., J. Küttner, J. Grzegorzewski, O. Dirsch, E. Kindler, R. Klopfleisch, V. Liska, V. Moulisova, S. Nickel, R. Palek, J. Rosendorf, S. Saalfeld, U. Settmacher, H. M. Tautenhahn, M. König and U. Dahmen (2024):

Cross-species variability in lobular geometry and cytochrome P450 hepatic zonation: insights into CYP1A2, CYP2D6, CYP2E1 and CYP3A4.

Front Pharmacol 15: 1404938. DOI: 10.3389/fphar.2024.1404938.

Aljomah, G., S. S. Baker, W. Liu, R. Kozielski, J. Oluwole, B. Lupu, R. D. Baker and L. Zhu (2015):

Induction of CYP2E1 in non-alcoholic fatty liver diseases.

Experimental and Molecular Pathology 99: 677-681. DOI: 10.1016/j.yexmp.2015.11.008.

Almazroo, O. A., M. K. Miah and R. Venkataramanan (2017):

Drug Metabolism in the Liver.

Clinics in Liver Disease 21: 1-20. DOI: 10.1016/j.cld.2016.08.001.

Arun, J., N. Jhala, A. J. Lazenby, R. Clements and G. A. Abrams (2007):

Influence of liver biopsy heterogeneity and diagnosis of nonalcoholic steatohepatitis in subjects undergoing gastric bypass.

Obes Surg 17: 155-161. DOI: 10.1007/s11695-007-9041-2.

Bailey, J. and M. Balls (2019):

Recent efforts to elucidate the scientific validity of animal-based drug tests by the pharmaceutical industry, pro-testing lobby groups, and animal welfare organisations.

BMC Med Ethics 20: 16. DOI: 10.1186/s12910-019-0352-3.

Bailey, J., M. Thew and M. Balls (2014):

An analysis of the use of animal models in predicting human toxicology and drug safety.

Altern Lab Anim 42: 181-199. DOI: 10.1177/026119291404200306.

Baillie, T. A. and A. E. Rettie (2011):

Role of Biotransformation in Drug-Induced Toxicity: Influence of Intra-and Inter-Species Differences in Drug Metabolism.

Drug Metabolism and Pharmacokinetics 26: 15-29. DOI: DOI 10.2133/dmpk.DMPK-10-RV-089.

Bang, W. S., Y. R. Hwang, Z. Li, I. Lee and H. E. Kang (2019):

Effects of Orotic Acid-Induced Non-Alcoholic Fatty Liver on the Pharmacokinetics of Metoprolol and its Metabolites in Rats.

J Pharm Pharm Sci 22: 98-111. DOI: 10.18433/jpps30268.

Bazzocchi, M., G. Como and C. Franchini (2008):

Steatosis, Hepatic.

Encyclopedia of Diagnostic Imaging. A. L. Baert. Berlin, Heidelberg, Springer Berlin Heidelberg: 1741-1744.

Bell, L. N., C. J. Temm, R. Saxena, R. Vuppalanchi, P. Schauer, M. Rabinovitz, A. Krasinskas, N. Chalasani and S. G. Mattar (2010):

Bariatric surgery-induced weight loss reduces hepatic lipid peroxidation levels and affects hepatic cytochrome P-450 protein content.

Ann Surg 251: 1041-1048. DOI: 10.1097/SLA.0b013e3181dbb572.

Ben-Moshe, S., Y. Shapira, A. E. Moor, R. Manco, T. Veg, K. Bahar Halpern and S. Itzkovitz (2019):

Spatial sorting enables comprehensive characterization of liver zonation.

Nat Metab 1: 899-911. DOI: 10.1038/s42255-019-0109-9.

Bf3R (2022):

Verwendung von Versuchstieren im Berichtsjahr 2022, Bf3R "Deutschen Zentrums zum Schutz von Versuchstieren".

Bradski, G. and A. Kaehler (2008):

Learning OpenCV: Computer vision with the OpenCV library.

Corporate Headquarters, 1005 Gravenstein Highway North, Sebastopol, CA 95472 USA, O'Reilly Media, Inc.

Bravo, A. A., S. G. Sheth and S. Chopra (2001):

Liver biopsy.

N Engl J Med 344: 495-500. DOI: 10.1056/NEJM200102153440706.

Brunt, E. M. (2007):

Pathology of fatty liver disease.

Mod Pathol 20 Suppl 1: S40-48. DOI: 10.1038/modpathol.3800680.

Bryda, E. C. (2013):

The Mighty Mouse: the impact of rodents on advances in biomedical research.

Mo Med 110: 207-211.

Burt, A. D., C. Lackner and D. G. Tiniakos (2015):

Diagnosis and Assessment of NAFLD: Definitions and Histopathological Classification.

Semin Liver Dis 35: 207-220. DOI: 10.1055/s-0035-1562942.

Campos, G., W. Schmidt-Heck, J. De Smedt, A. Widera, A. Ghallab, L. Putter, D. Gonzalez, K. Edlund, C. Cadenas, R. Marchan, R. Guthke, C. Verfaillie, C. Hetz, A. Sachinidis, A. Braeuning, M. Schwarz, T. S. Weiss, B. K. Banhart, J. Hoek, R. Vadigepalli, J. Willy, J. L. Stevens, D. C. Hay, J. G. Hengstler and P. Godoy (2020):

Inflammation-associated suppression of metabolic gene networks in acute and chronic liver disease.

Arch Toxicol 94: 205-217. DOI: 10.1007/s00204-019-02630-3.

Capitan, V., J. M. Petit, S. Aho, P. H. Lefevre, S. Favelier, R. Loffroy, P. Hillon, D. Krause, J. P. Cercueil and B. Guiu (2012):

Macroscopic heterogeneity of liver fat: an MR-based study in type-2 diabetic patients.

Eur Radiol 22: 2161-2168. DOI: 10.1007/s00330-012-2468-4.

Chang, T. K., C. L. Crespi and D. J. Waxman (2006):

Spectrophotometric analysis of human CYP2E1-catalyzed p-nitrophenol hydroxylation.

Methods Mol Biol 320: 127-131. DOI: 10.1385/1-59259-998-2:127.

Choi, Y., J. M. Lee, N. J. Yi, H. Kim, M. S. Park, G. Hong, T. Yoo, S. W. Suh, H. W. Lee, K. W. Lee and K. S. Suh (2015):

Heterogeneous living donor hepatic fat distribution on MRI chemical shift imaging.

Ann Surg Treat Res 89: 37-42. DOI: 10.4174/astr.2015.89.1.37.

Cobbina, E. and F. Akhlaghi (2017):

Non-alcoholic fatty liver disease (NAFLD) – pathogenesis, classification, and effect on drug metabolizing enzymes and transporters.

Drug Metabolism Reviews 49: 197-211. DOI: 10.1080/03602532.2017.1293683.

Cozzi, E., E. Bosio, M. Seveso, D. Rubello and E. Ancona (2009):

Xenotransplantation as a model of integrated, multidisciplinary research.

Organogenesis 5: 14-22. DOI: 10.4161/org.7578.

Dalgaard, L. (2015):

Comparison of minipig, dog, monkey and human drug metabolism and disposition.

J Pharmacol Toxicol Methods 74: 80-92. DOI: 10.1016/j.vascn.2014.12.005.

Day, C. P. (2006):

From fat to inflammation.

Gastroenterology 130: 207-210. DOI: 10.1053/j.gastro.2005.11.017.

Deng, M. H., U. Dahmen, J. Sun, H. Huang, C. Sehestedt, A. Homeyer, A. Schenk and O. Dirsch (2014):

Limited Correlation Between Conventional Pathologist and Automatic Computer-Assisted Quantification of Hepatic Steatosis due to Difference Between Event-Based and Surface-Based Analysis.

Ieee Journal of Biomedical and Health Informatics 18: 1473-1477. DOI: 10.1109/Jbhi.2013.2282999.

Donato, M. T., N. Jiménez, A. Serralta, J. Mir, J. V. Castell and M. J. Gómez-Lechón (2007):

Effects of steatosis on drug-metabolizing capability of primary human hepatocytes.

Toxicology in Vitro 21: 271-276. DOI: 10.1016/j.tiv.2006.07.008.

Donato, M. T., A. Lahoz, N. Jimenez, G. Perez, A. Serralta, J. Mir, J. V. Castell and M. J. Gomez-Lechon (2006):

Potential impact of steatosis on cytochrome P450 enzymes of human hepatocytes isolated from fatty liver grafts.

Drug Metab Dispos 34: 1556-1562. DOI: 10.1124/dmd.106.009670.

Estes, C., H. Razavi, R. Loomba, Z. Younossi and A. J. Sanyal (2018):

Modeling the epidemic of nonalcoholic fatty liver disease demonstrates an exponential increase in burden of disease.

Hepatology 67: 123-133. DOI: 10.1002/hep.29466.

European Association for the Study of the Liver, European Association for the Study of Diabetes and E. A. f. t. S. o. Obesity (2016):

EASL-EASD-EASO Clinical Practice Guidelines for the management of non-alcoholic fatty liver disease.

J Hepatol 64: 1388-1402. DOI: 10.1016/j.jhep.2015.11.004.

Farrell, G. C., N. C. Teoh and R. S. McCuskey (2008):

Hepatic microcirculation in fatty liver disease.

Anat Rec (Hoboken) 291: 684-692. DOI: 10.1002/ar.20715.

Fisher, C. D., A. J. Lickteig, L. M. Augustine, J. Ranger-Moore, J. P. Jackson, S. S. Ferguson and N. J. Cherrington (2009):

Hepatic Cytochrome P450 Enzyme Alterations in Humans with Progressive Stages of Nonalcoholic Fatty Liver Disease.

Drug Metabolism and Disposition 37: 2087-2094. DOI: 10.1124/dmd.109.027466.

Fröhlich, F., D. Weindl, Y. Schälte, D. Pathirana, Ł. Paszkowski, G. T. Lines, P. Stapor and J. Hasenauer (2021):

AMICI: high-performance sensitivity analysis for large ordinary differential equation models.

Bioinformatics 37: 3676-3677.

Fromenty, B. (2019):

Inhibition of mitochondrial fatty acid oxidation in drug-induced hepatic steatosis.

Liver Research 3: 157-169.

Garza, A. Z., S. B. Park and R. Kocz (2022):

Drug elimination.

[Updated 2022 Jul 11]. In: StatPearls [Internet]. Treasure Island (FL): StatPearls Publishing. Available from: https://www.ncbi.nlm.nih.gov/books/NBK547662/.

Gatenbee, C. D., A. M. Baker, S. Prabhakaran, O. Swinyard, R. J. C. Slebos, G. Mandal, E. Mulholland, N. Andor, A. Marusyk, S. Leedham, J. R. Conejo-Garcia, C. H. Chung, M. Robertson-Tessi, T. A. Graham and A. R. A. Anderson (2023):

Virtual alignment of pathology image series for multi-gigapixel whole slide images.

Nat Commun 14: 4502. DOI: 10.1038/s41467-023-40218-9.

Gebhardt, R. (1992):

Metabolic zonation of the liver: regulation and implications for liver function.

Pharmacol Ther 53: 275-354. DOI: 10.1016/0163-7258(92)90055-5.

Geweke, J. F. (1991):

Evaluating the accuracy of sampling-based approaches to the calculation of posterior moments, Federal Reserve Bank of Minneapolis. Staff Report 148.

Ghallab, A., M. Myllys, C. H. Holland, A. Zaza, W. Murad, R. Hassan, Y. A. Ahmed, T. Abbas, E. A. Abdelrahim, K. M. Schneider, M. Matz-Soja, J. Reinders, R. Gebhardt, M. L. Berres, M. Hatting, D. Drasdo, J. Saez-Rodriguez, C. Trautwein and J. G. Hengstler (2019):

Influence of Liver Fibrosis on Lobular Zonation.

Cells 8. DOI: 10.3390/cells8121556.

Gillies, S., C. van der Wel, J. Van den Bossche, M. W. Taves, J. Arnott and B. C. Ward (2023):

Shapely (2.0.2).

Zenodo. https://doi.org/10.5281/zenodo.8436711.

Gluchowski, N. L., M. Becuwe, T. C. Walther and R. V. Farese, Jr. (2017):

Lipid droplets and liver disease: from basic biology to clinical implications.

Nat Rev Gastroenterol Hepatol 14: 343-355. DOI: 10.1038/nrgastro.2017.32.

Goode, A., B. Gilbert, J. Harkes, D. Jukic and M. Satyanarayanan (2013):

OpenSlide: A vendor-neutral software foundation for digital pathology.

J Pathol Inform 4: 27. DOI: 10.4103/2153-3539.119005.

Griffen, S. C., J. Wang and M. S. German (2001):

A genetic defect in beta-cell gene expression segregates independently from the fa locus in the ZDF rat.

Diabetes 50: 63-68. DOI: 10.2337/diabetes.50.1.63.

Guido, M., S. Sarcognato, D. Sacchi and K. Ludwig (2019):

The anatomy and histology of the liver and biliary tract.

Pediatric Hepatology and Liver Transplantation: 41-55.

Hajar, R. (2011):

Animal testing and medicine.

Heart Views 12: 42. DOI: 10.4103/1995-705X.81548.

Hammer, H., F. Schmidt, P. Marx-Stoelting, O. Potz and A. Braeuning (2021):

Cross-species analysis of hepatic cytochrome P450 and transport protein expression.

Arch Toxicol 95: 117-133. DOI: 10.1007/s00204-020-02939-4.

Hata, S., Y. Miki, F. Fujishima, R. Sato, A. Okaue, K. Abe, K. Ishida, J. Akahira, M. Unno and H. Sasano (2010):

Cytochrome 3A and 2E1 in human liver tissue: Individual variations among normal Japanese subjects.

Life Sciences 86: 393-401. DOI: 10.1016/j.lfs.2010.01.011.

Homeyer, A., S. Hammad, L. O. Schwen, U. Dahmen, H. Hofener, Y. Gao, S. Dooley and A. Schenk (2018):

Focused scores enable reliable discrimination of small differences in steatosis.

Diagn Pathol 13: 76. DOI: 10.1186/s13000-018-0753-5.

Homeyer, A., A. Schenk, J. Arlt, U. Dahmen, O. Dirsch and H. K. Hahn (2015):

Fast and accurate identification of fat droplets in histological images.

Comput Methods Programs Biomed 121: 59-65. DOI: 10.1016/j.cmpb.2015.05.009.

Hrycay, E. G. and S. M. Bandiera (2009):

Expression, function and regulation of mouse cytochrome P450 enzymes: comparison with human P450 enzymes.

Curr Drug Metab 10: 1151-1183. DOI: 10.2174/138920009790820138.

Hucka, M., A. Finney, H. M. Sauro, H. Bolouri, J. C. Doyle, H. Kitano, A. P. Arkin, B. J. Bornstein, D. Bray, A. Cornish-Bowden, A. A. Cuellar, S. Dronov, E. D. Gilles, M. Ginkel, V. Gor, Goryanin, II, W. J. Hedley, T. C. Hodgman, J. H. Hofmeyr, P. J. Hunter, N. S. Juty, J. L. Kasberger, A. Kremling, U. Kummer, N. Le Novere, L. M. Loew, D. Lucio, P. Mendes, E. Minch, E. D. Mjolsness, Y. Nakayama, M. R. Nelson, P. F. Nielsen, T. Sakurada, J. C. Schaff, B. E. Shapiro, T. S. Shimizu, H. D. Spence, J. Stelling, K. Takahashi, M. Tomita, J. Wagner, J. Wang and S. Forum (2003):

The systems biology markup language (SBML): a medium for representation and exchange of biochemical network models.

Bioinformatics 19: 524-531. DOI: 10.1093/bioinformatics/btg015.

Jamwal, R., B. J. Barlock, S. Adusumalli, K. Ogasawara, B. L. Simons and F. Akhlaghi (2017):

Multiplex and Label-Free Relative Quantification Approach for Studying Protein Abundance of Drug Metabolizing Enzymes in Human Liver Microsomes Using SWATH-MS.

J Proteome Res 16: 4134-4143. DOI: 10.1021/acs.jproteome.7b00505.

Jiang, W., M. H. Guo and X. Hai (2016):

Hepatoprotective and antioxidant effects of lycopene on non-alcoholic fatty liver disease in rat.

World J Gastroenterol 22: 10180-10188. DOI: 10.3748/wjg.v22.i46.10180.

Kanuri, G. and I. Bergheim (2013):

In vitro and in vivo models of non-alcoholic fatty liver disease (NAFLD).

Int J Mol Sci 14: 11963-11980. DOI: 10.3390/ijms140611963.

Keating, S. M., D. Waltemath, M. Konig, F. Zhang, A. Drager, C. Chaouiya, F. T. Bergmann, A. Finney, C. S. Gillespie, T. Helikar, S. Hoops, R. S. Malik-Sheriff, S. L. Moodie, Moraru, II, C. J. Myers, A. Naldi, B. G. Olivier, S. Sahle, J. C. Schaff, L. P. Smith, M. J. Swat, D. Thieffry, L. Watanabe, D. J. Wilkinson, M. L. Blinov, K. Begley, J. R. Faeder, H. F. Gomez, T. M. Hamm, Y. Inagaki, W. Liebermeister, A. L. Lister, D. Lucio, E. Mjolsness, C. J. Proctor, K. Raman, N. Rodriguez, C. A. Shaffer, B. E. Shapiro, J. Stelling, N. Swainston, N. Tanimura, J. Wagner, M. Meier-Schellersheim, H. M. Sauro, B. Palsson, H. Bolouri, H. Kitano, A. Funahashi, H. Hermjakob, J. C. Doyle, M. Hucka and S. L. C. members (2020):

SBML Level 3: an extensible format for the exchange and reuse of biological models.

Mol Syst Biol 16: e9110. DOI: 10.15252/msb.20199110.

Keramida, G., J. Hunter, S. Dizdarevic and A. M. Peters (2016):

Heterogeneity of intrahepatic fat distribution determined by F-18-FDG PET and CT.

Annals of Nuclear Medicine 30: 200-206. DOI: 10.1007/s12149-015-1045-8.

Kietzmann, T. (2017):

Metabolic zonation of the liver: The oxygen gradient revisited.

Redox Biol 11: 622-630. DOI: 10.1016/j.redox.2017.01.012.

Kleeberg, U. and W. Klinger (1982):

Sensitive Formaldehyde Determination with Nashs Reagent and a Tryptophan Reaction.

Journal of Pharmacological Methods 8: 19-31. DOI: Doi 10.1016/0160-5402(82)90004-3.

Kleiner, D. E., E. M. Brunt, M. Van Natta, C. Behling, M. J. Contos, O. W. Cummings, L. D. Ferrell, Y. C. Liu, M. S. Torbenson, A. Unalp-Arida, M. Yeh, A. J. McCullough, A. J. Sanyal and N. Nonalcoholic Steatohepatitis Clinical Research (2005):

Design and validation of a histological scoring system for nonalcoholic fatty liver disease.

Hepatology 41: 1313-1321. DOI: 10.1002/hep.20701.

Kokkinidis, M., N. M. Glykos and V. E. Fadouloglou (2020):

Catalytic activity regulation through post-translational modification: the expanding universe of protein diversity.

Adv Protein Chem Struct Biol 122: 97-125. DOI: 10.1016/bs.apcsb.2020.05.001.

Kolaric, T. O., V. Nincevic, L. Kuna, K. Duspara, K. Bojanic, S. Vukadin, N. Raguz-Lucic, G. Y. Wu and M. Smolic (2021):

Drug-induced Fatty Liver Disease: Pathogenesis and Treatment.

J Clin Transl Hepatol 9: 731-737. DOI: 10.14218/JCTH.2020.00091.

Kolwankar, D., R. Vuppalanchi, B. Ethell, D. R. Jones, S. A. Wrighton, S. D. Hall and N. Chalasani (2007):

Association Between Nonalcoholic Hepatic Steatosis and Hepatic Cytochrome P-450 3A Activity.

Clinical Gastroenterology and Hepatology 5: 388-393. DOI: 10.1016/j.cgh.2006.12.021.

Kostrzewski, T., T. Cornforth, S. A. Snow, L. Ouro-Gnao, C. Rowe, E. M. Large and D. J. Hughes (2017):

Three-dimensional perfused human in vitro model of non-alcoholic fatty liver disease.

World J Gastroenterol 23: 204-215. DOI: 10.3748/wjg.v23.i2.204.

Kruepunga, N., T. B. M. Hakvoort, J. Hikspoors, S. E. Kohler and W. H. Lamers (2019):

Anatomy of rodent and human livers: What are the differences?

Biochim Biophys Acta Mol Basis Dis 1865: 869-878. DOI: 10.1016/j.bbadis.2018.05.019.

Kulkarni, N. M., S. Malampati, M. Y. Mahat, S. Chandrasekaran, J. Raghul, A. A. Khan, U. M. Krishnan and S. Narayanan (2016):

Altered pharmacokinetics of rosiglitazone in a mouse model of non-alcoholic fatty liver disease.

Drug Metab Pers Ther 31: 165-171. DOI: 10.1515/dmpt-2016-0008.

Lambers, L., N. Waschinsky, J. Schleicher, M. König, H.-M. Tautenhahn, M. Albadry, U. Dahmen and T. Ricken (2023):

Quantifying Fat Zonation in Liver Lobules: An IntegratedMultiscale In-silico Model Combining DisturbedMicroperfusion and Fat Metabolism via aContinuum-Biomechanical Bi-scale, Tri-phasic Approach. DOI: https://doi.org/10.21203/rs.3.rs-3348101/v1.

Lambers, L., N. Waschinsky, J. Schleicher, M. König, H. M. Tautenhahn, M. Albadry, U. Dahmen and T. Ricken (2024):

Quantifying fat zonation in liver lobules: an integrated multiscale in silico model combining disturbed microperfusion and fat metabolism via a continuum biomechanical bi-scale, tri-phasic approach.

Biomech Model Mechanobiol 23: 631-653. DOI: 10.1007/s10237-023-01797-0.

Lau, C., B. Kalantari, K. P. Batts, L. D. Ferrell, S. L. Nyberg, R. P. Graham and R. K. Moreira (2021):

The Voronoi theory of the normal liver lobular architecture and its applicability in hepatic zonation.

Sci Rep 11: 9343. DOI: 10.1038/s41598-021-88699-2.

Lerapetritou, M. G., P. G. Georgopoulos, C. M. Roth and L. P. Androulakis (2009):

Tissue-level modeling of xenobiotic metabolism in liver: An emerging tool for enabling clinical translational research.

Clin Transl Sci 2: 228-237. DOI: 10.1111/j.1752-8062.2009.00092.x.

Li, H., J. D. Clarke, A. L. Dzierlenga, J. Bear, M. J. Goedken and N. J. Cherrington (2017):

In vivo cytochrome P450 activity alterations in diabetic nonalcoholic steatohepatitis mice.

Journal of Biochemical and Molecular Toxicology 31: e21840. DOI: 10.1002/jbt.21840.

Lickteig, A. J., C. D. Fisher, L. M. Augustine, L. M. Aleksunes, D. G. Besselsen, A. L. Slitt, J. E. Manautou and N. J. Cherrington (2007):

Efflux transporter expression and acetaminophen metabolite excretion are altered in rodent models of nonalcoholic fatty liver disease.

Drug Metab Dispos 35: 1970-1978. DOI: 10.1124/dmd.107.015107.

Lindros, K. O. (1997):

Zonation of cytochrome P450 expression, drug metabolism and toxicity in liver.

Gen Pharmacol 28: 191-196. DOI: 10.1016/s0306-3623(96)00183-8.

Lonardo, A., S. Bellentani, C. K. Argo, S. Ballestri, C. D. Byrne, S. H. Caldwell, H. Cortez-Pinto, A. Grieco, M. V. Machado, L. Miele and G. Targher (2015):

Epidemiological modifiers of non-alcoholic fatty liver disease: Focus on high-risk groups.

Dig Liver Dis 47: 997-1006. DOI: 10.1016/j.dld.2015.08.004.

Lu, Q., X. Tian, H. Wu, J. Huang, M. Li, Z. Mei, L. Zhou, H. Xie and S. Zheng (2021):

Metabolic Changes of Hepatocytes in NAFLD.

Front Physiol 12: 710420. DOI: 10.3389/fphys.2021.710420.

Macenko, M., M. Niethammer, J. S. Marron, D. Borland, J. T. Woosley, X. Guan, C. Schmitt and N. E. Thomas (2009):

A method for normalizing histology slides for quantitative analysis.

2009 IEEE international symposium on biomedical imaging: from nano to macro, IEEE.

Manco, R. and S. Itzkovitz (2021):

Liver zonation.

J Hepatol 74: 466-468. DOI: 10.1016/j.jhep.2020.09.003.

Marsman, H., T. Matsushita, R. Dierkhising, W. Kremers, C. Rosen, L. Burgart and S. L. Nyberg (2004):

Assessment of donor liver steatosis: pathologist or automated software?

Hum Pathol 35: 430-435. DOI: 10.1016/j.humpath.2003.10.029.

Martignoni, M., G. M. M. Groothuis and R. de Kanter (2006):

Species differences between mouse, rat, dog, monkey and human CYP-mediated drug metabolism, inhibition and induction.

Expert Opinion on Drug Metabolism & Toxicology 2: 875-894. DOI: 10.1517/17425255.2.6.875.

Mashek, D. G. (2020):

Hepatic lipid droplets: A balancing act between energy storage and metabolic dysfunction in NAFLD.

Molecular Metabolism 50. DOI: ARTN 10111510.1016/j.molmet.2020.101115.

Massart, J., K. Begriche, J. H. Hartman and B. Fromenty (2022):

Role of Mitochondrial Cytochrome P450 2E1 in Healthy and Diseased Liver.

Cells 11. DOI: ARTN 28810.3390/cells11020288.

Massart, J., K. Begriche, C. Moreau and B. Fromenty (2017):

Role of nonalcoholic fatty liver disease as risk factor for drug-induced hepatotoxicity.

Journal of clinical and translational research 3: 212. DOI: 10.18053/jctres.03.2017S1.006.

Merrell, M. D. and N. J. Cherrington (2011):

Drug metabolism alterations in nonalcoholic fatty liver disease.

Drug Metab Rev 43: 317-334. DOI: 10.3109/03602532.2011.577781.

Miele, L., A. Liguori, G. Marrone, M. Biolato, C. Araneo, F. G. Vaccaro, A. Gasbarrini and A. Grieco (2017):

Fatty liver and drugs: the two sides of the same coin.

Eur Rev Med Pharmacol Sci 21: 86-94.

Mukaka, M. M. (2012):

Statistics Corner: A guide to appropriate use of Correlation coefficient in medical research.

Malawi Medical Journal 24: 69-71.

Murad, S. (2022):

Research Possibilities in Computational Modeling as a Low Cost Alternative to Traditional Experimental Research.

Higher Education in the Arab World: Research and Development, Springer: 165-172.

Newville, M., T. Stensitzki, D. B. Allen, M. Rawlik, A. Ingargiola and A. Nelson (2016):

LMFIT: Non-linear least-square minimization and curve-fitting for Python.

Astrophysics Source Code Library: ascl: 1606.1014.

NIH. (2022).

How Animals Have Helped Improve Public Health. from https://grants.nih.gov/grants/policy/air/how-animals-help.htm.

Osna, N. A., T. M. Donohue, Jr. and K. K. Kharbanda (2017):

Alcoholic Liver Disease: Pathogenesis and Current Management.

Alcohol Res 38: 147-161.

Paine, M. F., H. L. Hart, S. S. Ludington, R. L. Haining, A. E. Rettie and D. C. Zeldin (2006):

The human intestinal cytochrome P450 "pie".

Drug Metabolism and Disposition 34: 880-886. DOI: 10.1124/dmd.105.008672.

Palek, R., J. Rosendorf, A. Maleckova, L. Vistejnova, K. Bajcurova, H. Mirka, V. Tegl, O. Brzon, A. Kumar, L. Bednar, Z. Tonar, P. Hosek, V. Moulisova, L. Eberlova, V. Treska and V. Liska (2020):

Influence of Mesenchymal Stem Cell Administration on The Outcome of Partial Liver Resection in a Porcine Model of Sinusoidal Obstruction Syndrome.

Anticancer Res 40: 6817-6833. DOI: 10.21873/anticanres.14704.

Pedregosa, F., G. Varoquaux, A. Gramfort, V. Michel, B. Thirion, O. Grisel, M. Blondel, P. Prettenhofer, R. Weiss and V. Dubourg (2011):

Scikit-learn: Machine learning in Python.

the Journal of machine Learning research 12: 2825-2830.

Peleman, C., W. H. De Vos, I. Pintelon, A. Driessen, A. Van Eyck, C. Van Steenkiste, L. Vonghia, J. De Man, B. Y. De Winter, T. Vanden Berghe, S. M. Francque and W. J. Kwanten (2023):

Zonated quantification of immunohistochemistry in normal and steatotic livers.

Virchows Arch 482: 1035-1045. DOI: 10.1007/s00428-023-03496-8.

Pereira, E., R. R. Silvares, E. E. I. Flores, K. L. Rodrigues, I. P. Ramos, I. J. da Silva, M. P. Machado, R. A. Miranda, C. C. Pazos-Moura, C. F. Goncalves-de-Albuquerque, H. C. C. Faria-Neto, E. Tibirica and A. Daliry (2017):

Hepatic microvascular dysfunction and increased advanced glycation end products are components of non-alcoholic fatty liver disease.

PLoS One 12: e0179654. DOI: 10.1371/journal.pone.0179654.

Pohl, R. J. and J. R. Fouts (1980):

A rapid method for assaying the metabolism of 7-ethoxyresorufin by microsomal subcellular fractions.

Anal Biochem 107: 150-155. DOI: 10.1016/0003-2697(80)90505-9.

Ramadori, G. and B. Christ (1999):

Cytokines and the hepatic acute-phase response.

Semin Liver Dis 19: 141-155. DOI: 10.1055/s-2007-1007106.

Rey-Bedon, C., P. Banik, A. Gokaltun, O. Hofheinz, M. L. Yarmush, M. K. Uygun and O. B. Usta (2022):

CYP450 drug inducibility in NAFLD via an in vitro hepatic model: Understanding drug-drug interactions in the fatty liver.

Biomed Pharmacother 146: 112377. DOI: 10.1016/j.biopha.2021.112377.

Ricken, T., D. Werner, H. G. Holzhutter, M. Konig, U. Dahmen and O. Dirsch (2015):

Modeling function-perfusion behavior in liver lobules including tissue, blood, glucose, lactate and glycogen by use of a coupled two-scale PDE-ODE approach.

Biomech Model Mechanobiol 14: 515-536. DOI: 10.1007/s10237-014-0619-z.

Rohan, E., J. Camprova Turjanicova and V. Liska (2021):

Geometrical model of lobular structure and its importance for the liver perfusion analysis.

PLoS One 16: e0260068. DOI: 10.1371/journal.pone.0260068.

Rong, R., Y. Wei, L. Li, T. Wang, H. Zhu, G. Xiao and Y. Wang (2023):

Image-based quantification of histological features as a function of spatial location using the Tissue Positioning System.

EBioMedicine 94.

Santhekadur, P. K., D. P. Kumar and A. J. Sanyal (2018):

Preclinical models of non-alcoholic fatty liver disease.

J Hepatol 68: 230-237. DOI: 10.1016/j.jhep.2017.10.031.

Satapathy, S. K., V. Kuwajima, J. Nadelson, O. Atiq and A. J. Sanyal (2015):

Drug-induced fatty liver disease: An overview of pathogenesis and management.

Ann Hepatol 14: 789-806. DOI: 10.5604/16652681.1171749.

Schälte, Y., F. Fröhlich, P. Stapor, J. Vanhoefer, D. Weindl, P. J. Jost, D. Wang, P. Lakrisenko, E. Raimúndez, P. Dilan, L. Schmiester, P. Städter, L. Contento, S. Merkt, E. Dudkin, S. Grein and J. Hasenauer. (2021).

pyPESTO - Parameter EStimation TOolbox for python (0.2.7). from https://doi.org/10.5281/zenodo.6606687.

Schenk, A., A. Ghallab, U. Hofmann, R. Hassan, M. Schwarz, A. Schuppert, L. O. Schwen, A. Braeuning, D. Teutonico, J. G. Hengstler and L. Kuepfer (2017):

Physiologically-based modelling in mice suggests an aggravated loss of clearance capacity after toxic liver damage.

Sci Rep 7: 6224. DOI: 10.1038/s41598-017-04574-z.

Schmiester, L., Y. Schalte, F. T. Bergmann, T. Camba, E. Dudkin, J. Egert, F. Frohlich, L. Fuhrmann, A. L. Hauber, S. Kemmer, P. Lakrisenko, C. Loos, S. Merkt, W. Muller, D. Pathirana, E. Raimundez, L. Refisch, M. Rosenblatt, P. L. Stapor, P. Stadter, D. Wang, F. G. Wieland, J. R. Banga, J. Timmer, A. F. Villaverde, S. Sahle, C. Kreutz, J. Hasenauer and D. Weindl (2021):

PEtab-Interoperable specification of parameter estimation problems in systems biology.

PLoS Comput Biol 17: e1008646. DOI: 10.1371/journal.pcbi.1008646.

Schwen, L. O., A. Homeyer, M. Schwier, U. Dahmen, O. Dirsch, A. Schenk, L. Kuepfer, T. Preusser and A. Schenk (2016):

Zonated quantification of steatosis in an entire mouse liver.

Comput Biol Med 73: 108-118. DOI: 10.1016/j.compbiomed.2016.04.004.

Seebacher, F., A. Zeigerer, N. Kory and N. Krahmer (2020):

Hepatic lipid droplet homeostasis and fatty liver disease.

Semin Cell Dev Biol 108: 72-81. DOI: 10.1016/j.semcdb.2020.04.011.

Sherlock, S. and J. Dooley (2002):

Diseases of the liver and biliary system.

Osney Mead, Oxford OX2 0EL, UK, Blackwell Science.

Shimada, T., H. Yamazaki, M. Mimura, Y. Inui and F. P. Guengerich (1994):

Interindividual variations in human liver cytochrome P-450 enzymes involved in the oxidation of drugs, carcinogens and toxic chemicals: studies with liver microsomes of 30 Japanese and 30 Caucasians.

J Pharmacol Exp Ther 270: 414-423.

Silva, G. H., G. Hessel, K. I. R. Coelho and C. A. F. Escanhoela (2011):

Steatosis of indeterminate cause in a pediatric group: is it a primary mitochondrial hepatopathy?

Sao Paulo Medical Journal 129: 217-223. DOI: Doi 10.1590/S1516-31802011000400004.

Soret, P. A., J. Magusto, C. Housset and J. Gautheron (2020):

In Vitro and In Vivo Models of Non-Alcoholic Fatty Liver Disease: A Critical Appraisal.

J Clin Med 10. DOI: 10.3390/jcm10010036.

Stärkel, P., C. Sempoux, I. Leclercq, M. Herin, C. Deby, J. P. Desager and Y. Horsmans (2003):

Oxidative stress, KLF6 and transforming growth factor-beta up-regulation differentiate non-alcoholic steatohepatitis progressing to fibrosis from uncomplicated steatosis in rats.

J Hepatol 39: 538-546. DOI: 10.1016/s0168-8278(03)00360-x.

Stefan, N., K. Kantartzis and H. U. Haring (2008):

Causes and metabolic consequences of Fatty liver.

Endocr Rev 29: 939-960. DOI: 10.1210/er.2008-0009.

Steffen, G., L. Lena, M. Luis, F. Julian, R. Tim and K. Matthias (2024):

Simulation of zonation-function relationships in the liver using coupled multiscale models: Application to drug-induced liver injury.

bioRxiv: 2024.2003.2026.586870. DOI: 10.1101/2024.03.26.586870.

Sun, J. (2011):

Induction of fatty liver in Lewis rats using different diets Doctor's Degree of Medicine, University of Duisburg-Essen.

Tachikawa, M., Y. Sumiyoshiya, D. Saigusa, K. Sasaki, M. Watanabe, Y. Uchida and T. Terasaki (2018):

Liver Zonation Index of Drug Transporter and Metabolizing Enzyme Protein Expressions in Mouse Liver Acinus.

Drug Metabolism and Disposition 46: 610-618. DOI: 10.1124/dmd.117.079244.

Tarantino, G., M. N. Di Minno and D. Capone (2009):

Drug-induced liver injury: is it somehow foreseeable?

World J Gastroenterol 15: 2817-2833. DOI: 10.3748/wjg.15.2817.

Teutsch, H. F., D. Schuerfeld and E. Groezinger (1999):

Three-dimensional reconstruction of parenchymal units in the liver of the rat.

Hepatology 29: 494-505. DOI: 10.1002/hep.510290243.

Trefts, E., M. Gannon and D. H. Wasserman (2017):

The liver.

Curr Biol 27: R1147-R1151. DOI: 10.1016/j.cub.2017.09.019.

Turner, P. V., T. Brabb, C. Pekow and M. A. Vasbinder (2011):

Administration of substances to laboratory animals: routes of administration and factors to consider.

J Am Assoc Lab Anim Sci 50: 600-613.

Van Peer, E., E. Verbueken, M. Saad, C. Casteleyn, C. Van Ginneken and S. Van Cruchten (2014):

Ontogeny of CYP3A and P-glycoprotein in the liver and the small intestine of the Gottingen minipig: an immunohistochemical evaluation.

Basic Clin Pharmacol Toxicol 114: 387-394. DOI: 10.1111/bcpt.12173.

van Waterschoot, R. A., A. E. van Herwaarden, J. S. Lagas, R. W. Sparidans, E. Wagenaar, C. M. van der Kruijssen, J. A. Goldstein, D. C. Zeldin, J. H. Beijnen and A. H. Schinkel (2008):

Midazolam metabolism in cytochrome P450 3A knockout mice can be attributed to up-regulated CYP2C enzymes.

Mol Pharmacol 73: 1029-1036. DOI: 10.1124/mol.107.043869.

Vanhoefer, J., M. Matos, D. Pathirana, Y. Schälte and J. Hasenauer (2021):

yaml2sbml: Human-readable and -writable specification of ODE models and their conversion to SBML.

Journal of Open Source Software 6: 3215. DOI: 10.21105/joss.03215.

Vernon, H., C. J. Wehrle, V. S. K. Alia and A. Kasi (2023):

Anatomy, Abdomen and Pelvis: Liver.

StatPearls. Treasure Island (FL) ineligible companies. Disclosure: Chase Wehrle declares no relevant financial relationships with ineligible companies. Disclosure: Valentine Sampson Alia

declares no relevant financial relationships with ineligible companies. Disclosure: Anup Kasi declares no relevant financial relationships with ineligible companies.

Vetelainen, R., A. van Vliet, D. J. Gouma and T. M. van Gulik (2007):

Steatosis as a risk factor in liver surgery.

Annals of Surgery 245: 20-30. DOI: 10.1097/01.sla.0000225113.88433.cf.

Vinod, G. and B. Mahalakshmi (2023):

Rodents in Drug Discovery.

Rodents and Their Role in Ecology, Medicine and Agriculture. S. Mohammad Manjur. Rijeka, IntechOpen: Ch. 5.

Virtanen, P., R. Gommers, T. E. Oliphant, M. Haberland, T. Reddy, D. Cournapeau, E. Burovski, P. Peterson, W. Weckesser, J. Bright, S. J. van der Walt, M. Brett, J. Wilson, K. J. Millman, N. Mayorov, A. R. J. Nelson, E. Jones, R. Kern, E. Larson, C. J. Carey, I. Polat, Y. Feng, E. W. Moore, J. VanderPlas, D. Laxalde, J. Perktold, R. Cimrman, I. Henriksen, E. A. Quintero, C. R. Harris, A. M. Archibald, A. H. Ribeiro, F. Pedregosa, P. van Mulbregt and C. SciPy (2020):

SciPy 1.0: fundamental algorithms for scientific computing in Python.

Nat Methods 17: 261-272. DOI: 10.1038/s41592-019-0686-2.

Vousden, W. D., W. M. Farr and I. Mandel (2016):

Dynamic temperature selection for parallel tempering in Markov chain Monte Carlo simulations.

Monthly Notices of the Royal Astronomical Society 455: 1919-1937. DOI: 10.1093/mnras/stv2422.

Washabau, R. J. (2013):

Chapter 61 - Liver.

Canine and Feline Gastroenterology. R. J. Washabau and M. J. Day. Saint Louis, W.B. Saunders: 849-957.

Wehling, M. (2011):

Drug development in the light of translational science: shine or shade?

Drug Discov Today 16: 1076-1083. DOI: 10.1016/j.drudis.2011.07.008.

Weltman, M. D., G. C. Farrell, P. Hall, M. Ingelman-Sundberg and C. Liddle (1998):

Hepatic cytochrome P450 2E1 is increased in patients with nonalcoholic steatohepatitis.

Hepatology 27: 128-133.

Weltman, M. D., G. C. Farrell and C. Liddle (1996):

Increased hepatocyte CYP2E1 expression in a rat nutritional model of hepatic steatosis with inflammation.

Gastroenterology 111: 1645-1653. DOI: 10.1016/s0016-5085(96)70028-8.

Woolsey, S. J., S. E. Mansell, R. B. Kim, R. G. Tirona and M. D. Beaton (2015):

CYP3A Activity and Expression in Nonalcoholic Fatty Liver Disease.

Drug Metab Dispos 43: 1484-1490. DOI: 10.1124/dmd.115.065979.

Yap, K. K. and G. M. Mitchell (2022):

Chapter One - Recapitulating the liver niche in vitro.

Advances in Stem Cells and their Niches. S. Nilsson, Elsevier. 6: 1-55.

Yersiz, H., C. Lee, F. M. Kaldas, J. C. Hong, A. Rana, G. T. Schnickel, J. A. Wertheim, A. Zarrinpar, V. G. Agopian, J. Gornbein, B. V. Naini, C. R. Lassman, R. W. Busuttil and H. Petrowsky (2013):

Assessment of hepatic steatosis by transplant surgeon and expert pathologist: A prospective, double-blind evaluation of 201 donor livers.

Liver Transplantation 19: 437-449. DOI: 10.1002/lt.23615.

Younossi, Z. M., P. Golabi, J. M. Paik, A. Henry, C. Van Dongen and L. Henry (2023):

The global epidemiology of nonalcoholic fatty liver disease (NAFLD) and nonalcoholic steatohepatitis (NASH): a systematic review.

Hepatology 77: 1335-1347. DOI: 10.1097/HEP.0000000000000004.

Zachary, J. F. and M. D. McGavin (2012):

Pathologic Basis of Veterinary Disease. Elsevier Health Sciences.

Zanger, U. M. and M. Schwab (2013):

Cytochrome P450 enzymes in drug metabolism: regulation of gene expression, enzyme activities, and impact of genetic variation.

Pharmacol Ther 138: 103-141. DOI: 10.1016/j.pharmthera.2012.12.007.

Zhang, L., P. Xu, Y. Cheng, P. Wang, X. Ma, M. Liu, X. Wang and F. Xu (2019):

Diet-induced obese alters the expression and function of hepatic drug-metabolizing enzymes and transporters in rats.

Biochem Pharmacol 164: 368-376. DOI: 10.1016/j.bcp.2019.05.002.

Zhang, X. B., Y. M. Zeng, X. Y. Chen, Y. X. Zhang, J. Z. Ding and C. Xue (2018):

Decreased expression of hepatic cytochrome P450 1A2 (CYP1A2) in a chronic intermittent hypoxia mouse model.

J Thorac Dis 10: 825-834. DOI: 10.21037/jtd.2017.12.106.

Zhong, F., X. Zhou, J. Xu and L. Gao (2020):

Rodent Models of Nonalcoholic Fatty Liver Disease.

Digestion 101: 522-535. DOI: 10.1159/000501851.

9. Appendix

9.1. Supplementary tables

Table S 1. Formulation of a typical and high-fat diet with low levels of methionine and choline. “Reproduced with permission from Springer Nature” (Albadry et al. 2022).

Nutrients	**Standard control diet [%]** 1320 formula, Altromin International	**High fat diet with low methionine [%] (www.ssniff.de)**
Dry matter	88,7	96.8**%**
Crude protein (N x 6.25)	19.2	12.9**%**
Crude fat	4.1	15.1**%**
Sugar/Dextrins	Not available	45.1**%**
Starch	Not available	14.1**%**
N free extracts	55%	57.8**%**
Crude ash	5.9%	5.9**%**
Crude fibre	6.1%	5**%**
Methionine	0.27%	0.14**%**
Lysine	0.81%	1.25**%**
Lys : Met+Cys	Not available	1: 0.28**%**
Met+Cys	Not available	0.35**%**

Table S 2. Compilation of studies investigating the impact of hepatic steatosis on drug metabolism. Those studies were mostly focusing on PK, CYP protein expression level and enzyme activity, but less on zonal distribution of CYP enzymes. “Reproduced with permission from Springer Nature” (Albadry et al. 2022).

Study	species	Model	PK	Activity	IHC	WB	mRNA
Own study (Albadry et al. 2022)	Mouse	MCD+HF diet/4wks, NAFLD	Y	Y	Y	-	-
(Woolsey et al. 2015)	Human	NASH	Y	Y	-	-	Y
(Fisher et al. 2009)	Human	NASH	-	Y	-	Y	Y
(Kolwankar et al. 2007)	Human	NASH	-	Y	-	Y	Y
(Weltman et al. 1998)	Human	NASH	-	-	Y	-	-
(Hata et al. 2010)	Human	Steatosis (Type: NA)	-	-	Y	-	Y
(Bell et al. 2010)	Human	NASH	-	-	-	Y	-
(Aljomah et al. 2015)	Human	NASH	-	-	-	-	Y
(Kulkarni et al. 2016)	Mouse	HF diet+High fructose diet/8wks	Y	-	-	-	-
(Li et al. 2017)	Mouse	MCD dieet/ 4wks	Y	-	-	Y	Y
(Woolsey et al. 2015)	Mouse	HF diet/4wks	-	Y	-	-	Y
(Abdelmegeed et al. 2012)	Mouse	HF diet/ 10 wks	-	Y	-	-	-
(Lickteig et al. 2007)	SD rat	HF diet/ 8wks	Y	-	-	-	-
(Lickteig et al. 2007)	SD rat	MCD-diet/8wks	Y	-	-	-	-
(Bang et al. 2019)	SD rat	1% orotic acid-diet (OA)/ 4-5wks	Y	-	-	Y	-
(Zhang et al. 2019)	SD rat	HF diet	-	Y	-	Y	Y
(Stärkel et al. 2003)	Wi Rat	MCD/ 2-6wk	-	Y	-	Y	-
(Stärkel et al. 2003)	Wi Rat	5% OA/ 2-6wk	-	y	-	Y	-
(Weltman et al. 1996)	Wi Rat	MCD-diet/ 13wks	-	Y	Y	-	Y
(Jiang et al. 2016)	Wi Rat	HF-diet/ 14wk	-	-	Y	-	-
(Woolsey et al. 2015)	human hepatoma cells	*in vitro* cellular steatosis	-	Y	-	-	Y
(Donato et al. 2006)	Human hepatocytes	*in vitro* cellular steatosis	-	Y	-	-	Y
(Donato et al. 2007)	Human hepatocytes	*in vitro* cellular steatosis	-	Y	-	-	Y
(Kostrzewski et al. 2017)	Human hepatocytes	*in vitro* cellular steatosis	-	Y	-	-	Y
(Rey-Bedon et al. 2022)	human hepatocytes	*in vitro* cellular steatosis	-	-	-	-	Y

Table S 3. Contradictory results regarding the impact of hepatic steatosis on expression and activity of selected CYP enzymes. (IHC=H, Western Blot = W, mRNA expression= m, Activity=A; pk=pharmacokinetics; blue color = ↓; light red color = ↑; yellow color= no difference). “Reproduced with permission from Springer Nature” (Albadry et al. 2022).

Study	species	Model	CYP3A	CYP1A	CYP3A4	CYP1A2	CYP2D6	CYP2E1	2A6	2A1	2B6	2B1	2C9	2C19	3A1	3A2	2C29	2C11	3A5	2D22	4A	4A1	7A1
Own study	Mouse	MCD+HF diet	↓ A	↓ A	↓ Pk No diff H	↓ Pk No diff H	No diff Pk, H	↑A No diff H	-	-	-	-	-	-	-	-	-	-	-	-	-		-
(Fisher et al. 2009)	Human	NASH	-	-	↓ A, m	↓ W, A, m	↓ W, m	↓ W, m	↑ W, A	-	↑ W	-	↑ W, A	↓ A,m	-	-	-	-	-	-	-		-
Weltman et al. 1998)	Human	NASH	-	-	↓ H	-	-	↑ H	-	-	-	-	-	-	-	-	-	-	-	-	-		-
(Kolwankar et al. 2007)	Human	NASH	↓A, No diff in m, W	-	↓A, No diff in m W	-	-	-	-	-	-	-	-	-	-	-	-	-	-	-	-		-
(Woolsey et al. 2015)	Human	NASH	-	-	↓ A, m, Pk	-	-	↑ m	-	-	-	-	-	-	-	-	-	-	-	-	-		-
(Aljomah et al. 2015)	Human	NASH	-	-	-	-	-	↑ m	-	-	-	-	-	-	-	-	-	-	-	-	-		-
(Bell et al. 2010)	Human	NASH	-	-	↓ H	-	-	↑ H	-	-	-	-	-	-	-	-	-	-	↓ H	-	-		-
(Hata et al. 2010)	Human	Steatosis	-	-	↓ m, H	-	-	↑ m, H	-	-	-	-	-	-	-	-	-	-	-	-	-		-

(Woolsey et al. 2015)	Mouse	HF diet	-	-	↓ A,m	-	-	↑ m	-	-	-	-	-	-	-	-	-	-	-	-	-		-
(Abdelmegeed et al. 2012)	Mouse	HF diet	-	-	-	-	-	↑ A	-	-	-	-	-	-	-	-	-	-	-	-	-		-
(Li et al. 2017)	Mouse	MCD diet	↓ W,M	-	No diff pk	↓ W, m,pk	No diff pk	-	-	-	-	-	No diff pk	No diff pk	-	-	↓ W, m	-	-	↓ W, m	-		-
(Zhang et al. 2019)	SD rat	HF diet	-	-	-	↓ W, A, m	-	No diff W, A	-	-	-	↓ A, m	-	-	↓ m, A no diff W	no diff W, A	-	↓ W, A, m	-	-	-	↓ A, m	-
(Bang et al. 2019)	SD rat	1% OA diet, Oral metoprolol	-	-	-	-	↓ W, Pk	-	-	-	-	-	-	-	-	-	-	-	-	-	-		-
(Bang et al. 2019)	SD rat	1% OA diet, i.v metoprolol	-	-	-	-	↓W, No diff. Pk	-	-	-	-	-	-	-	-	-	-	-	-	-	-		-
(Stärkel et al. 2003)	Wi Rat	MCD diet	↓ A, No diff. W	-	-	-	-	↓ A, m	-	-	-	-	-	-	-	-	-	-	-	-	↓ A, W		-
(Stärkel et al. 2003)	Wi Rat	5% OA diet	↓ A, ↑ W	-	-	-	-	↑ W,A	-	-	-	-	-	-	-	-	-	-	-	-	No diff		-
(Weltman et al. 1996)	Wi Rat	MCD diet	-	-	-	-	-	↑ A, m, H	-	↓ A	-	-	-	-	-	↓A	-	↓A	-	-	-		-
(Jiang et al. 2016)	Wi Rat	HFD diet	-	-	-	-	-	↑H	-	-	-	-	-	-	-	-	-	-	-	-	-		-

(Donato et al. 2006)	Human hepatocytes	*in vitro* cellular steatosis	-	-	↓ A, m	↓ A, m	↓ A, m	↓ A, m	↓ A, m	-	↓ A, m	-	↓ A, m	-	-	-	-	-	-	-	-	-	-
(Donato et al. 2007)	Human hepatocytes	*in vitro* cellular steatosis	-	-	↓ A,m	↓ A, m	-	↓ A, m	-	-	-	-	↓ A, m	-	-	-	-	-	-	-	-	-	-
(Kostrzewski et al. 2017)	Human hepatocytes	*in vitro* cellular steatosis	-	-	↓ A, m	No diff	No diff	↑ A, m	-	-	-	-	↓ A, m	-	-	-	-	-	-	-	-	-	↑ A, m
(Woolsey et al. 2015)	human hepatoma	*in vitro* cellular steatosis	-	-	↓ A, m	-	-	↑ m	-	-	-	-	-	-	-	-	-	-	-	-	-	-	-
(Rey-Bedon et al. 2022)	human hepatocytes	*in vitro* cellular steatosis	-	↓ m	-	-	-	↑ m	-	-	↑ m	-	No diff m	-	-	-	-	-	-	-	-	-	-

Table S 4. Lack of characterization of steatosis in previous drug metabolism studies (NASH= Nonalcoholic steatohepatitis; HF= High fat; MCD= Methionine choline deficient; OA= Orotic acid). “Reproduced with permission from Springer Nature” (Albadry et al. 2022).

Study	species	Model	severity	pattern	zonation	Drug Metabolism Assay
Own Study	Mouse	MCD+HF diet	moderate	Micro and Macro	periportal	PK, IHC, Activity
(Weltman et al. 1998)	Human	NASH	severe	Macro	diffuse	IHC
(Fisher et al. 2009)	Human	NASH	severe	-	-	WB, Activity, mRNA expression
(Kolwankar et al. 2007)	Human	NASH	-	Macro	-	WB, Activity, mRNA expression
(Woolsey et al. 2015)	Human	NASH	-	-	-	PK, Activity, mRNA expression
(Aljomah et al. 2015)	Human	NASH	-	-	-	mRNA expression
(Bell et al. 2010)	Human	NASH	-	-	-	IHC
(Hata et al. 2010)	Human	Steatosis	-	-	-	IHC, mRNA expression
(Woolsey et al. 2015)	Bl6 Mouse	HF diet	-	-	-	Activity, mRNA expression
(Abdelmegeed et al. 2012)	Wild type Mouse	HF diet	-	micro- and macro	-	Activity
(Kulkarni et al. 2016)	Bl6 Mouse	HF diet+High fructose diet	-	Micro	-	PK
(Li et al. 2017)	Leptin deficient ob/ob Mouse	MCD/4wks	Severe	Macro	-	PK, WB, mRNA
(Lickteig et al. 2007)	SD rat	HF diet	mild	Micro?	Periportal?	Pk
(Lickteig et al. 2007)	SD rat	MCD diet	severe	Macro?	Diffuse?	PK
(Bang et al. 2019)	SD rat	1% OA diet	severe	-	-	PK, WB
(Zhang et al. 2019)	SD rat	HF diet	-	-	-	WB, Activity, mRNA expression
(Weltman et al. 1996)	Wi Rat	MCD diet	severe	macro	diffuse	IHC, Activity, mRNA expression
(Jiang et al. 2016)	Wi Rat	HF diet	-	macro	PC	IHC
(Stärkel et al. 2003)	Wi Rat	MCD diet	severe	macro	2wks diffuse 6wks pericentral	WB, Activity
(Stärkel et al. 2003)	Wi Rat	5% OA diet	severe	micro	2wks pericentral 6wks diffuse	WB, Activity, mRNA expression

Table S 5. Additional parameters of pharmacokinetic study (a = significance difference between Control vs. 2Wks HF-diet; b = significance difference between Control vs. 4Wks HF-diet; c = significance difference between 2Wks HF-diet vs. 4Wks HF-diet HF-diet). “Reproduced with permission from Springer Nature” (Albadry et al. 2022).

Group		Control	2 Wks MCD+HFD	4 Wks MCD+HFD
Midazolam	AUC (hr·ng/mL)	38.38±28.32	37,80±13.36	76,47±25.07*c
	t1/2 (hr)	0.529±0.175	0.919±0.250	1.096±0.584
	Cmax (ng/ml)	59.05±38.42	36.04±16.53	75.29±40.82
	Time of Cmax (hr)	0.315±0.104	0.548±0.149	0.653±0.348
Caffeine	AUC (hr·ng/mL)	1999±350.4	1119±219.4**a	2434±306.6****c
	t1/2 (hr)	1.501±0.307	0.8215±0.383*a	1.156±0.206
	Cmax (ng/ml)	1165±227.2	1326±504.7	1833±547.4
	Time of Cmax (hr)	0.894±0.83	0.489±0.228*a	0.689±0.123
Codeine	AUC (hr·ng/mL)	155.1±10.39	144.1±26.30	190.1±21.11**c
	t1/2 (hr)	0.517±0.064	0.479±0.031	0.579±0.054**c
	Cmax (ng/ml)	254.9±37.12	251.8±35.69	276.2±29.97
	Time of Cmax (hr)	0.308±0.038	0.285±0.019	0.345±0.032

Table S 6. Overview of relative CYP zonal expression. “Reproduced from Frontiers in Pharmacology” (Albadry et al. 2024).

Species	Subject	GS	CYP1A2	CYP2D6	CYP2E1	CYP3A4
Mouse	MNT-021	11.55	58.2	81.48	66.12	52.92
Mouse	MNT-022	12.32	57.47	89.12	67.25	51.58
Mouse	MNT-023	13.69	67.92	85.81	64.09	58.64
Mouse	MNT-024	10.65	52.95	68.41	60.53	66.21
Mouse	MNT-025	14.06	61.95	90.60	62.13	47.94
Mouse	MNT-026	7.05	61.28	74.43	47.45	63.52
Rat	NOR-021	6.23	29.25	93.71	59.84	47.09
Rat	NOR-022	6.79	33.61	78.80	59.81	33.69
Rat	NOR-023	8.12	41.21	97.55	72.60	72.25
Rat	NOR-024	6.81	30.99	95.00	69.50	53.21
Rat	NOR-025	6.73	24.99	95.54	57.81	84.50
Rat	NOR-026	9.64	34.92	91.78	72.91	62.79
Pig	SSES2021/10	4.94	86.44	87.97	60.18	91.56
Pig	SSES2021/12	4.47	85.07	87.08	55.13	88.24
Pig	SSES2021/14	4.99	68.01	92.23	44.55	88.82
Pig	SSES2021/9	8.30	89.02	90.06	68.51	93.99
Pig	VS11 3/8/21	6.71	84.12	91.28	49.70	91.18
Pig	VS12 3/8/21	3.86	77.90	88.06	58.01	89.83
Human	UKJ-19-026	4.12	33.31	89.15	70.02	54.69
Human	UKJ-19-036	10.04	63.14	90.19	82.80	59.94
Human	UKJ-19-033	10.49	61.43	83.52	72.36	38.45
Human	UKJ-19-049	8.58	50.80	96.31	83.18	59.20
Human	UKJ-19-041	10.21	65.39	87.76	64.70	56.14
Human	UKJ-19-010	x	56.43	x	60.03	39.11

Table S 7. Overview of statistical analysis of relative CYP zonal expression (mean ± sd). “Reproduced from Frontiers in Pharmacology” (Albadry et al. 2024).

Species	GS	CYP1A2	CYP2D6	CYP2E1	CYP3A4
Mouse	11.55 ± 2.55	52.96 ± 5.05	81.64 ± 8.73	61.26 ± 7.2	56.8 ± 7.19
Rat	7.39 ± 1.27	32.5 ± 5.52	92.06 ± 6.78	65.41 ± 7	58.92 ± 18.2
Pig	5.55 ± 1.65	81.75 ± 7.68	89.45 ± 2.06	56.01 ± 8.36	90.6 ± 2.1
Human	8.69 ± 2.66	55.08 ± 11.88	89.39 ± 4.63	72.18 ± 7.4	51.26 ± 9.86

Table S 8. Overview of geometric parameters between species. “Reproduced from Frontiers in Pharmacology” (Albadry et al. 2024).

Species	Parameter	n	mean	sd	se	median	min	max	q1	q3	unit
mouse	perimeter	1530	2233	1397	57	1939	157	16155	1436	2636	µm
rat	perimeter	669	2734	2052	106	2345	116	20607	1534	3407	µm
pig	perimeter	698	3562	1823	135	3561	157	11024	2403	4695	µm
human	perimeter	1074	3966	3200	121	3365	157	23206	1841	5091	µm
mouse	area	1530	299281	360094	7651	192697	1269	4462695	110097	350281	μm^2
rat	area	669	467614	729369	18079	266095	846	9373817	121837	553765	μm^2
pig	area	698	718451	572536	27194	637528	1269	3788785	303006	1008009	μm^2
human	area	1074	966234	1357480	29484	530075	1269	10652257	157796	1174054	μm^2
mouse	compactness	1530	0.64	0.10	0.02	0.65	0.19	0.85	0.59	0.70	-
rat	compactness	669	0.62	0.11	0.02	0.63	0.15	0.86	0.56	0.69	-
pig	compactness	698	0.61	0.10	0.02	0.62	0.20	0.81	0.55	0.68	-
human	compactness	1074	0.59	0.12	0.02	0.61	0.18	0.88	0.52	0.68	-
mouse	minimum_bounding_radius	1530	375	216	10	330	33	2068	249	442	µm
rat	minimum_bounding_radius	669	451	299	17	401	21	2488	263	563	µm
pig	minimum_bounding_radius	698	583	285	22	581	33	1737	405	770	µm
human	minimum_bounding_radius	1074	637	473	19	559	33	3889	309	830	µm

Table S 9. Overview of required lobules to determine geometric parameters in different species (with 95% confidence and a 20% margin of error). “Reproduced from Frontiers in Pharmacology” (Albadry et al. 2024).

species	perimeter	area (µm2)	compactness	minimum_bounding_radius (µm)
mouse	31.9 ± 11.5	82.0 ± 20.9	2.2 ± 1.1	27.8 ± 7.5
rat	34.4 ± 10.3	66.4 ± 9.2	2.7 ± 1.5	29.6 ± 8.9
pig	21.7 ± 7.3	44.5 ± 14.1	2.4 ± 0.8	20.0 ± 6.7
human	42.5 ± 29.4	82.4 ± 47.2	3.8 ± 2.9	37.6 ± 26.9

Table S 10. Overview of required lobules to determine geometric parameters in different subjects. "Reproduced from Frontiers in Pharmacology" (Albadry et al. 2024).

species	subject	parameter	unit	mean	sd	n	n0.05	n0.1	n0.15	n0.2	n 0.25	n0.3	n0.35
human	UKJ-19-010_Human	perimeter	µm	3741	2894	196	161.6	105.8	67.2	44.4	31.0	22.6	17.1
human	UKJ-19-026_Human	perimeter	µm	4000	2142	154	114.1	64.2	37.2	23.4	15.8	11.3	8.5
human	UKJ-19-033_Human	perimeter	µm	4017	3076	134	116.7	84.0	57.3	39.6	28.4	21.1	16.2
human	UKJ-19-036_Human	perimeter	µm	4940	4560	107	98.9	80.6	61.6	46.4	35.2	27.1	21.4
human	UKJ-19-041_Human	perimeter	µm	3873	3429	326	256.6	156.5	94.9	61.2	42.0	30.3	22.9
human	UKJ-19-049_Human	perimeter	µm	3701	2760	157	132.6	90.5	59.2	39.9	28.1	20.6	15.7
pig	SSES202110	perimeter	µm	3440	1811	180	126.5	66.9	37.5	23.2	15.6	11.1	8.3
pig	SSES202112	perimeter	µm	3418	1787	193	132.3	68.0	37.6	23.1	15.5	11.0	8.2
pig	SSES202114	perimeter	µm	3779	1862	219	138.0	65.4	34.9	21.1	14.0	9.9	7.4
pig	SSES20219	perimeter	µm	3584	1784	106	82.9	50.1	30.2	19.4	13.3	9.6	7.2
rat	NOR-021	perimeter	µm	2910	1612	96	79.8	52.9	33.9	22.5	15.8	11.5	8.7
rat	NOR-022	perimeter	µm	2636	2241	94	86.7	70.2	53.4	39.9	30.2	23.2	18.3
rat	NOR-023	perimeter	µm	2734	2266	92	84.6	68.2	51.6	38.4	28.9	22.2	17.5
rat	NOR-024	perimeter	µm	2890	2822	116	107.5	88.1	67.7	51.2	38.9	30.1	23.8
rat	NOR-025	perimeter	µm	2840	1808	115	97.1	66.1	43.2	29.1	20.5	15.0	11.4
rat	NOR-026	perimeter	µm	2493	1402	156	118.1	68.3	40.1	25.4	17.3	12.4	9.3
mouse	MNT-021	perimeter	µm	2273	1371	307	198.2	96.1	51.7	31.4	20.9	14.8	11.0
mouse	MNT-022	perimeter	µm	2072	1026	313	171.0	72.4	36.9	21.9	14.4	10.1	7.5
mouse	MNT-023	perimeter	µm	2243	1402	265	183.8	95.8	53.2	32.8	22.0	15.7	11.7
mouse	MNT-024	perimeter	µm	2276	1710	212	170.4	107.2	66.2	43.2	29.8	21.6	16.3
mouse	MNT-025	perimeter	µm	2089	1131	275	170.7	79.8	42.3	25.5	16.9	12.0	8.9
mouse	MNT-026	perimeter	µm	2645	1859	158	130.8	86.2	55.0	36.5	25.5	18.6	14.1
human	UKJ-19-010_Human	area	µm²	837915	1264922	196	185.6	160.1	130.3	103.4	81.7	65.0	52.4
human	UKJ-19-026_Human	area	µm²	878636	754435	154	135.6	99.8	69.3	48.5	35.0	26.1	20.1
human	UKJ-19-033_Human	area	µm²	976494	1374596	134	128.4	113.9	96.0	78.6	63.8	51.9	42.5

human	UKJ-19-036_Human	area	µm²	1656519	2217903	107	103.0	92.6	79.3	66.0	54.3	44.6	36.9
human	UKJ-19-041_Human	area	µm²	942527	1350411	326	295.5	230.7	168.9	122.9	91.0	69.1	53.8
human	UKJ-19-049_Human	area	µm²	782376	954124	157	146.9	123.2	97.0	74.8	57.8	45.2	36.0
pig	SSES202110	area	µm²	664093	546665	180	153.5	106.4	70.4	47.8	33.8	24.9	19.0
pig	SSES202112	area	µm²	679547	540088	193	161.0	107.5	69.2	46.2	32.3	23.7	18.0
pig	SSES202114	area	µm²	808088	609002	219	175.1	109.3	67.2	43.7	30.1	21.8	16.5
pig	SSES20219	area	µm²	696395	573430	106	96.2	75.3	55.3	40.3	29.9	22.7	17.7
rat	NOR-021	area	µm²	506794	562745	96	91.4	79.8	65.9	53.0	42.4	34.0	27.6
rat	NOR-022	area	µm²	460569	1007005	94	92.8	89.4	84.3	78.0	71.2	64.4	57.8
rat	NOR-023	area	µm²	507442	925985	92	90.4	85.8	79.2	71.4	63.5	55.9	48.9
rat	NOR-024	area	µm²	531143	903934	116	113.1	105.0	94.0	81.9	70.2	59.8	50.9
rat	NOR-025	area	µm²	478036	566090	115	109.2	94.8	77.7	62.0	49.3	39.4	31.8
rat	NOR-026	area	µm²	369337	333639	156	138.7	104.2	73.6	52.2	38.0	28.5	22.0
mouse	MNT-021	area	µm²	301442	335951	307	264.5	186.8	125.4	85.9	61.1	45.2	34.6
mouse	MNT-022	area	µm²	250421	222950	313	249.0	154.3	94.5	61.2	42.2	30.5	23.0
mouse	MNT-023	area	µm²	299576	373616	265	238.6	183.6	132.6	95.5	70.3	53.1	41.2
mouse	MNT-024	area	µm²	325437	468968	212	198.8	167.5	132.7	102.8	79.7	62.5	49.8
mouse	MNT-025	area	µm²	262029	262374	275	233.3	160.4	105.5	71.3	50.3	37.0	28.2
mouse	MNT-026	area	µm²	421125	515680	158	147.9	124.0	97.7	75.3	58.2	45.6	36.2
human	UKJ-19-010_Human	compactness	-	0.60	0.12	196	44.5	13.4	6.2	3.5	2.3	1.6	1.2
human	UKJ-19-026_Human	compactness	-	0.59	0.10	154	33.2	9.9	4.6	2.6	1.7	1.2	0.9
human	UKJ-19-033_Human	compactness	-	0.59	0.11	134	38.1	12.1	5.7	3.2	2.1	1.5	1.1
human	UKJ-19-036_Human	compactness	-	0.59	0.13	107	43.4	15.6	7.6	4.4	2.8	2.0	1.5
human	UKJ-19-041_Human	compactness	-	0.59	0.13	326	64.1	18.8	8.6	4.9	3.2	2.2	1.6
human	UKJ-19-049_Human	compactness	-	0.58	0.13	157	49.3	16.1	7.6	4.4	2.8	2.0	1.5

pig	SSES2021 10	compactness	-	0.61	0.10	180	35.5	10.4	4.8	2.7	1.8	1.2	0.9
pig	SSES2021 12	compactness	-	0.62	0.10	193	30.8	8.8	4.0	2.3	1.5	1.0	0.7
pig	SSES2021 14	compactness	-	0.62	0.09	219	30.8	8.6	3.9	2.2	1.4	1.0	0.7
pig	SSES2021 9	compactness	-	0.61	0.10	106	28.0	8.7	4.1	2.3	1.5	1.0	0.8
rat	NOR-021	compactness	-	0.62	0.09	96	25.1	7.8	3.6	2.1	1.3	0.9	0.7
rat	NOR-022	compactness	-	0.60	0.11	94	33.4	11.4	5.4	3.1	2.0	1.4	1.0
rat	NOR-023	compactness	-	0.62	0.10	92	28.4	9.2	4.3	2.5	1.6	1.1	0.8
rat	NOR-024	compactness	-	0.62	0.12	116	37.6	12.4	5.9	3.4	2.2	1.5	1.1
rat	NOR-025	compactness	-	0.61	0.10	115	29.0	8.9	4.2	2.4	1.5	1.1	0.8
rat	NOR-026	compactness	-	0.63	0.10	156	33.2	9.9	4.5	2.6	1.7	1.2	0.9
mouse	MNT-021	compactness	-	0.63	0.10	307	35.4	9.7	4.4	2.5	1.6	1.1	0.8
mouse	MNT-022	compactness	-	0.64	0.09	313	26.6	7.1	3.2	1.8	1.2	0.8	0.6
mouse	MNT-023	compactness	-	0.64	0.10	265	31.1	8.5	3.9	2.2	1.4	1.0	0.7
mouse	MNT-024	compactness	-	0.64	0.10	212	31.9	9.0	4.1	2.3	1.5	1.0	0.8
mouse	MNT-025	compactness	-	0.64	0.09	275	28.6	7.8	3.5	2.0	1.3	0.9	0.7
mouse	MNT-026	compactness	-	0.63	0.11	158	34.5	10.3	4.8	2.7	1.7	1.2	0.9
human	UKJ-19-010_Human	minimum_bounding_radius	µm	609	428	196	155.7	96.2	58.8	38.1	26.2	19.0	14.3
human	UKJ-19-026_Human	minimum_bounding_radius	µm	652	334	154	111.3	60.8	34.6	21.6	14.6	10.4	7.8
human	UKJ-19-033_Human	minimum_bounding_radius	µm	655	456	134	113.6	78.0	51.2	34.6	24.4	18.0	13.7
human	UKJ-19-036_Human	minimum_bounding_radius	µm	765	662	107	97.9	78.0	58.2	43.0	32.2	24.6	19.3
human	UKJ-19-041_Human	minimum_bounding_radius	µm	619	513	326	248.9	145.6	86.1	54.8	37.3	26.8	20.2
human	UKJ-19-049_Human	minimum_bounding_radius	µm	588	394	157	127.9	82.2	51.5	33.9	23.5	17.1	12.9
pig	SSES2021 10	minimum_bounding_radius	µm	557	280	180	123.0	63.1	34.8	21.4	14.3	10.2	7.6
pig	SSES2021 12	minimum_bounding_radius	µm	560	278	193	128.0	63.6	34.6	21.1	14.1	10.0	7.5
pig	SSES2021 14	minimum_bounding_radius	µm	620	293	219	133.7	61.7	32.5	19.6	12.9	9.1	6.8
pig	SSES2021 9	minimum_bounding_radius	µm	594	280	106	80.9	47.3	28.0	17.8	12.1	8.7	6.6
rat	NOR-021	minimum_bounding_radius	µm	486	255	96	78.2	50.3	31.6	20.7	14.4	10.5	7.9
rat	NOR-022	minimum_bounding_radius	µm	433	320	94	84.5	64.9	46.7	33.6	24.7	18.6	14.5
rat	NOR-023	minimum_bounding_radius	µm	446	329	92	82.9	63.9	46.2	33.3	24.5	18.5	14.4

rat	NOR-024	minimum_bounding_radius	µm	471	391	116	104.6	80.7	58.5	42.2	31.1	23.5	18.3
rat	NOR-025	minimum_bounding_radius	µm	467	270	115	94.0	60.7	38.2	25.1	17.5	12.7	9.6
rat	NOR-026	minimum_bounding_radius	µm	415	217	156	113.8	62.9	36.0	22.5	15.2	10.9	8.1
mouse	MNT-021	minimum_bounding_radius	µm	380	210	307	185.6	84.9	44.6	26.8	17.7	12.5	9.3
mouse	MNT-022	minimum_bounding_radius	µm	351	168	313	165.3	68.4	34.6	20.5	13.4	9.4	7.0
mouse	MNT-023	minimum_bounding_radius	µm	380	218	265	173.9	85.6	46.4	28.2	18.8	13.3	9.9
mouse	MNT-024	minimum_bounding_radius	µm	378	246	212	159.8	92.0	53.9	34.1	23.2	16.6	12.5
mouse	MNT-025	minimum_bounding_radius	µm	352	184	275	166.3	76.1	40.0	24.0	15.9	11.2	8.3
mouse	MNT-026	minimum_bounding_radius	µm	437	288	158	127.8	81.2	50.5	33.0	22.9	16.6	12.6

Table S 11. Overview of required lobules to determine relative CYPs expression in different species (with 95% confidence and a 20% margin of error). “Reproduced from Frontiers in Pharmacology” (Albadry et al. 2024).

species	HE	GS	CYP1A2	CYP2D6	CYP2E1
mouse	2.5 ± 1.5	20.1 ± 15.8	5.9 ± 2.0	2.0 ± 0.4	5.9 ± 1.6
rat	8.1 ± 7.9	36.5 ± 9.5	8.9 ± 3.5	5.6 ± 1.1	7.1 ± 3.0
pig	12.3 ± 8.1	28.9 ± 5.6	9.0 ± 4.7	7.3 ± 4.5	13.9 ± 3.5
human	28.3 ± 20.0	42.1 ± 10.5	35.1 ± 16.4	16.8 ± 11.6	27.2 ± 22.1

9.2. Supplementary figures

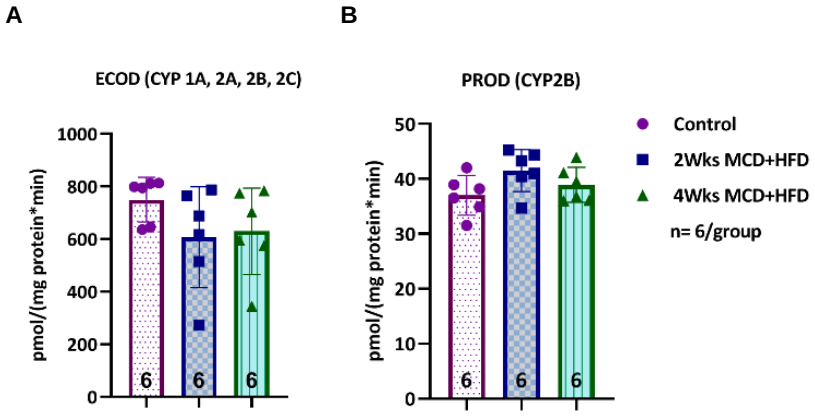

Figure S 1. CYP activity. (A) Using the ECOD assay covering the activity of CYP1A, CYP2A, CYP2B, and CYP2C, no differences between groups were detected; (B) The PROD assay covering the activity of CYP2B did not show any differences between the three groups (sample size of each group displayed in the bottom of the bar). “Reproduced with permission from Springer Nature” (Albadry et al. 2022).

We did not find a correlation between steatosis severity (lipid droplet, micro- or macrovesicular steatosis) and CYP2B Activity (PROD-model reaction), respectively, the results of the ECOD assay covering the combined activity of CYP1A, 2A, 2B, and 2C (Figure S 2).

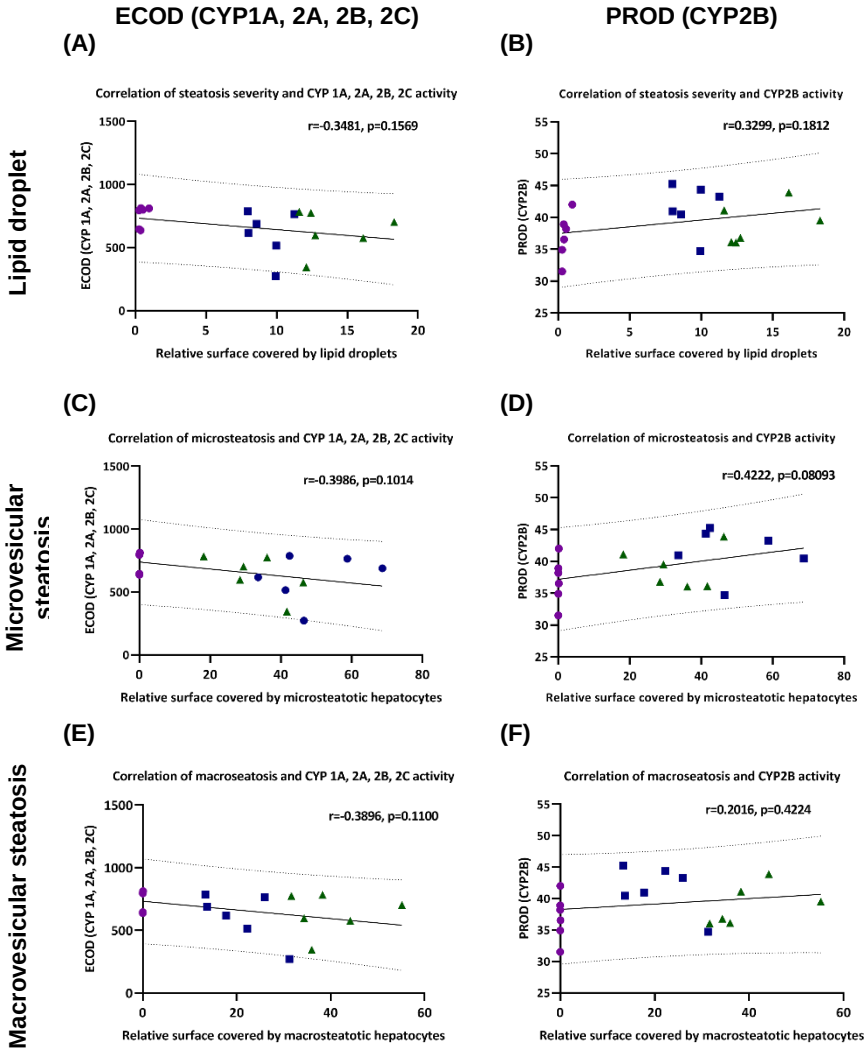

Figure S 2. Correlation analysis between steatosis severity (lipid droplet analysis, micro-and macro-vesicular steatosis) and CYP activity; No correlation between (A, B) lipid droplet analysis, (B, C) microvesicular steatosis, and (C, D) macrovesicular steatosis and results of ECOD-model reaction determining CYP 1A, 2A, 2B,2C activity, respectively PROD-model reaction covering CYP2B. Control as magenta circles, two weeks HF-diet as blue squares, four weeks HF-diet as green triangles. “Reproduced with permission from Springer Nature” (Albadry et al. 2022).

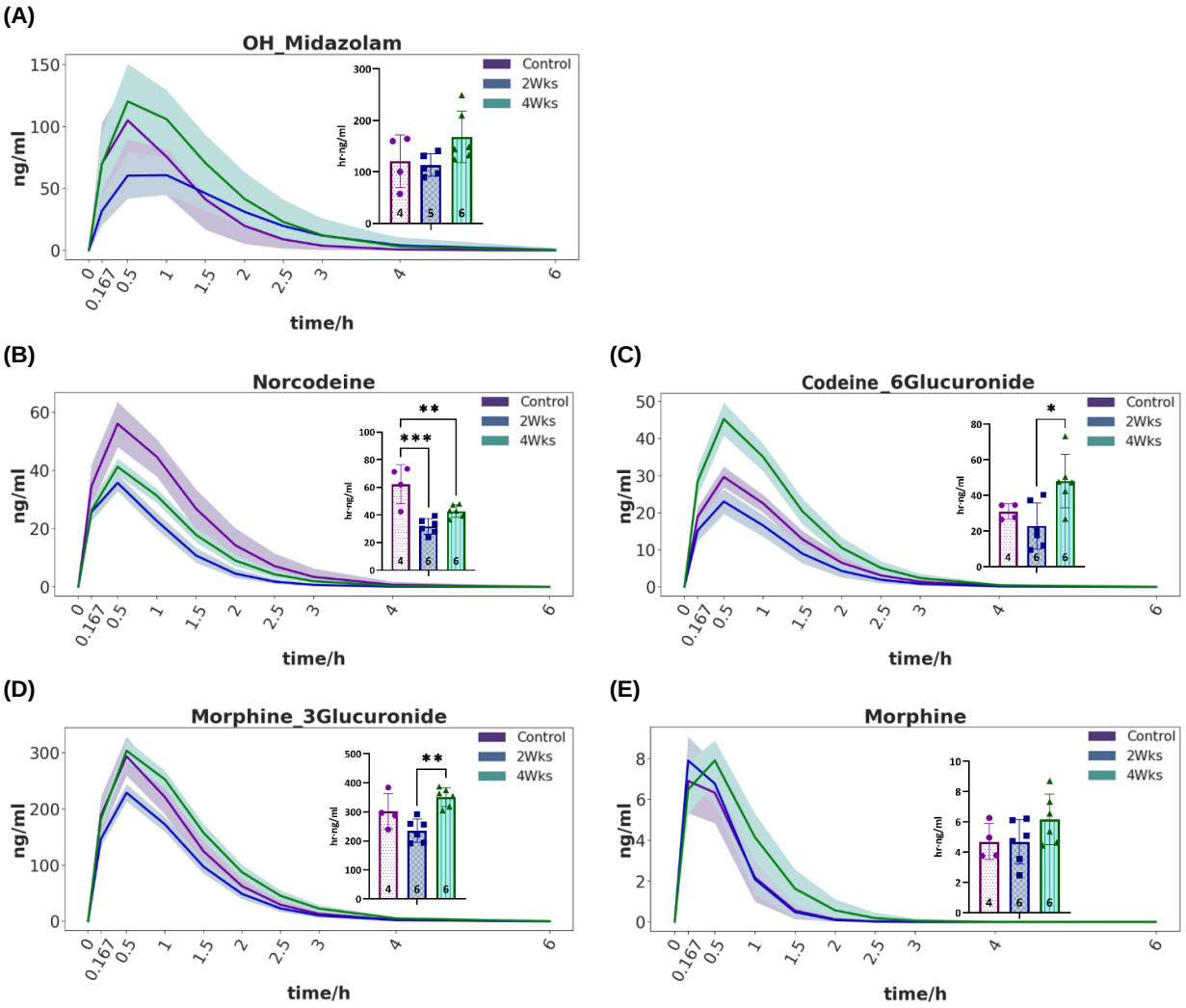

Figure S 3. Drug elimination curves of the test drugs metabolites and resulting AUC. (A) 1-OH-Midazolam; (B) Norcodeine; (C) Codeine-6-Glucuronide; (D) Morphine-3-Glucuronide; (E) Morphine. (*significance level < 0.05, **significance level < 0.03, *** significance level < 0.0021, **** significance level < 0.0001). sample size of each group displayed in the bottom of the bar. Solid lines are mean, shaded areas correspond to the 95% credibility interval from the Bayesian analysis. “Reproduced with permission from Springer Nature” (Albadry et al. 2022).

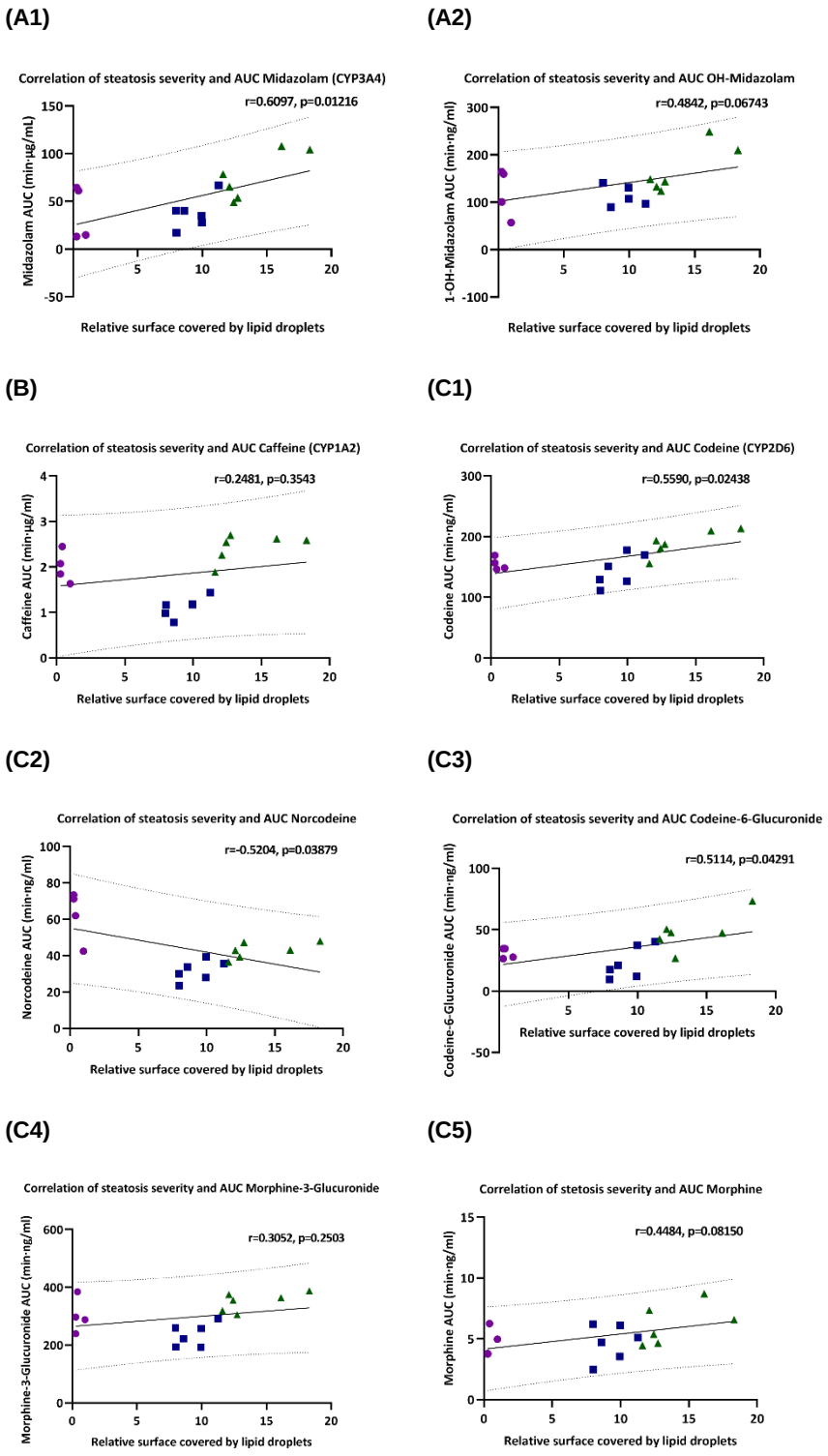

Figure S 4. (A1-C5) Linear correlation between steatosis severity (lipid droplet analysis) and AUC of the test drugs and their metabolites. Moderate positive correlation between lipid droplet analysis and AUC of midazolam (CYP3A4), respectively codeine (CYP2D6), norcodeine and codeine-6-glucuronide. Correlation coefficient and p-value indicated in the figure. Control as magenta circles, two weeks HF-diet as blue squares, four weeks HF-diet as green triangles. “Reproduced with permission from Springer Nature” (Albadry et al. 2022).

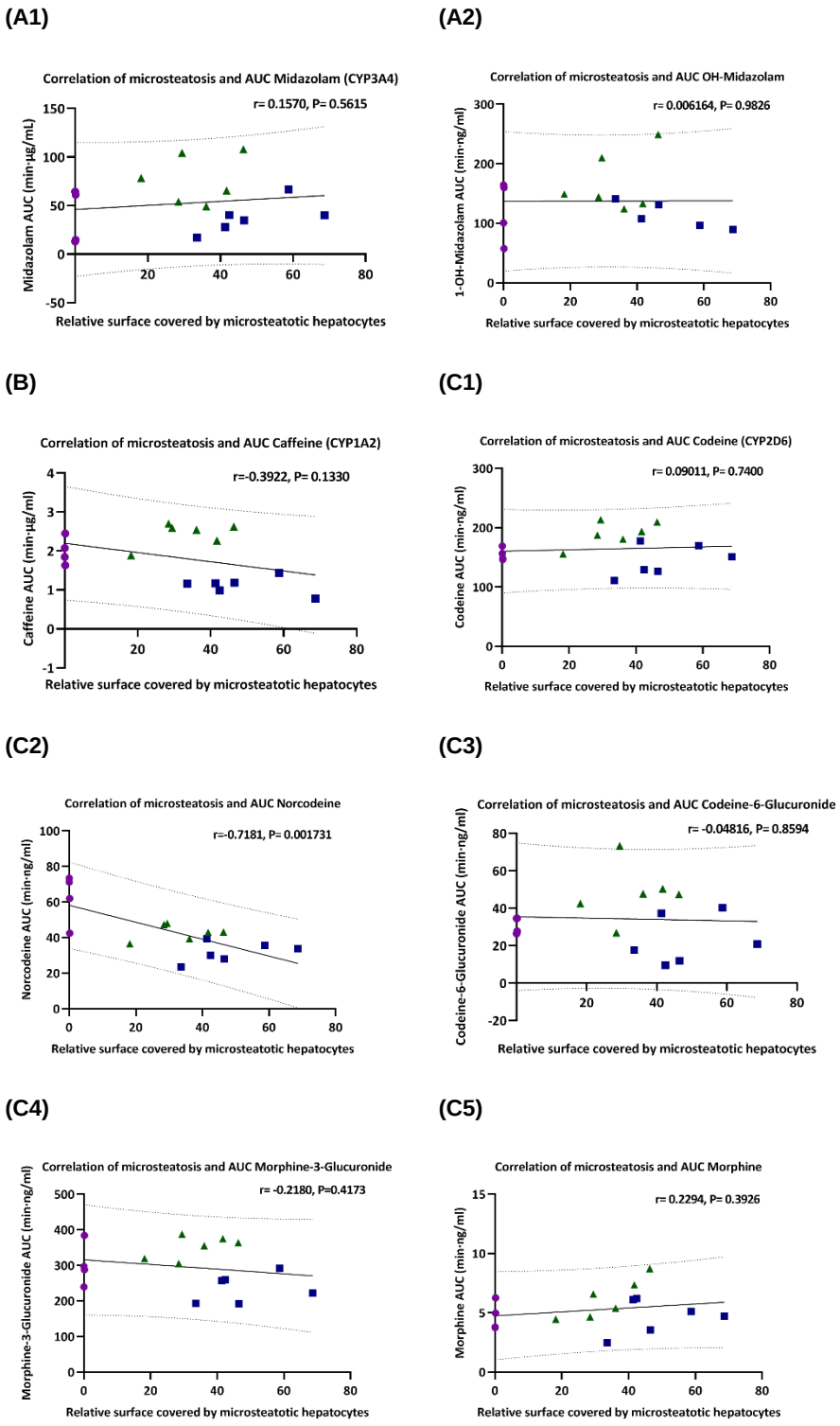

Figure S 5. (A1-C5) Linear correlation between microvesicular steatosis and AUC of the test drugs and their metabolites; (C2) Strong negative correlation between microvesicular steatosis and AUC of norcodeine. Correlation coefficient and p-value indicated in the figure. The heavier the weight of the box line, the stronger is the correlation. Control as magenta circles, two weeks HF-diet as blue squares, four weeks HF-diet as green triangles. “Reproduced with permission from Springer Nature” (Albadry et al. 2022).

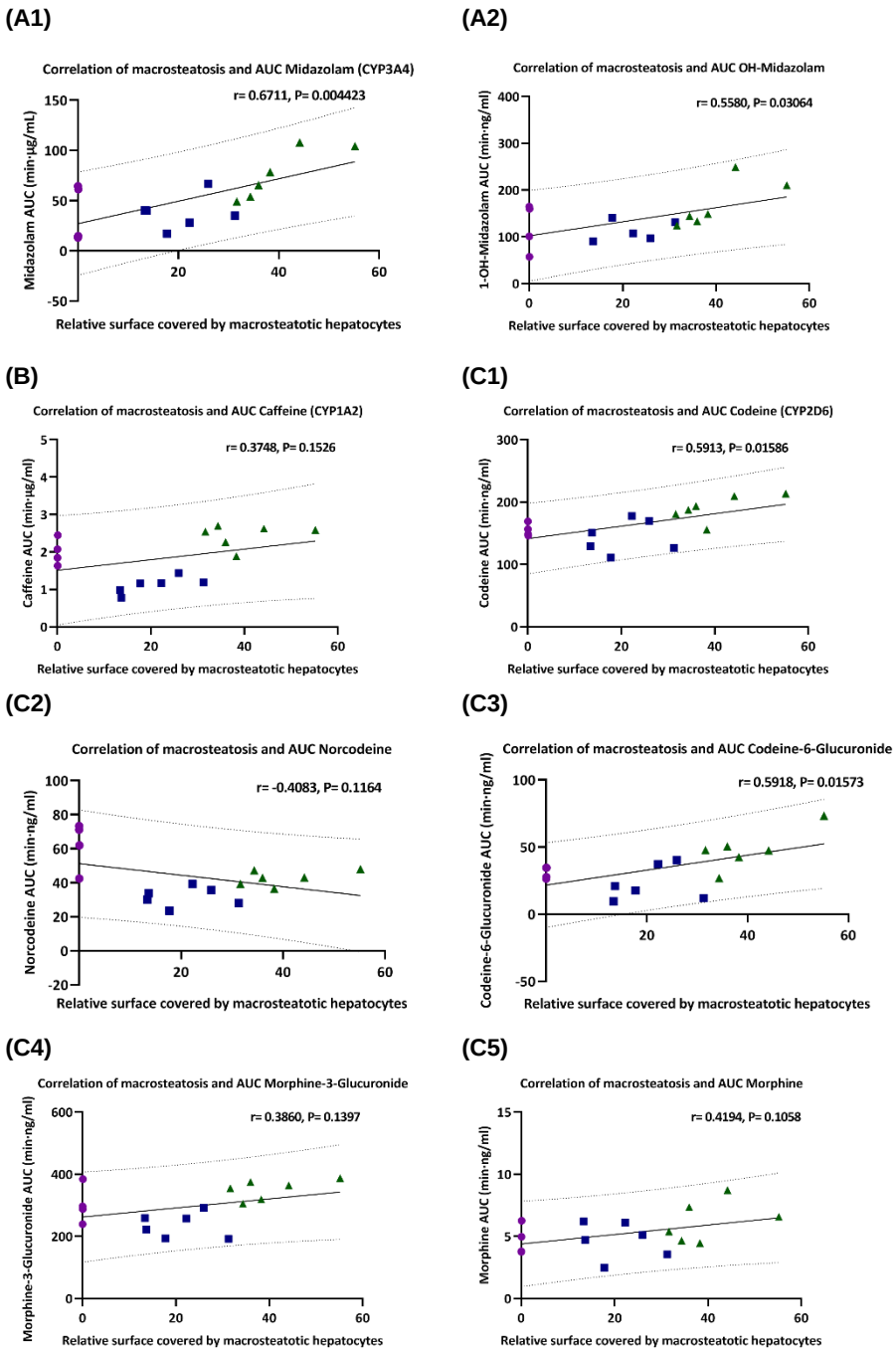

Figure S 6. (A1-C5) Linear correlation between macrovesicular steatosis and AUC of the test drugs and their metabolites. Moderate positive correlation between macrovesicular steatosis and AUC of midazolam (CYP3A4) and OH-midazolam, respectively codeine (CYP2D6) and codeine-6-glucuronide. The correlation coefficient and p-value are indicated in the figure. The correlation coefficient and p-value are indicated in the figure. Control as magenta circles, two weeks HF-diet as blue squares, four weeks HF-diet as green triangles. “Reproduced with permission from Springer Nature” (Albadry et al. 2022).

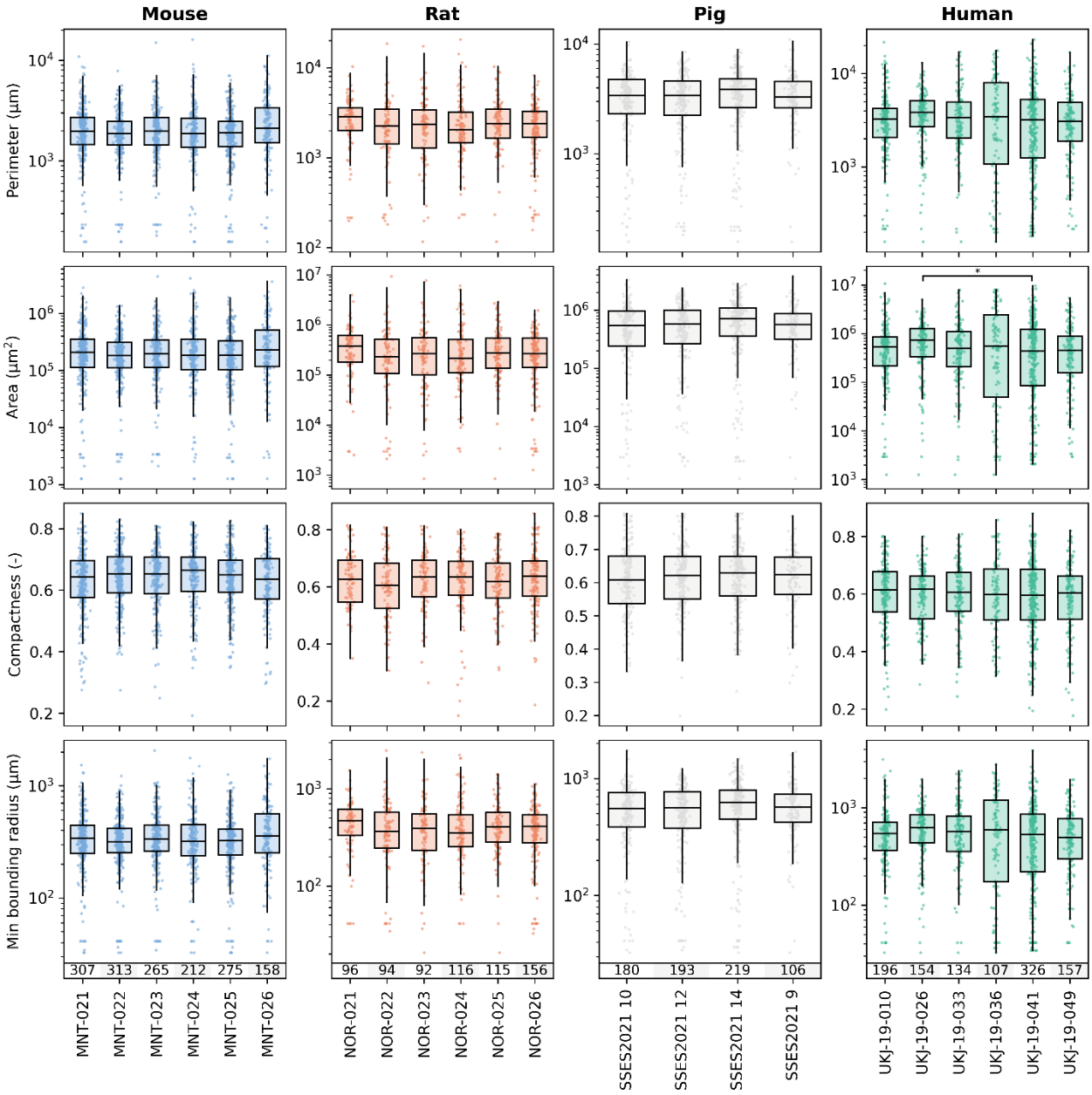

Figure S 7. Intra- and inter-individual variability of lobular geometric parameters in human, pig, rat and mouse. Boxes represent quantiles Q1 and Q3. Upper and lower whiskers extend to the last date less than Q3 + 1.5 * IQR and the first date greater than Q1 - 1.5 * IQR, respectively. IQR denotes interquartile range (Q3-Q1). Significance levels: * p<0.05, ** p<0.01, *** p<0.001, **** p<0.0001. “Reproduced from Frontiers in Pharmacology” (Albadry et al. 2024).

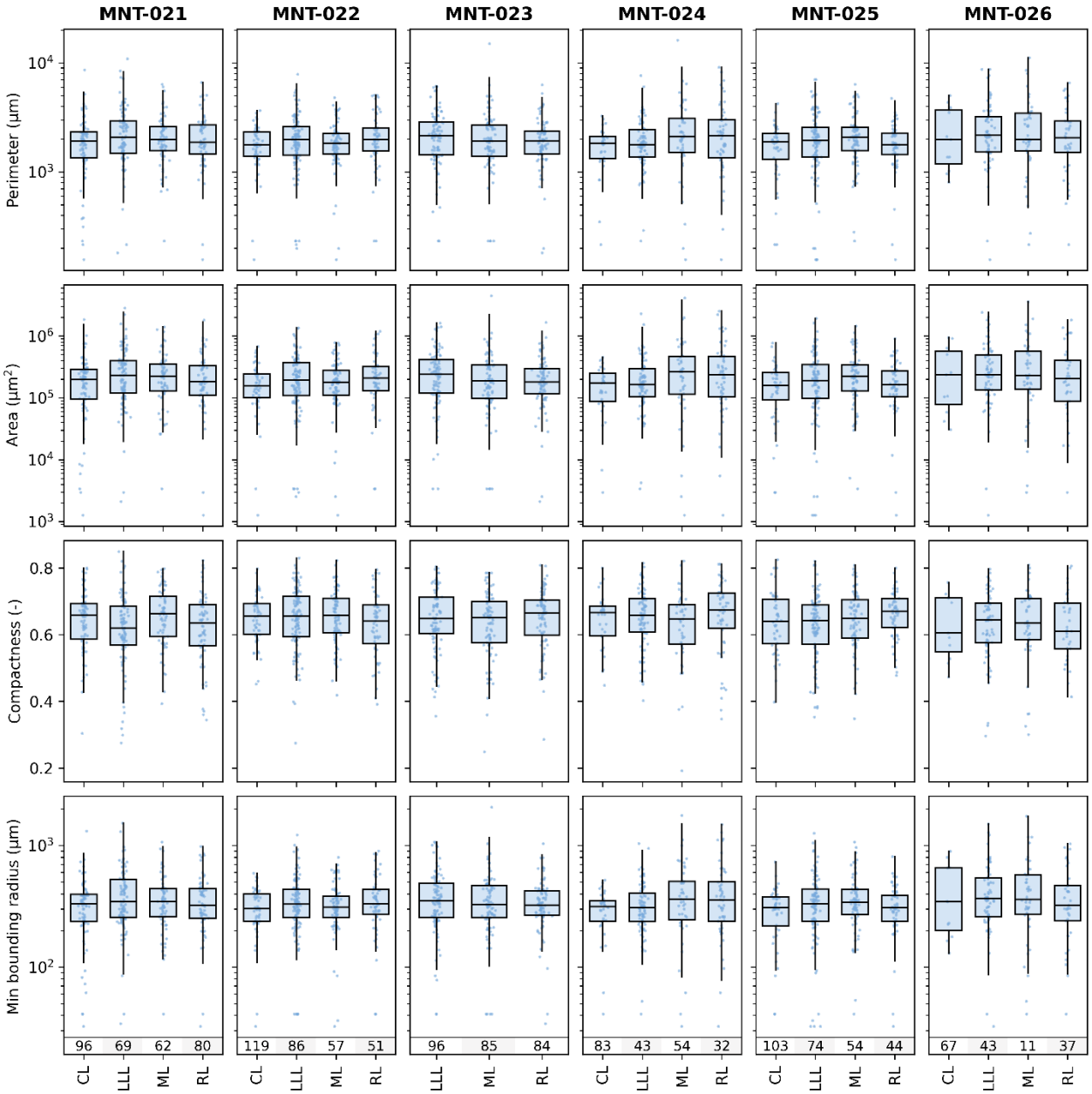

Figure S 8. Intra-lobe variability in lobular geometric parameters in mice. Boxes represent quantiles Q1 and Q3. Upper and lower whiskers extend to the last date less than Q3 + 1.5 * IQR and the first date greater than Q1 - 1.5 * IQR, respectively. IQR denotes interquartile range (Q3-Q1). Significance levels: * p<0.05, ** p<0.01, *** p<0.001, **** p<0.0001. CL: caudate lobe, LLL: left lateral lobe, ML: median lobe, right lobe; lCL in MNT-023 could not be evaluated due to lack of ROI registration. “Reproduced from Frontiers in Pharmacology” (Albadry et al. 2024).

9.3. Permissions amd license agreement

License agreement to use Figure 3. Global, regional data collected from 1990 to 2019 (Younossi et al. 2023).

WOLTERS KLUWER HEALTH, INC. LICENSE
TERMS AND CONDITIONS

Jan 16, 2024

This Agreement between Mr. Mohamed Albadry ("You") and Wolters Kluwer Health, Inc. ("Wolters Kluwer Health, Inc.") consists of your license details and the terms and conditions provided by Wolters Kluwer Health, Inc. and Copyright Clearance Center.

License Number	5710940825018
License date	Jan 16, 2024
Licensed Content Publisher	Wolters Kluwer Health, Inc.
Licensed Content Publication	Hepatology
Licensed Content Title	The global epidemiology of nonalcoholic fatty liver disease (NAFLD) and nonalcoholic steatohepatitis (NASH): a systematic review
Licensed Content Author	Zobair M. Younossi, Pegah Golabi, James M. Paik, et al
Licensed Content Date	Jan 3, 2023
Licensed Content Volume	77
Licensed Content Issue	4
Type of Use	Dissertation/Thesis
Requestor type	University/College

Springer nature agreement to use figures included in the first publication in own thesis (Albadry et al. 2022).

From: Frontiers in Physiology - Production
To: Albadry, Mohamed
Subject: [ext] Copyright (permissions request)
Date: Mittwoch, 3. Januar 2024 11:32:54

Dear Mohamed Albadry,

All Frontiers content is published under a CC-BY Creative Commons attribution license that enables anyone to use the publication freely, given appropriate attribution to the author(s) and citing Frontiers as the original publisher. Therefore, when reusing a figure, the original publication should be cited. For example:

Figure 1, Chen L, Li J, Zhu W, Kuang Y, Liu T, Zhang W, Chen X and Peng C (2020) Skin and Gut Microbiome in Psoriasis: Gaining Insight Into the Pathophysiology of It and Finding Novel Therapeutic Strategies. Front. Microbiol. 11:589726. doi: 10.3389/fmicb.2020.589726

Best regards,
Tobi

Production Team

Production Manager: Marcin Tomaszkow

Frontiers | Production Office

Frontiers

35 New Broad St

London

EC2M 1NH

Office T +41 21 510 17 06

www.frontiersin.org

Frontiers agreement to use figures included in the second publication in own thesis (Albadry et al. 2024)**.**

From: Frontiers in Physiology - Production
To: Albadry, Mohamed
Subject: [ext] Copyright (permissions request)
Date: Mittwoch, 3. Januar 2024 11:32:54

ACHTUNG: Diese E-Mail stammt von einem Absender **außerhalb des UKJ.** Bitte vermeiden Sie es, Anhänge oder externe Links zu öffnen, wenn Sie die **E-Mailadresse des Absenders** Frontiers in Physiology - Production <physiology.production.office@frontiersin.org> nicht kennen. Weitere Informationen finden Sie auf der Intranetseite Informationssicherheit.

Dear Mohamed Albadry,

All Frontiers content is published under a CC-BY Creative Commons attribution license that enables anyone to use the publication freely, given appropriate attribution to the author(s) and citing Frontiers as the original publisher. Therefore, when reusing a figure, the original publication should be cited. For example:

Figure 1, Chen L, Li J, Zhu W, Kuang Y, Liu T, Zhang W, Chen X and Peng C (2020) Skin and Gut Microbiome in Psoriasis: Gaining Insight Into the Pathophysiology of It and Finding Novel Therapeutic Strategies. Front. Microbiol. 11:589726. doi: 10.3389/fmicb.2020.589726

Best regards,
Tobi

Production Team

Production Manager: Marcin Tomaszkow

Frontiers | Production Office

Frontiers

35 New Broad St

London

EC2M 1NH

Office T +41 21 510 17 06

www.frontiersin.org

10. List of own publications regarding this topic

10.1. Research papers

Albadry, M., S. Höpfl, N. Ehteshamzad, M. König, M. Böttcher, J. Neumann, A. Lupp, O. Dirsch, N. Radde, B. Christ, M. Christ, L. O. Schwen, H. Laue, R. Klopfleisch and U. Dahmen (2022): Periportal steatosis in mice affects distinct parameters of pericentral drug metabolism. Scientific Reports 12: 21825. DOI: 10.1038/s41598-022-26483-6.

Albadry, M., J. Kuttner, J. Grzegorzewski, O. Dirsch, E. Kindler, R. Klopfleisch, V. Liska, V. Moulisova, S. Nickel, R. Palek, J. Rosendorf, S. Saalfeld, U. Settmacher, H. M. Tautenhahn, M. Konig and U. Dahmen (2024):
Cross-species variability in lobular geometry and cytochrome P450 hepatic zonation: insights into CYP1A2, CYP2D6, CYP2E1 and CYP3A4.
Front Pharmacol 15: 1404938. DOI: 10.3389/fphar.2024.1404938.

Hopfl, S., **M. Albadry**, U. Dahmen, K. H. Herrmann, E. M. Kindler, M. Konig, J. R. Reichenbach, H. M. Tautenhahn, W. Wei, W. T. Zhao and N. E. Radde (2024):
Bayesian modelling of time series data (BayModTS)-a FAIR workflow to process sparse and highly variable data.
Bioinformatics 40. DOI: 10.1093/bioinformatics/btae312.

Lambers, L., N. Waschinsky, J. Schleicher, M. König, H. M. Tautenhahn, **M. Albadry**, U. Dahmen and T. Ricken (2024):
Quantifying fat zonation in liver lobules: an integrated multiscale in silico model combining disturbed microperfusion and fat metabolism via a continuum biomechanical bi-scale, tri-phasic approach.
Biomech Model Mechanobiol 23: 631-653. DOI: 10.1007/s10237-023-01797-0.

Budelmann, D., C. Qing, H. O. Laue, **M. Albadry**, U. Dahmen and L. O. Schwen (2023):
Segmentation of lipid droplets in histological images.
In Medical Imaging with Deep Learning, short paper track.
https://openreview.net/forum?id=nTnAm_El0RC.

10.2. Conferences

Albadry, M., S. Höpfl, N. Ehteshamzad, M. König, M. Böttcher, J. Neumann, A. Lupp, O. Dirsch, N. Radde, B. Christ, M. Christ, L. O. Schwen, H. Laue, R. Klopfleisch and U. Dahmen (2023): Periportal steatosis in mice affects distinct parameters of pericentral drug metabolism. In Graduate Program Experimental Medicine Jena School for Ageing Medicine Retreat “Oral presentation”.

Albadry, M., S. Höpfl, N. Ehteshamzad, M. König, M. Böttcher, J. Neumann, A. Lupp, O. Dirsch, N. Radde, B. Christ, M. Christ, L. O. Schwen, H. Laue, R. Klopfleisch and U. Dahmen (2023): Periportale Steatose bei Mäusen beeinflusst verschiedene Parameter des perizentralen Arzneimittelstoffwechsels. Tierärztliche Praxis Ausgabe K: Kleintiere/Heimtiere, 51(03), V01.https://doi:10.1055/s-0043-1770858. In 66. Jahrestag. der Fachgr. Pathologie der Deutschen Veterinärmed. Gesellschaft, Fulda, Germany “Oral presentation”.

Albadry, M., A. Lupp, O. Dirsch, H-M. Tautenhahn, R. Klopfleisch, V. Liška and U. Dahmen (2021): Impact of impaired perfusion on drug metabolism in different species. In 24. Chirurgischen Forschungstagen 2021 Virtual “Oral presentation”.

11. Acknowledgment

First of all, I would like to express my gratitude to my principal supervisor, **Prof. Dr. Robert Klopfleisch**, Institute of Veterinary Pathology, Department of Veterinary Medicine, FU-Berlin, for allowing me to be a part of the Biomedical Sciences Ph.D. program organized by Dahlem Research School. I am deeply grateful for his support and guidance, regular advisory meetings, and timely feedback, which greatly aided my progress. His assistance and support have been instrumental in helping me fulfill the DRS Ph.D. program criteria within a reasonable period. He encouraged me to present our research at the National German Meeting of Veterinary Pathology and promoted the dissemination of our results. Prof. Klopfleisch also helped me explore career options inside and outside academia.

I want to express my deepest gratitude to my supervisor**, Prof. Dr. Uta Dahmen,** Head of Experimental Transplantation Surgery at the Department of General, Visceral, and Vascular Surgery at Friedrich-Schiller-University Jena Hospital, for inviting me to join her research group. Her guidance and constructive criticism throughout the research project and the writing process, as well as her critical revision of the thesis, were invaluable. She helped me develop my research and critical thinking skills and encouraged me to attend academic conferences that expanded my scientific horizons. She supported my integration into different interdisciplinary research groups, thereby enhancing my insight into neighboring fields such as system medicine, computational modeling, and image analysis. Her support helped me win the “Michael Stifel Prize” offered by the QuaLiPerF DFG project “FOR 5151.” She also assisted me in future career planning in academia and supported the integration of my family and kids in Germany. I want to express my sincere gratitude for her continuous support.

Furthermore, I would like to express a special acknowledgment to **Prof. Dr. Utz Settmacher,** Director of the Department of General, Visceral, and Vascular Surgery, Friedrich-Schiller-University Jena Hospital, for giving me the precious opportunity to work on liver research in his department. Together with **PD Dr. med. Hans-Michael Tautenhahn**, he granted access to clinical samples.

I am deeply grateful to my mentor, **PD Dr. Lars Mundhenk**, from FU-Berlin's Institute of Veterinary Pathology. He gave me the opportunity to participate in the Veterinary Pathology Journal Club, which helped me build up my scientific background. Overall, his guidance inspired me to think actively about my future career path and take the necessary steps for a successful transition after completing my Ph.D.

I am grateful to **PD Dr. med. Olaf Dirsch,** Director of the Institute of Pathology at the BG Klinikum Unfallkrankenhaus Berlin, for his invaluable support and guidance in my research and training journey. His expertise and insights in pathology greatly improved the quality of my studies, and his assistance in troubleshooting staining protocol issues ensured reliable results. I am truly thankful for his dedication.

I would like to express my sincerest appreciation to **Prof. Dr. Amelie Lupp** from the Institute of Pharmacology and Toxicology at Jena University Hospital in Germany for her invaluable support in establishing and conducting the CYP activity assay. Her exceptional feedback and expertise in Pharmacology were instrumental in ensuring the success of the study (A).

I want to express my gratitude to **Professor Dr. Bruno Christ** from the University of Leipzig Medical Center, Germany, for his expertise in the triglyceride assay and critical feedback in revising the manuscripts, which played a vital role in ensuring the success of the publication process.

I express my sincere appreciation to **Dr. Michael Böttcher,** Head of MVZ Medical Lab Dessau Kassel GmbH, located at Bauhüttenstraße 6, 06847 Dessau-Roßlau, Germany, his exceptional support and expertise in measuring the drug level.

Also, I would like to express my sincere gratitude to **PD. Dr. Matthias König** and his group, from the Institute for Theoretical Biology and Institute of Biology at Humboldt-University in Berlin, Germany, for establishing the image analysis pipeline to quantify CYP zonation and lobular geometry.

I express my profound gratitude to **Mr. Sebastian Höpfl** and his supervisor **Prof Dr. rer. nat Nicole Radde,** an esteemed member of the Institute for Systems Theory and Automatic Control, Faculty of Engineering Design, Production Engineering, and Automotive Engineering at the University of Stuttgart, Germany, for performing Bayesian uncertainty quantification for pharmacokinetics data. His assistance was of tremendous value, as it enabled us to understand the results and overcome the inherent variability of biological data in a scientific manner.

I am very grateful for the support and assistance that I received from the entire team of Experimental Transplantation Surgery at the Department of General, Visceral, and Vascular Surgery, University Hospital Jena. Their expertise and dedication played a significant role in the success of this project. I would also like to thank my colleagues, **Dr. Stefan Pentzold, Dr. med. Fengming Xu, Dr. rer. nat. Janine Arlt, Mr. Mohamad Hashem, Ms. Ana Paz, Mr. XinPei Chen, and Mr. Haotian Chen**, for their collaboration and valuable insights throughout the research process.

ACKNOWLEDGMENT

I hereby acknowledge the utilization of **Grammarly and Quillbot** as language editing tools to ensure grammatical accuracy and consistency in the text.

I would like to take this opportunity to express my deepest appreciation to my family members - **my father, mother, wife (Mrs. Samar Abdelkader), and my kids (Mostafa and Abdelrahman)**. Their constant support and trust throughout my promotion and Ph.D. process have been invaluable in making my academic pursuits a reality. I extend my heartfelt gratitude for their incredible efforts and contributions, which played an integral role in my success. Their dedication and willingness to go above and beyond, even in the face of adversity, is a testament to their support and love.

12. Funding

This research was funded by the German Research Foundation (DFG), “SteaPKMod, Grant number 410848700”, FOR 5151 "QuaLiPerF (Quantifying Liver Perfusion-Function Relationship in Complex Resection - A Systems Medicine Approach), Grant number 436883643”, and “(Priority Programme SPP 2311, Subproject SimLivA), Grant number 465194077.”

Mathias Konig (Humboldt-Universität zu Berlin, Institute for Theoretical Biology, Institute für Biologie, Systems Medicine of the Liver, Berlin, Germany) developed and supported the establishment of the image analysis pipeline for quantification of lobular geometry and CYP gradient intensity. Hans Michael Tautenhahn (Leipzig University Hospital, Clinic and Polyclinic for Visceral, Transplantation, Thoracic, and Vascular Surgery, Leipzig) supported the clinical study. Both M. König and H-M. Tautenhahn were supported by the Federal Ministry of Education and Research (BMBF, Germany) within the research network Systems Medicine of the Liver (LiSyM, Grant number 031L0054). M. König was also supported by the BMBF-funded de.NBI Cloud within the German Network for Bioinformatics Infrastructure (de.NBI) (031A537B, 031A533A, 031A538A, 031A533B, 031A535A, 031A537C, 031A534A, 031A532B).

We acknowledge the support by the Deutsche Forschungsgemeinschaft (German Research Foundation) project number 512648189 and the Open Access Publication Fund of the Thuringian University and State Library Jena.

13. Conflict of interest

In the context of this work, there are no conflicts of interest due to contributions from third parties.

14. Declaration of originality

I hereby certify that I have prepared this thesis independently. I assure that I have used only the sources and aids indicated.

Berlin, 07.08.2024 Mohamed Albadry